UNIVERSITY OF CALIFORNIA SAN DIEGO

Design and Applications of Immune Responsive Biomaterials Scaffolds

A Dissertation submitted in partial satisfaction of the requirements
for the degree Doctor of Philosophy

in

Chemical Engineering

by

Matthew D. Kerr

Committee in charge:

Professor Nisarg J. Shah, Chair
Professor Liangfang Zhang, Co-Chair
Professor Jesse V. Jokerst
Professor Dong-Er Zhang

2023

The Dissertation of Matthew D. Kerr is approved, and it is acceptable in quality and form for publication on microfilm and electronically.

University of California San Diego

2023

DEDICATION

I dedicate my dissertation to my family and my friends. First and foremost, I would like to thank my parents, Brad and Caroline, for their incredible support throughout my entire life. From an early age, they emphasized the importance of freethinking and instilled a passion for learning and strong work ethic. My brother and sister, Lucas and Jennifer, have always been at my side and I am eternally grateful that we are not just siblings but incredible friends. My grandmother, Ying, for helping my parents raise us and being a constant source of inspiration. She is truly one of the strongest women I have ever met, and I am eternally grateful for her perseverance and tenacity. My fianceé, Jess, words cannot express how happy I am that we found each other. Thank you for always being there for me. I love you and cannot wait to see what our future holds.

Lastly, to all my friends both new and old, thank you for supporting me. I am incredibly lucky to have such a fun and caring friend group. Special thanks to Jake Besok, Sam Rosis, Jesus Barragan, Wade Johnson, Luke Nathan and Benny Carriel, you guys are like a second family to me. May our shenanigans never end.

EPIGRAPH

“It is not the critic who counts; not the man who points out how the strong man stumbles, or where the doer of deeds could have done them better. The credit belongs to the man who is actually in the arena, whose face is marred by dust and sweat and blood; who strives valiantly; who errs, who comes short again and again, because there is no effort without error and shortcoming; but who does actually strive to do the deeds; who knows great enthusiasms, the great devotions; who spends himself in a worthy cause; who at the best knows in the end the triumph of high achievement, and who at the worst, if he fails, at least fails while daring greatly, so that his place shall never be with those cold and timid souls who neither know victory nor defeat.”

-Theodore Roosevelt

TABLE OF CONTENTS

LIST OF FIGURES

LIST OF TABLES

ACKNOWLEDGEMENTS

My foremost appreciation is for my mentor and advisor Prof. Nisarg Shah who has been an exceptional mentor and provided me the opportunity to work on cutting-edge projects which greatly accelerated my development as a researcher. I am especially appreciative of the countless hours of discussion, reflection, revision, encouragement, and patience throughout my graduate career. Thank you for everything.

I would like to thank the rest of my thesis committee, Prof. Jesse Jokerst, Prof. Liangfang Zhang, and Prof. Dong-Er Zhang for providing their expertise and time. Especially Prof. Dong-Er Zhang for co-mentoring and providing support for my F31 fellowship application.

I would like to thank Prof. Susan Sharfstein who welcomed me into her lab as an undergraduate under the mentorship of Prof. Cula Svidzinski and later Dr. Karen Torrejon. My experience in the Sharfstein Lab was responsible for my decision to pursue graduate school. I would also like to thank Prof. David Mooney whose lab I worked in as a research technician between undergraduate and graduate school, which provided excellent training and conceptual framework which influenced my own graduate research.

Lastly, I would like to thank my graduate student colleagues, David McBride and Wade Johnson, and my undergraduate mentee Arun Chumber who have been exceptional to work with throughout graduate school. I am fortunate to have met such great lifelong friends and will look back fondly at the time we spent working together.

Chapter 2, in full, is a reprint of the material as it appears in Bioengineering & Translational Medicine. 2022, 8(1): e10309, with the following authors Matthew D. Kerr, David A. McBride, Wade T. Johnson, Arun K. Chumber, Alexander J. Najibi, Bo Ri Seo, Alexander G. Stafford, David T. Scadden, David J. Mooney, & Nisarg J. Shah. The dissertation author was the primary investigator and author of this paper.

Chapter 3, in full, is a reprint of the material as it appears in Expert Opinion on Drug Discovery. 2020, with the following authors Matthew D. Kerr, David A. McBride, Arun K. Chumber, Nisarg J. Shah. The dissertation author was the primary author of this review paper.

Chapter 4, in full, is a copy of a manuscript accepted for publication in Bioengineering & Translational medicine with the following authors Matthew D. Kerr, Wade T. Johnson, David A. McBride, Arun K. Chumber, Nisarg J. Shah. The dissertation author was the primary investigator and author of this paper.

VITA

Education and Field of Study

2023 Doctor of Philosophy in Chemical Engineering, University of California San Diego

2020 Master of Science in Chemical Engineering, University of California San Diego

2017 Bachelor of Science in Nanoscale Engineering & Applied Mathematics, State University of New York Polytechnic Institute

Awards

2022 National Heart, Lung, and Blood Institute F31 Fellowship

2019 Cancer Researchers in Nanotechnology Program T32 Fellowship

Publications

Original Research

Wade T. Johnson, David A. McBride, **Matthew D. Kerr**, Anders Nguyen, Martina Zoccheddu, Miriam Bolman, Xiaofu Wei, Ryan Jones, Wei Wang, Mattias N.D. Svensson, Nunzio Bottini, Nisarg J. Shah. Immunomodulatory nanoparticles for modulating arthritis flares. ACS Nano. [Submitted].

Matthew D. Kerr, Wade T. Johnson, David A. McBride, Arun K. Chumber, Nisarg J. Shah. Biodegradable scaffolds for enhancing vaccine efficacy. Bioengineering & Translational Medicine. [Accepted].

David A. McBride, **Matthew D. Kerr**, Wade T. Johnson, Anders Nguyen, Martina Zoccheddu, Mina Yao, Edward B. Prideaux, Nicholas C. Dorn, Wei Wang, Mattias N.D. Svensson, Nunzio Bottini, Nisarg J. Shah. Immunomodulatory Microparticles Epigenetically Modulate T cells and Systemically Ameliorate Autoimmune Arthritis. Advanced Science. 2202720 (2023).

Colman Moore, Yong Cheng, Natalia Tjokro, Brendan Zhang, **Matthew Kerr**, Mohammed Hayati, Kai Chiao Joe Chang, Nisarg Shah, Casey Chen, Jesse V. Jokerst. A Photoacoustic-Fluorescent Imaging Probe for Proteolytic Gingipains Expressed by Porphyromonas gingivalis. *Angewandte Chemie International Edition.* e202201843 (2022).

Matthew D. Kerr, David A. McBride, Wade T. Johnson, Arun K. Chumber, Alexander J. Najibi, Bo Ri Seo, Alexander G. Stafford, David T. Scadden, David J. Mooney, &

Nisarg J. Shah. Immune-responsive biodegradable scaffolds for enhancing neutrophil regeneration. *Bioengineering & Translational Medicine*, 8(1): e10309 (2022).

David A. McBride, **Matthew D. Kerr**, Shinya L. Wai, Yvonne Y. Yee, Dora A. Ogbonna, & Nisarg J. Shah. Characterization of regulatory T cell expansion for manufacturing cellular immunotherapies. *Biomaterials Science*, 8: 4186-4198 (2020).

Nisarg J. Shah, Angelo S. Mao, Ting-Yu Shih, **Matthew D. Kerr**, Azeem Sharda, Theresa M. Raimondo, James C. Weaver, Vladimir D. Vrbanac, Maud Deruaz, Andrew M. Tager, David J. Mooney, & David T. Scadden. Enhanced T-cell immunity in vivo using injectable bioengineered scaffolds. *Nature Biotechnology*, 37: 293-302 (2019).

Cula N. Dautriche, Dennis Szymanski, **Matthew Kerr**, Karen Y. Torrejon, Magnus Bergkvist, John Danias, W.D. Stamer, & Susan T. Sharfstein. A biomimetic Schlemm's canal inner wall: A model to study outflow physiology, glaucoma pathology and high-throughput drug screening. *Biomaterials,* 65: 86-92 (2015).

Review Articles

David A. McBride, **Matthew D. Kerr**, Nicholas C. Dorn, Dora A. Ogbonna, Evan C. Santos, Nisarg J. Shah. Triggers, Timescales, and Treatment for Cytokine-Mediated Tissue Damage. *EMJ Innov,* DOI: 10.33590/emjinnov/20-00203 (2020).

Matthew D. Kerr, David A. McBride, Arun K. Chumber, & Nisasrg J. Shah. Combining therapeutic vaccines with chemo- and immunotherapies in the treatment of cancer. *Expert Opinion on Drug Discovery*, DOI: 10.1080/17460441.2020.1811673 (2020).

David A. McBride*, **Matthew D. Kerr***, Shinya L. Wai, Nisarg J. Shah. Applications of molecular engineering in T-cell-based immunotherapies. *WIREs Nanomed Nanobiotechnol*, e1557 (2019). *Denotes Equal Contribution

Book Chapters

Karen Y. Torrejon & **Matthew D. Kerr**. Bioengineered human trabecular meshwork membrane constructs: opportunities and challenges. *Glaucoma Research and Clinical Advances 2018 - 2020*, 85-98 (2017).

ABSTRACT OF THE DISSERTATION

Design and Applications of Immune Responsive Biomaterials Scaffolds

by

Matthew D. Kerr

Doctor of Philosophy in Chemical Engineering

University of California San Diego, 2023

Professor Nisarg J. Shah

Sustained release of immune modulating agents is a potential strategy to enhance the efficacy of immunotherapies compared to traditional bolus delivery strategies. However, methods for sustaining release often rely on implants composed of materials that remain in the body over an extended period, often permanently, and remain susceptible to a pathogenic foreign body response (FBR). This body of work focuses on the design and validation of immune responsive degradable biomaterials to sustain release of immune modulating agents to facilitate drug delivery while mitigating the risk of an adverse FBR. This thesis focuses on harnessing the innate immune cell response to biomaterials through systematic studies assessing degradation and release of encapsulated agents. To this end, the development of a cell-permissive macroporous hyaluronic acid (HA)-based scaffold, termed HA cryogel, is reported. HA cryogels were formed by rapidly freezing an aqueous solution containing crosslinkable polymers. The resulting scaffold comprised interconnected pores which permitted stress dissipation during a minimally invasive deployment via an injection. Immunophenotypic characterization of innate immune cells infiltrating HA cryogels post-injection revealed that degradation is primarily mediated by neutrophils, which are early participants in the foreign body response. In mice modeling transient or chronic immune deficiency HA cryogel degradation was significantly delayed or altogether absent. The cell-responsive behavior of HA cryogels was leveraged to enhance immune reconstitution in post-hematopoietic stem cell transplanted mice through sustained release of granulocyte colony stimulating factor. The utility of HA cryogels was further validated in sustaining the release of vaccine components to enhance immunity in mouse models of immune deficiency and cancer. In a melanoma

mouse model, the HA cryogel-based vaccine enhanced the antigen-specific adaptive immunity compared to bolus vaccination and induced robust prophylactic and therapeutic protection. In sum, this body of work provides a path for the development and validation of biodegradable materials as a therapeutic delivery modality that mediates sustained release of immune modulating agents.

CHAPTER 1

1.0 Introduction

This body of work focuses on the design and validation of degradable biomaterials to sustain release of immunomodulators to enhance immunity. A key aspect of this work focuses on harnessing the innate immune cell response to biomaterials to shape the immune response through systematic studies assessing biomaterial degradation and release of encapsulated agents. Sustained drug release was utilized to demonstrate the enhancement of innate and adaptive immunity in models of immune deficiency and cancer.

1.1 Background

1.1.1 Innate and adaptive immunity

The immune system is comprised of an extensive network of specialized cells and tissue systems which provide protection against foreign pathogens and cancers. The cells which constitute the immune system can broadly be categorized as either innate or adaptive immune cells [1–3]. Innate immune cells are responsible for a variety of immune surveillance functions mediated in part by pattern recognition receptors (PRRs) that sense, identify, and respond to pattern associated molecular patterns. Downstream signaling of PRRs can lead to a variety of cellular responses including phagocytosis, cytokine secretion, membrane attack complex activation[1,3]. A variety of innate immune cells can act as antigen presenting cells which express a subset PRRs known as toll-like receptors, whose activation mediates activation of adaptive immune cells[4–7].

The adaptive immune system consists primarily of T and B cells which are specialized to respond to antigen-specific challenges. Adaptive immunity has the important feature of

memory which persists even after the stimulating antigen is cleared, thereby providing long lasting protection. Both T and B cells are activated in secondary lymph nodes by professional antigen presenting cells[8,9]. Activated cytotoxic T cells expand rapidly and eliminate their target through various mechanisms which includes direct lysis[10]. In contrast, activated helper T cells interface with professional antigen presenting cells and secrete cytokines which can broadly activate or suppress surrounding immune cells[11,12]. Following pathogen clearance, a small number of activated cytotoxic and helper T cells persist as memory T cells, which more rapidly respond to repeat infections from the same pathogen[10-12]. B cells in secondary lymph nodes can activated upon exposure to foreign antigen and/or activation by helper T cells[8]. Activated B cells may differentiate into long-lived plasma cells, which form long-term immunological memory and generate antibodies which can bind to foreign pathogens and target them for clearance by phagocytic innate immune cells[13].

1.1.2 Drug-eluting implants

Drug-eluting implants are designed to release an active agent, typically in a sustained manner to treat and/or prevent disease. This subset of such implants consists of a biocompatible polymer encapsulating a small molecule or protein therapeutic. Examples include sustained release of etonogestrel from subcutaneous implants to prevent pregnancy[14], sustained release of paclitaxel from stents to prevent narrowing of the coronary artery[15], and sustained release of bone morphogenic protein from a collagen matrix for spinal fusion[16]. Other pre-clinical examples include antibiotic releasing orthopedic implants to prevent infection after joint replacement[17], sustained release of

immunomodulatory agents to treat autoimmunity in a local manner[18], and sustained release of vaccine components to enhance vaccination efficacy[19,20].

1.1.3 Foreign body response and impact on device function

The foreign body response (FBR) is a term used to describe the general reaction of primarily innate immune cells to implants. FBR is thought to be a sequential process and begins immediately after implantation[21]. Neutrophils mediate the primary response and localize on the biomaterial surface within hours[22]. Monocyte and fibroblast presence on the biomaterial follows neutrophil recruitment and occurs within the first day of implantation[21,23]. Monocytes differentiate into pro-inflammatory macrophages which contribute to inflammation by secretion of cytokines[24]. Fibroblasts secrete extracellular matrix to partition the device from the surrounding tissue[21]. Long-term presence of the implant results in fibrotic encapsulation and fusion of macrophages into foreign body giant cells to partition the device from the surrounding tissue[21].

While FBR is associated with all implants, the duration of cellular recruitment and amount of inflammation are influenced by a multitude of factors including device location, surface chemistries, device porosity, and endotoxin content[25–27]. These are important considerations as pathogenic FBR can impair device function or lead to device failure[28–31]. For example, device failure due to FBR is associated with joint replacement implants where the development of a fibrotic capsule can lead to complications and failure[32,33].

1.1.4 Hydrogels for drug delivery

Hydrogels are cross-linked polymer networks composed primarily of water which are commonly used in pre-clinical drug delivery and tissue engineering applications[34,35]. Polymer composition, density, molecular weight, and cross-linking chemistries can all be

modified to achieve desired physiochemical properties and degradation profile[34]. The mesh size for hydrogels can vary substantially and is influenced by the degree of crosslinking density, with higher crosslinking density resulting in smaller mesh size[36,37]. Hydrogels can be designed to deliver proteins that have a size that is comparable to the hydrogel mesh, allowing for degradation mediated release[37,38].

A potential limitation for deploying hydrogels with a nanometer-scale mesh size in vivo is the risk of structural failure during a minimally invasive injection[39]. Various strategies have been developed to overcome this limitation including cryogelation which is a crosslinking method in which the crosslinking process is conducted below freezing temperature of water, allowing formation of ice crystals and large interconnected pores that allow for stress disappation[39–41]. Hydrogels formed in this manner are termed “cryogels” and have an interconnected porous structure which allows for deformation under shearing stress[41,42]. During injection, cryogels can compress through the needle and expand to regain their initial shape[35,41–43]. Furthermore, the high surface area to volume ratio of cryogels compared to hydrogels results in differences in both degradation and release kinetics.

1.2 Objective

The overall objective of the thesis is to design an injectable degradable biomaterial scaffold to mediate sustained release of immunomodulatory agents.

1.3 Overview

This thesis is divided into five major sections. Chapter 2 explores the development and characterization of a hyaluronic acid (HA) cryogel system to sustain the release of granulocyte colony stimulating factor (G-CSF) post-hematopoietic stem cell transplant

(HSCT) to accelerate neutrophil reconstitution. Chater 3 provides background on clinical results of cancer vaccines and pre-clinical strategies to improve efficacy of cancer vaccines. Chapter 4 detail the development of a HA cryogel-based sustained release vaccine formulation to enhance the immune response for protection against cancer. Chapter 5 provides and discusses future directions for utilizing the HA cryogel platform as a drug delivery device.

1.4 Specific Aims

Aim 1: Development of injectable HA cryogel platform and characterization of degradation mechanisms (Chapter 2). Aim 1 overviews click-functionalization of HA, HA cryogel fabrication, and materials characterization of the HA cryogel. Materials characterization includes quantification of surface porosity, assessment of interconnectedness, and degradation kinetics in vitro. In vivo characterization involves quantification of degradation kinetics and comprehensive assessment of the FBR to the HA cryogel in both immune competent and various models of immune deficiency. To assess the FBR, phenotypic analysis of infiltrating innate immune cells and histological analysis of excised cryogels were conducted.

Aim 2: Sustaining release of G-CSF from HA cryogel to enhance neutrophil reconstitution post-HSCT (Chapter 2). Aim 2 assesses delayed HA cryogel degradation and innate immune cell infiltration in immune deficient post-HSCT context. G-CSF is encapsulated within HA cryogel and release kinetics of G-CSF is compared in both immune competent and post-HSCT settings. G-CSF encapsulated HA cryogel is utilized to enhance neutrophil reconstitution kinetics post-HSCT and equivalence to clinical standard PEG G-CSF is determined.

Aim 3: Development of HA cryogel vaccine formulation to enhance adaptive immunity (Chapter 4). Aim 3 utilizes the HA cryogel to mediate sustained release of vaccine components to enhance vaccine efficacy. First, HA cryogels are fabricated from multiple suppliers. Comparisons based on materials characterization, in vitro degradation, and in vitro release kinetics of encapsulated OVA are conducted. Next, OVA encapsulated HA cryogels are administered to mice and differences in in vivo degradation, FBR, and B cell response to OVA are assessed. The effect of encapsulation of additional adjuvants, cystine paired guanine (CpG) and/or granulocyte macrophage colony stimulating factor (GM-CSF), on in vivo degradation kinetics, FBR, and adaptive immune response to OVA were all characterized. As a result of these, we conducted further assessments with a formulation termed CpG-OVA-HAC2. Dose escalation studies showed vaccine dose dependence of the adaptive immune response. Studies with B16-OVA melanoma model showed the CpG-OVA-HAC2 mediated protection against cancer development with greatly improved efficacy compared to dose matched bolus equivalent.

1.5 References

1. Kaczanowska S, Joseph AM, Davila E. TLR agonists: our best frenemy in cancer immunotherapy. J Leukoc Biol. 2013;93(6):847-863. doi:https://doi.org/10.1189/jlb.1012501

2. Marshall JS, Warrington R, Watson W, Kim HL. An introduction to immunology and immunopathology. Allergy, Asthma & Clinical Immunology. 2018;14(2):49. doi:10.1186/s13223-018-0278-1

3. Kawasaki T, Kawai T. Toll-Like Receptor Signaling Pathways. Front Immunol. 2014;5. https://www.frontiersin.org/articles/10.3389/fimmu.2014.00461

4. Vono M, Lin A, Norrby-Teglund A, Koup RA, Liang F, Loré K. Neutrophils acquire the capacity for antigen presentation to memory CD4+ T cells in vitro and ex vivo. Blood. 2017;129(14):1991-2001. doi:10.1182/blood-2016-10-744441

5. Grabowska J, Lopez-Venegas MA, Affandi AJ, den Haan JMM. CD169+ Macrophages Capture and Dendritic Cells Instruct: The Interplay of the Gatekeeper and the General of the Immune System. Front Immunol. 2018;9. https://www.frontiersin.org/articles/10.3389/fimmu.2018.02472

6. Muntjewerff EM, Meesters LD, van den Bogaart G. Antigen Cross-Presentation by Macrophages. Front Immunol. 2020;11. https://www.frontiersin.org/articles/10.3389/fimmu.2020.01276

7. Lin A, Loré K. Granulocytes: New Members of the Antigen-Presenting Cell Family. Front Immunol. 2017;8. https://www.frontiersin.org/articles/10.3389/fimmu.2017.01781

8. Doherty DG, Melo AM, Moreno-Olivera A, Solomos AC. Activation and Regulation of B Cell Responses by Invariant Natural Killer T Cells. Front Immunol. 2018;9. https://www.frontiersin.org/articles/10.3389/fimmu.2018.01360

9. Bousso P. T-cell activation by dendritic cells in the lymph node: lessons from the movies. Nat Rev Immunol. 2008;8(9):675-684. doi:10.1038/nri2379

10. Zhang Z, Liu S, Zhang B, Qiao L, Zhang Y, Zhang Y. T Cell Dysfunction and Exhaustion in Cancer. Front Cell Dev Biol. 2020;8. https://www.frontiersin.org/articles/10.3389/fcell.2020.00017

11. Zhu J, Yamane H, Paul WE. Differentiation of Effector CD4 T Cell Populations. Annu Rev Immunol. 2010;28(1):445-489. doi:10.1146/annurev-immunol-030409-101212

12. Rocamora-Reverte L, Melzer FL, Würzner R, Weinberger B. The Complex Role of Regulatory T Cells in Immunity and Aging. Front Immunol. 2021;11. https://www.frontiersin.org/articles/10.3389/fimmu.2020.616949

13. Malkiel S, Barlev AN, Atisha-Fregoso Y, Suurmond J, Diamond B. Plasma Cell Differentiation Pathways in Systemic Lupus Erythematosus. Front Immunol. 2018;9. https://www.frontiersin.org/articles/10.3389/fimmu.2018.00427

14. Agrawal A, Robinson C. An assessment of the first 3 years' use of Implanon® in Luton. Journal of Family Planning and Reproductive Health Care. 2005;31(4):310. doi:10.1783/147118905774480581

15. Stone GW, Ellis SG, Cox DA, et al. A Polymer-Based, Paclitaxel-Eluting Stent in Patients with Coronary Artery Disease. New England Journal of Medicine. 2004;350(3):221-231. doi:10.1056/NEJMoa032441

16. Hustedt JW, Blizzard DJ. The Controversy Surrounding Bone Morphogenetic Proteins in the Spine: A Review of Current Research. Yale J Biol Med. 2014;87(4):549-561.

17. Xi W, Hegde V, Zoller SD, et al. Point-of-care antimicrobial coating protects orthopaedic implants from bacterial challenge. Nat Commun. 2021;12(1):5473. doi:10.1038/s41467-021-25383-z

18. McBride DA, Kerr MD, Johnson WT, et al. Immunomodulatory Microparticles Epigenetically Modulate T Cells and Systemically Ameliorate Autoimmune Arthritis. Advanced Science. 2023;10(11):2202720. doi:https://doi.org/10.1002/advs.202202720

19. Bencherif SA, Warren Sands R, Ali OA, et al. Injectable cryogel-based whole-cell cancer vaccines. Nat Commun. 2015;6(1):7556. doi:10.1038/ncomms8556

20. Gale EC, Powell AE, Roth GA, et al. Hydrogel-Based Slow Release of a Receptor-Binding Domain Subunit Vaccine Elicits Neutralizing Antibody Responses Against SARS-CoV-2. Advanced Materials. 2021;33(51):2104362. doi:https://doi.org/10.1002/adma.202104362

21. Anderson JM, Rodriguez A, Chang DT. Foreign body reaction to biomaterials. Semin Immunol. 2008;20(2):86-100. doi:https://doi.org/10.1016/j.smim.2007.11.004

22. Jhunjhunwala S, Aresta-DaSilva S, Tang K, et al. Neutrophil Responses to Sterile Implant Materials. PLoS One. 2015;10(9):e0137550-. https://doi.org/10.1371/journal.pone.0137550

23. Chandorkar Y, K R, Basu B. The Foreign Body Response Demystified. ACS Biomater Sci Eng. 2019;5(1):19-44. doi:10.1021/acsbiomaterials.8b00252

24. Liu Y, Segura T. Biomaterials-Mediated Regulation of Macrophage Cell Fate. Front Bioeng Biotechnol. 2020;8. https://www.frontiersin.org/articles/10.3389/fbioe.2020.609297

25. Yin Y, He XT, Wang J, et al. Pore size-mediated macrophage M1-to-M2 transition influences new vessel formation within the compartment of a scaffold. Appl Mater Today. 2020;18:100466. doi:https://doi.org/10.1016/j.apmt.2019.100466

26. Shih TY, Blacklow SO, Li AW, et al. Injectable, Tough Alginate Cryogels as Cancer Vaccines. Adv Healthc Mater. 2018;7(10):1701469. doi:https://doi.org/10.1002/adhm.201701469

27. van Putten SM, Wübben M, Plantinga JA, Hennink WE, van Luyn MJA, Harmsen MC. Endotoxin contamination delays the foreign body reaction. J Biomed Mater Res A. 2011;98A(4):527-534. doi:https://doi.org/10.1002/jbm.a.33144

28. Spearman BS, Desai VH, Mobini S, et al. Tissue-Engineered Peripheral Nerve Interfaces. Adv Funct Mater. 2018;28(12):1701713. doi:https://doi.org/10.1002/adfm.201701713

29. Salatino JW, Ludwig KA, Kozai TDY, Purcell EK. Glial responses to implanted electrodes in the brain. Nat Biomed Eng. 2017;1(11):862-877. doi:10.1038/s41551-017-0154-1

30. Capuani S, Malgir G, Chua CYX, Grattoni A. Advanced strategies to thwart foreign body response to implantable devices. Bioeng Transl Med. 2022;7(3):e10300. doi:https://doi.org/10.1002/btm2.10300

31. Chen FM, Liu X. Advancing biomaterials of human origin for tissue engineering. Prog Polym Sci. 2016;53:86-168. doi:https://doi.org/10.1016/j.progpolymsci.2015.02.004

32. Jacobs JJ, Urban RM, Wall J, Black J, Reid JD, Veneman L. Unusual foreign-body reaction to a failed total knee replacement: simulation of a sarcoma clinically and a sarcoid histologically. A case report. JBJS. 1995;77(3). https://journals.lww.com/jbjsjournal/Fulltext/1995/03000/Unusual_foreign_body_reaction_to_a_failed_total.15.aspx

33. Gibon E, Córdova LA, Lu L, et al. The biological response to orthopedic implants for joint replacement. II: Polyethylene, ceramics, PMMA, and the foreign body reaction. J Biomed Mater Res B Appl Biomater. 2017;105(6):1685-1691. doi:https://doi.org/10.1002/jbm.b.33676

34. Drury JL, Mooney DJ. Hydrogels for tissue engineering: scaffold design variables and applications. Biomaterials. 2003;24(24):4337-4351. doi:https://doi.org/10.1016/S0142-9612(03)00340-5

35. Shah NJ, Mao AS, Shih TY, et al. An injectable bone marrow–like scaffold enhances T cell immunity after hematopoietic stem cell transplantation. Nat Biotechnol. 2019;37(3). doi:10.1038/s41587-019-0017-2

36. Urueña JM, Pitenis AA, Nixon RM, Schulze KD, Angelini TE, Gregory Sawyer W. Mesh Size Control of Polymer Fluctuation Lubrication in Gemini Hydrogels. Biotribology. 2015;1-2:24-29. doi:https://doi.org/10.1016/j.biotri.2015.03.001

37. Amsden BG. Hydrogel Mesh Size and Its Impact on Predictions of Mathematical Models of the Solute Diffusion Coefficient. Macromolecules. 2022;55(18):8399-8408. doi:10.1021/acs.macromol.2c01443

38. Appel EA, Loh XJ, Jones ST, Dreiss CA, Scherman OA. Sustained release of proteins from high water content supramolecular polymer hydrogels. Biomaterials. 2012;33(18):4646-4652. doi:https://doi.org/10.1016/j.biomaterials.2012.02.030

39. Chen MH, Wang LL, Chung JJ, Kim YH, Atluri P, Burdick JA. Methods To Assess Shear-Thinning Hydrogels for Application As Injectable Biomaterials. ACS Biomater Sci Eng. 2017;3(12):3146-3160. doi:10.1021/acsbiomaterials.7b00734

40. Hixon KR, Lu T, Sell SA. A comprehensive review of cryogels and their roles in tissue engineering applications. Acta Biomater. 2017;62:29-41. doi:https://doi.org/10.1016/j.actbio.2017.08.033

41. Koshy ST, Ferrante TC, Lewin SA, Mooney DJ. Injectable, porous, and cell-responsive gelatin cryogels. Biomaterials. 2014;35(8):2477-2487. doi:https://doi.org/10.1016/j.biomaterials.2013.11.044

42. Eggermont LJ, Rogers ZJ, Colombani T, Memic A, Bencherif SA. Injectable Cryogels for Biomedical Applications. Trends Biotechnol. 2020;38(4):418-431. doi:10.1016/j.tibtech.2019.09.008

43. Shah NJ, Najibi AJ, Shih TY, et al. A biomaterial-based vaccine eliciting durable tumour-specific responses against acute myeloid leukaemia. Nat Biomed Eng. 2020;4(1):40-51. doi:10.1038/s41551-019-0503-3

CHAPTER 2

IMMUNE-RESPONSIVE BIODEGRADABLE SCAFFOLDS FOR ENHANCING NEUTROPHIL REGENERATION

2.0 Abstract

Neutrophils are essential effector cells for mediating rapid host defense and their insufficiency arising from therapy-induced side-effects, termed neutropenia, can lead to immunodeficiency-associated complications. In autologous hematopoietic stem cell transplantation (HSCT), neutropenia is a complication that limits therapeutic efficacy. Here, we report the development and in vivo evaluation of an injectable, biodegradable hyaluronic acid (HA)-based scaffold, termed HA cryogel, with myeloid responsive degradation behavior. In mouse models of immune deficiency, we show that the infiltration of functional myeloid-lineage cells, specifically neutrophils, is essential to mediate HA cryogel degradation. Post-HSCT neutropenia in recipient mice delayed degradation of HA cryogels by up to 3 weeks. We harnessed the neutrophil-responsive degradation to sustain the release of granulocyte colony stimulating factor (G-CSF) from HA cryogels. Sustained release of G-CSF from HA cryogels enhanced post-HSCT neutrophil recovery, comparable to pegylated G-CSF, which, in turn, accelerated cryogel degradation. HA cryogels are a potential approach for enhancing neutrophils and concurrently assessing immune recovery in neutropenic hosts.

2.1 Introduction

Neutrophils mediate essential host defense against pathogens and are among the earliest responders in tissue injury [1-3]. Neutrophil deficiency, termed neutropenia, contributes to

opportunistic infections and could impair tissue regeneration in affected individuals [4-7]. In autologous hematopoietic stem cell transplantation (HSCT) pre-conditioning myelosuppressive regimens can contribute to a marked transient post-therapy impairment of neutrophils and render recipients susceptible to immune deficiency-associated complications for up to several weeks [6, 8-11].

Post-HSCT neutrophil regeneration follows successful bone marrow engraftment of transplanted hematopoietic cells [12, 13], facilitated by granulocyte colony stimulating factor (G-CSF)-mediated granulopoiesis of hematopoietic cells [14-16]. Neutropenia is typically treated as an emergency and, in a subset of patients, the risk of neutropenia may be prophylactically addressed with post-HSCT subcutaneous injection of recombinant human G-CSF (filgrastim) to facilitate recovery [6, 14, 17, 18]. Daily injections are used as G-CSF has a half-life of a 3 – 4 hours, which can be extended by conjugating G-CSF with polyethylene glycol (PEGylation) [19, 20]. However, immune responses against PEG have been demonstrated to enhance clearance of PEG-G-CSF in an antibody-dependent manner [21]. As multiple cycles of PEG-G-CSF treatment are common, long-term treatment could be rendered ineffective. Therefore, the development of a sustained release method to deliver G-CSF while avoiding immune responses against PEG, and concurrently assess neutrophil function could greatly improve the current standard-of-care.

Seeking to improve post-HSCT recovery of neutrophils and simultaneously assess recovery, we developed a biodegradable depot to prophylactically deliver G-CSF in post-HSCT recipients. The depot comprised a porous injectable scaffold made by low-temperature crosslinking, termed cryogelation, of hyaluronic acid (HA), an easily sourced and readily derivatized anionic glycosaminoglycan, termed ‘HA cryogel.’ As a component

of the extracellular matrix, endogenous HA is a substrate for degradation by myeloid cells through enzymatic action and by neutrophil-mediated oxidation [22-24]. Harnessing the immune-responsiveness of HA, we characterized in vivo degradation of HA cryogels in immune deficient and post-HSCT mice and identified myeloid cell infiltration in HA cryogels to be key mediators in facilitating degradation, which was significantly reduced or altogether eliminated in mice with severely deficient neutrophil function. Transient but profound post-HSCT myeloid depletion significantly delayed degradation of HA cryogels until recovery of neutrophils [25]. As the degradation profile of HA cryogels was responsive to neutrophil recovery, we harnessed encapsulated G-CSF to facilitate the sustained release, which was mediated by HA cryogel degradation. Neutrophil reconstitution was enhanced in post-HSCT mice injected with G-CSF-encapsulated HA cryogels, comparable to a single dose of PEGylated G-CSF, which accelerated HA cryogel degradation.

2.2 Results

2.2.1 Synthesis and characterization of HA cryogels

Click-functionalized HA was prepared by conjugating either tetrazine (Tz) amine or norbornene (Nb) methylamine to HA using carbodiimide chemistry. Nb- functionalized HA (HA-Nb) was reacted with Tz-Cy5 to form Cy5-labeled HA-Nb (Cy5-HA-Nb) (**Fig. 2.1a**). Tz amine-functionalized HA (HA-Tz) was prepared at 7% degree of substitution (termed high-DOS). 0.8% DOS HA-Tz (termed low DOS) was also prepared for comparison. Endotoxin levels of HA-Tz and Cy5-HA-Nb were quantified to be less than 5 endotoxin units/kg, the threshold pyrogenic dose for preclinical species (**Supplementary Table 2.1**) [26]. To maximize polymer concentration while maintaining proper viscosity to achieve

mixing, 0.6% w/v aqueous solutions of HA-Tz and Cy5-HA-Nb, pre-cooled to 4^{o}C, were well mixed in a 1:1 (v/v) ratio by vortexing (**Fig. 2.1a**). The solution was then pipetted onto individual pre-cooled (-20^{o}C) cryomolds (30 μL/mold) and immediately transferred to a -20^{o}C freezer and allowed to freeze (**Supplementary Note 2.1**), to generate Cy5-HA cryogels (**Fig. 2.1b, c**).

To characterize Cy5-HA cryogels, we estimated the swelling ratio by comparing the hydrated vs. cast volume and the aqueous mass composition from the wicked mass and fully hydrated mass. The swelling ratio was 1.5 ± 0.1 in both low- and high-DOS Cy5-HA cryogels (**Supplementary Fig. 2.1a**). The aqueous mass composition was 76.3 ± 4.0% and 71.9 ± 2.6% in low- and high-DOS Cy5-HA cryogels respectively (**Supplementary Fig. 2.1b**).

To measure surface porosity of lyophilized Cy5-HA cryogels, we used scanning electron microscopy (SEM) (**Fig. 2.1d, Supplementary Fig. 2.1c**). The surface pore structure images were used to measure the average pore diameter using FIJI, which were between 80-180μm and 40-90μm for low- and high-DOS Cy5-HA cryogels respectively (**Supplementary Fig. 2.1d**). To characterize interconnectedness of the Cy5-HA cryogel pore structure, we incubated fully hydrated low- and high-DOS Cy5-HA cryogels with Fluorescein isothiocyanate (FITC)-labeled 10μm diameter melamine resin particles and imaged using a confocal microscope (**Fig. 2.1e, Supplementary Fig. 2.1e**). Since the route of administration of the Cy5-HA cryogels is through a needle, we repeated this experiment with Cy5-HA cryogels after injection and observed similar penetration of the FITC-labeled 10μm particles (**Fig. 2.1e, Supplementary Fig. 2.1e**). Image analysis of z-stacked images showed co-localization of the FITC-labeled 10μm particles with Cy5-HA

up to a depth of 100μm below the surface, which was the limit of detection (**Supplementary Fig. 2.1f**). Both low- and high-DOS Cy5-HA cryogels maintained pore morphology and relative surface pore size distribution following lyophilization and rehydration (**Supplementary Fig. 2.2.1g, 1h**). Cy5-HA cryogels also maintained shape and structure post-injection (**Supplementary Movie 2.1**).

To confirm susceptibility of Cy5-HA cryogels to enzymatic degradation, we used a hyaluronidase-2 (HYAL2)-based in vitro assay (**Fig. 2.1f**). In native HA, HYAL2 cleaves internal beta-N-acetyl-D-glucosaminidic linkages resulting in fragmentation of HA [27]. Here, HYAL2 degraded HA cryogels and high DOS Cy5-HA cryogels degraded at a slower rate compared to the low-DOS Cy5-HA cryogels in vitro (**Fig. 2.1g, Supplementary Fig. 2.2a**). To assess in vivo degradation, low- and high-DOS Cy5-HA cryogels were injected subcutaneously in the hind flank of C57Bl/6J (B6) mice and degradation was measured using in vivo imaging system (IVIS) fluorescence spectroscopy (**Fig. 2.1h**). In contrast to in vitro degradation, both low- and high-DOS Cy5-HA cryogels degraded at a similar rate (**Fig. 2.1i, Supplementary Fig. 2.2b**). This observation, together with the finding of a similar pore size distribution in hydrated low- and high-DOS HA cryogels (**Supplementary Fig. 2.S1h**), supported the selection of one of the types of HA cryogels for subsequent experiments, and we selected high-DOS HA cryogels. To characterize if HA cryogels made from different batches of derivatized HA affected in vivo degradation, we compared degradation of Cy5-HA cryogels made from three distinct batches of Cy5-HA-Nb and HA-Tz and confirmed that all Cy5-HA-cryogels degraded at a similar rate (**Supplementary Fig. 2.2c**).

2.2.2 Depletion of immune cell subsets affects cellular infiltration into HA cryogels

As the HSCT pre-conditioning regimen depletes all immune cell lineages, we first sought to measure the effect of immune depletion on HA cryogel degradation. Cy5-HA cryogels were subcutaneously injected into the hind flank of untreated B6 mice (**Fig. 2.2a**) and the degradation profile was compared to that in B6 mice receiving (i) anti-Ly6G and anti-rat κ immunoglobulin light chain antibodies to deplete neutrophils (~98% efficiency) (**Fig. 2.2b**), (ii) clodronate liposomes to deplete monocytes/macrophages (80-95% efficiency) (**Fig. 2.2c**), (iii) anti-CD4 and anti-CD8 antibodies to deplete T cells (~99% efficiency) (**Supplementary Fig. 2.3a**), (iv) anti-B220 to transiently deplete B-cells (99% efficiency up to 4 days) (**Supplementary Fig. 2.3b**) and immune deficient NOD.Cg-Prkdcscid Il2rgtm1Wjl/SzJ (NSG) mice (**Fig. 2.2d**). The durability of depletion was assessed by measuring peripheral blood cellularity throughout the duration of the degradation study (**Supplementary Fig. 2.3c-l, Supplementary Table 2.2**). In untreated immune competent mice, the average half-life of Cy5-HA cryogels, quantified as the time to achieve a 50% reduction in fluorescence intensity, was about 9.5 days (**Supplementary Fig. 2.3m**). The average half-life in the macrophage, neutrophil, T cell, and B cell depleted mice was similar at about 11.8 days, 11.3 days, 9.6, and 10.2 respectively (**Supplementary Fig. 2.3m**). In contrast, only a 35% reduction in Cy5 signal intensity was measured after 3 months in the NSG mice (**Fig. 2.2d**). Retrieval of Cy5-HA cryogels from sacrificed mice at the endpoint confirmed that the gels had minimally degraded (**Supplementary Fig. 2.3n**).

To assess cellular infiltration and the foreign body response, Cy5-HA cryogels were explanted from the above groups at 1-, 5-, and 10-days post-injection and stained using

haemotoxylin and eosin (H&E). In Cy5-HA cryogels retrieved from all groups except NSG mice, the total cellularity increased from day 1 to 10 and formed a distinct capsule encapsulating the HA cryogel, indicative of a foreign body response (**Fig. 2.2e, Supplementary Fig. 2.4a**). In NSG mice, some infiltrates were quantified on day 1, however there was no appreciable increase in cellularity at the later timepoints or a capsule by day 10 (**Fig. 2.2e**). H&E slides were further analyzed to quantify the cell density in the different groups. Differences in infiltrates between the untreated and all immunodepleted B6 mice were significant at the earlier timepoints, and either increased or remained constant in all immunodepleted B6 (**Fig 2.2f, Supplementary Fig. 2.4b**). In contrast, cell infiltrates in HA cryogels retrieved from NSG mice reduced steadily and were 80% lower than untreated B6 mice by day 10 (**Fig. 2.2f**).

To identify the immune cells contributing to HA cryogel degradation, we quantified cell infiltrates in the Cy5-HA cryogels 1- and 10- days post-injection using flow cytometry in untreated and immune depleted B6 and NSG mice (**Fig. 2.3a, b, Supplementary Fig. 2.5a, b**). Viability of infiltrating cells, quantified by negative AnnexinV staining, was consistently greater than 95% in all groups (**Supplementary Fig. 2.5c**).

Infiltration of total $CD45^{+}CD11b^{+}$ (myeloid) cells into HA cryogels of untreated B6 mice and T cell depleted B6 mice were similar after 1- and 10-days post-injection (**Supplementary Fig. 2.5d**). While there were comparable myeloid cells in HA cryogels retrieved 1-day post-injection from B cell depleted B6 mice, by day 10 the number was about 66% lower than in untreated B6 mice (**Supplementary Fig. 2.5e**). Similarly, myeloid cell infiltration in Cy5-HA cryogels retrieved 1-day post-injection from macrophage depleted mice was unaffected, however by day ten the number of infiltrating

myeloid cells was about 58% lower than untreated B6 mice (**Fig. 2.3c**). Neutrophil depletion in B6 mice reduced the total number of myeloid cells in Cy5-HA cryogels compared with the untreated B6 mice by about 77% 1-day and 68% 10-days post-injection respectively (**Fig. 2.3c**). In NSG mice myeloid cell infiltration in HA cryogels was 51% lower 1-day and 91% lower 10-days post-injection as compared to untreated B6 mice (**Fig. 2.3c**).

$CD45^+CD11b^+F4/80^+$ (macrophage) infiltration in Cy5-HA cryogels retrieved from all groups except NSG mice reduced from 1- to 10-days (**Fig. 2.3d**, **Supplementary Fig. 2.5e**). Intraperitoneal (i.p.) administration of clodronate liposomes minimally affected macrophage infiltration in Cy5-HA cryogels even though it was effective in depleting peripheral blood monocytes (**Fig. 2.3d, Supplementary Fig. 2.3g, h**). In NSG mice, macrophage infiltration was 74% lower than in the untreated B6 mice on day 1 and remained unchanged 10-days post-injection (**Fig. 2.3d**).

In $CD45^+CD11b^+F4/80^-Ly6G^+$ (neutrophil) depleted B6 mice, an additional intracellular Ly6G staining step was included, as the method of neutrophil depletion is known to induce internalization of the Ly6G receptor (**Supplementary Fig. 2.5f**) [28]. Neutrophil infiltration in Cy5-HA cryogels retrieved from untreated B6 and T cell depleted B6 mice was comparable between 1- to 10-days post-injection (**Fig. 3e**, **Supplementary Fig. 2.5g**). B cell depletion did not affect the initial neutrophil infiltration 1-day post-injection compared with untreated controls but reduced the number of infiltrating neutrophils by 10-days post-injection (**Supplementary Fig. 2.5g**). As expected, neutrophil depletion significantly reduced initial neutrophil infiltration, by about 97%, compared to the untreated control. In this group, neutrophils constituted less than 50% of infiltrating myeloid cells at all

timepoints assessed (**Fig. 2.3f**). Despite an increase by day 10, attributable to the internalization of the Ly6G receptor which led to an approximate 4-fold increase in the infiltrating neutrophil fraction (**Supplementary Fig. 2.5f**), the number of infiltrating neutrophils were still 84% lower compared with untreated B6 mice (**Fig. 2.3e**). Macrophage depletion did not affect the initial neutrophil infiltration 1-day post-injection compared with untreated B6 mice but reduced the number of infiltrating neutrophils by 65% compared with untreated B6 mice by day 10. HA cryogels retrieved from NSG mice had 50% fewer neutrophils than those from untreated B6 mice on day 1 and very few to none were found by day 10 post-injection (**Fig. 2.3e**). In NSG mice neutrophils constituted over 90% of total myeloid cells on day 1 but decreased to about 8% by day 10 (**Fig. 2.3f**). This observation along with minimal Cy5-HA cryogel degradation in NSG mice (**Fig. 2.2d**), supported a key role of functional neutrophils in mediating degradation. In all groups, the infiltration of $CD45^{+}CD11b^{+}F4/80^{-}Ly6G^{-}CD115^{+}$ (monocyte) cells were minimal and constituted a negligible portion of total infiltrating myeloid cells (**Supplementary Fig. 2.5h, i**).

To provide additional confirmation of infiltrating neutrophils and macrophages, we used immunohistochemical (IHC) staining to assess for $Ly6G^{+}$ and $F4/80^{+}$ cells respectively in untreated B6 mice and NSG mice at 1-, 5-, and 10-days post-injection. Staining on day 1 corroborated the flow cytometry data in that there were more neutrophils than macrophages within the Cy5-HA cryogels (**Supplementary Fig. 2.5i, Supplementary Fig. 2.6a**). On subsequent days, non-specific debris precluded accurate assessment in Cy5-HA cryogels retrieved from B6 mice (**Supplementary Fig. 2.6a**). As a result of non-specific staining of debris at later timepoints, IHC was only conducted on Cy5-HA cryogels

excised 1-day after injection in macrophage depleted, neutrophil depleted, T cell depleted, and B cell depleted mice. Staining of these samples confirmed the presence of both Ly6G and F4/80 in Cy5-HA cryogels confirming flow cytometry data (**Supplementary Fig. 2.5i, Supplementary Fig. 2.6b**). In NSG mice, IHC staining of $Ly6G^+$ and $F4/80^+$ cells followed the results from flow cytometry analysis. Significantly more neutrophils than macrophages in Cy5-HA cryogels were observed 1-day after injection (**Supplementary Fig. 2.6c**). On day 5, there were significant macrophage and neutrophil infiltrates (**Supplementary Fig. 2.6c**) and by day 10, the neutrophil infiltration reduced significantly as expected from flow cytometry analysis (**Supplementary Fig. 2.5h, Supplementary Fig. 2.6c**).

To further characterize the role of functional neutrophils, we compared the degradation of Cy5-HA cryogels in B6 and B6.129S-$Cybb^{tm1Din}$ ($gp91^{phox-}$) mice. Affected hemizygous male $gp91^{phox-}$ mice have a defect in the NADPH oxidase enzyme, which renders mice deficient in neutrophil function through the production of reactive oxygen species [29, 30]. Cy5-HA cryogels were injected in $gp91^{phox-}$ mice and B6 mice and degradation was quantified using IVIS (**Fig. 2.3g**). Cy5-HA cryogels did not degrade appreciably in the $gp91^{phox-}$ over the course of the two-month study whereas the Cy5-HA cryogels in B6 mice degraded within 4 weeks, as expected (**Fig. 2.3h**).

Taken together, these results suggest that inducing immune deficiency by depletion affects cell infiltration in Cy5-HA cryogels but does not affect degradation. However, deficiencies which functionally impair neutrophils, modeled by NSG and $gp91^{phox-}$ mice are sufficient to significantly affect Cy5-HA cryogel degradation.

2.2.3 HA cryogels are neutrophil responsive in post-HSCT mice

We next quantified Cy5-HA cryogel degradation in post-HSCT mice. B6 recipients were irradiated 48 hours prior to i.v. injection of lineage depleted hematopoietic stem cells (2 x 10^5 cells, ~87% depleted) isolated from bone marrow of syngeneic B6 donor mice (**Supplementary Fig. 2.7a**). Concurrently, B6 recipients and control mice (B6, non-irradiated that do not receive a transplant) were injected subcutaneously with Cy5-HA cryogels, and the degradation rate was compared (**Fig. 2.4a**). In contrast to non-irradiated mice, a steady fluorescence signal was quantified for about 20 days in post-HSCT mice after which it decreased, corresponding to HA cryogel degradation, at a rate comparable to that in non-irradiated mice. The time interval to 50% of the initial fluorescence intensity was approximately 30 days in post-HSCT mice whereas in non-irradiated mice, a comparable decrease was achieved by day 13 (**Fig. 2.4b, Supplementary Fig. 2.7b**).

To quantify infiltrating myeloid subsets, Cy5-HA cryogels were excised on days 5 and 16 post-injection in non-irradiated mice and excised on days 5, 16, 21, and 26 in post-HSCT mice (**Fig. 2.4c**). Viability of infiltrating cells, quantified by negative AnnexinV staining, was initially lower 5- and 16-days post-injection, and increased by day 21 (**Supplementary Fig. 2.7c**). In non-irradiated B6 mice, the number of infiltrating myeloid cells decreased by 96% from days 5 to 16 post-injection (**Fig. 2.4d**), mirroring near-complete Cy5-HA cryogel degradation (**Fig. 2.4b, Supplementary Fig. 2.7b**). In contrast, myeloid cell infiltration in Cy5-HA cryogels was significantly delayed and 97% lower than that of the non-irradiated group, 5 days post-injection. In post-HSCT mice, appreciable myeloid infiltration was not quantified until about day 21 post-HSCT, which was still 67% lower when compared with HA cryogels from non-irradiated mice on day 5 (**Fig. 2.4d**).

Macrophage infiltration in Cy5-HA cryogels in non-irradiated mice decreased 87% from days 5 to 16 (**Fig. 2.4e**). On day 5 in post-HSCT mice, macrophage infiltration in Cy5-HA cryogels was reduced by about 92% compared to non-irradiated mice. By day 26, infiltrating macrophages in some post-HSCT mice were quantified but remained significantly lower than macrophage infiltration on day 5 in non-irradiated mice (**Fig. 2.4e**). Neutrophils constituted a majority of the myeloid cells in Cy5-HA cryogels in non-irradiated mice on day 5, but not by day 16 (**Fig. 2.4f**) when the majority of myeloid cells were macrophages (**Supplementary Fig. 2.7d**). In contrast, very few cells were in HA cryogels retrieved on day 5 in post-HSCT mice with a near absence of neutrophils, in contrast with non-irradiated mice at the same timepoint. Neutrophil infiltration in Cy5-HA cryogels was quantified 21 days post-injection but was still 62% lower than on day 5 in non-irradiated mice (**Fig. 2.4f**). In post-HSCT mice, macrophages constituted most of the cell infiltrates 5- and 16-days after injection, whereas a majority of myeloid cells were neutrophils on days 21 and 26 (**Supplementary Fig. 2.7d**). This data supports that irradiation reduces myeloid infiltration in Cy5-HA cryogels, delays cryogel degradation, and degradation coincides with neutrophil recovery (**Supplementary Fig. 2.7e**).

To assess whether the uniqueness of the results could be attributed to the HA cryogels, we compared the results with hydrolytically degradable oxidized alginate (OxAlg), also functionalized with Tz and Nb (**Supplementary Fig. 2.7f**). Unlike HA, OxAlg is not a substrate for endogenous enzymes [31, 32]. Tz-functionalized OxAlg was functionalized with Cy5 and Cy5-OxAlg cryogels were formed in the same manner as high-DOS Cy5-HA cryogels. In vitro, Cy5-OxAlg cryogels fully degraded in 1x PBS over 9-days (**Supplementary Fig. 2.7g**). In contrast to Cy5-HA cryogels, Cy5-OxAlg cryogels injected

in B6 and post-HSCT B6 mice degraded rapidly at a comparable rate, with approximately 70% reduction in fluorescence signal within 24 hours post-injection (**Supplementary Fig. 2.7h**).

2.2.4 HA cryogels sustain G-CSF delivery and enhance post-HSCT reconstitution of neutrophils

We sought to leverage the delay in post-HSCT degradation of HA cryogels to mediate G-CSF release and enhance neutrophil recovery. 1µg of Cy5-labeled G-CSF (Cy5 G-CSF) was encapsulated in HA cryogels and one cryogel was injected either in 1-day post-HSCT or in non-irradiated B6 mice. Encapsulated Cy5 G-CSF was quantified using IVIS and normalized to the initial 8-hour timepoint fluorescence signal (**Fig. 2.5a**). Cy5 G-CSF release, assessed by fluorescence attenuation, from non-irradiated mice proceeded in a sustained manner immediately post-injection with over 80% released after approximately 12-days post-injection. In post-HSCT mice, 20% Cy5 G-CSF released after approximately 12-days post-injection and subsequently released in a sustained manner (**Fig. 2.5b**). The time to 50% fluorescence intensity in non-irradiated mice was 5.9 ± 3.0 days compared to 15.5 ± 5.9 days in post-HSCT mice (**Fig. 2.5c**). We then sought to assess the effect of G-CSF delivery on peripheral blood neutrophil recovery and acceleration of Cy5-HA cryogel degradation. We compared mice receiving either two blank Cy5-HA cryogels or two G-CSF-encapsulated HA-cryogels and, as a positive control, we included mice with blank Cy5-HA cryogels injected systemically with 2µg pegylated (PEG) G-CSF (**Fig. 2.5d**), corresponding to the clinical-equivalent dose for mice [33, 34]. Mice were bled at pre-determined timepoints, and peripheral blood neutrophil concentration, quantified by flow cytometry, was consistently higher when G-CSF from Cy5-HA cryogels was delivered, and comparable with PEG G-CSF treatment than in mice which received blank Cy5-HA

cryogels (**Fig. 2.5e**). Moreover, Cy5-HA cryogel degradation was accelerated with G-CSF or PEG G-CSF treatment (**Fig. 5f, Supplementary Fig. 2.8**). These results support that G-CSF release from HA cryogels can improve neutrophil recovery in lethally radiated mice and Cy5-HA cryogel degradation may simultaneously be used as an indicator of functional neutrophil recovery.

2.3 Discussion

Here we demonstrate that an immune responsive biodegradable HA cryogel scaffold provides sustained G-CSF release and accelerates post-HSCT neutrophil recovery in mice which, in turn, accelerates HA cryogel degradation in vivo. Harnessing post-HSCT immune deficiency to sustain G-CSF release is distinct conceptually from other methods of drug delivery. It is well established that immune cells sense implanted materials as non-self and mount a well-characterized sequential response to isolate the implant in a fibrous capsule [35-37]. In this work, we observed neutrophil infiltration during the acute stages of inflammation and show them to be key mediators in HA cryogel degradation. Our finding is consistent with prior reports that have supported neutrophils as key mediators of shaping the early implant microenvironment and for in vivo destruction of implanted polymeric materials by neutrophil-derived oxidants [38-40]. The finding of primarily myeloid-lineage immune cell populations within the HA cryogel is consistent with previous observations of cell infiltration occurring within scaffolds of a similar composition [41, 42]. We demonstrate that the encapsulation and release of G-CSF from the polymer scaffold mediated recovery of neutrophils in the peripheral blood, significantly faster than control mice receiving blank HA cryogels and comparable to pegylated GCSF, which accelerated HA cryogel degradation.

HA was selected as the primary constituent polymer as it is ubiquitous in the extracellular matrix and has a long history of clinical use as a biodegradable material in a range of biomedical applications [43-48]. In this work, commercially purchased HA was derivatized with bioorthogonal Tz and Nb groups to facilitate crosslinking without the need for external energy input or addition of external agents such as stabilizers and catalysts [49, 50], which can make it challenging to purify the final product. The use of HA-Tz and HA-Nb also facilitated cryogelation at a slower rate, compared to free-radical polymerization methods, and consequently provided enhanced control over the crosslinking process [51, 52]. Moreover, other common cross-linking strategies that directly target the carboxylic acid or hydroxyl side chains groups and unreacted agents may inadvertently react with encapsulated proteins [53-56]. Further, Tz can be quantified spectroscopically and the DOS was readily assessed [57, 58].

Degradation of HA can be mediated by both enzymatic and non-enzymatic reactions. Enzymatic degradation is mediated by hyaluronidases, a class of enzymes that degrade predominantly HA and are widely distributed in mammalian tissues in the extracellular space, on the cell surface of stromal cells and intracellularly in lysosomal compartments[59]. Endogenous non-enzymatic reactions have been demonstrated to be mediated predominately by reactive oxygen species for which neutrophils are a major source, and which lack hyaluronidase[60, 61]. Consistent with prior work, our results show that DOS affected the rate of HA cryogel degradation by enzymatic cleavage in vitro [22, 62]. On the other hand, the paradoxical observation that DOS did not affect in vivo degradation is also consistent with prior work that has demonstrated that partial degradation of HA by non-enzymatic means in vivo overcomes steric factors which might otherwise hinder

enzymatic access to HA and, in our work, facilitated equalization of the in vivo degradation rate of low- and high- DOS HA cryogels [62].

Our results support that activated neutrophils mediate degradation of HA cryogels in vivo, consistent with past reports of the role of reactive oxygen species from activated neutrophils in mediating HA degradation [60, 63-65] and of neutrophils in the acute phase of the foreign body response [35, 36], which further clarifies how immune deficiency impacts the rate of degradation [9, 66]. We found that while despite successfully depleting neutrophils in the peripheral blood, antibody-based depletion did not achieve a similar depletion of infiltrating neutrophils in HA cryogels and degradation was unaffected in B6 mice. In NSG mice, which have defective adaptive and innate immune cells, Cy5-HA cryogels degraded minimally over 3 months and neutrophil infiltration into the HA cryogel was not sustained. The observation is consistent with the well-documented lack of adaptive immune cells, impaired innate immune cell subsets (e.g. macrophages) and a lack of a functional complement system which affects the activation of neutrophils in these mice [67-70]. We expanded upon these results by quantifying Cy5-HA cryogel degradation in gp91^{phox-} mice, which are on the B6 background, but gp91^{phox-} neutrophils in affected hemizygous male mice lack superoxide production [29, 30]. The functional deficiency of neutrophils in gp91^{phox-} is similar to the clinical observations of defective respiratory burst and phagocytosis affecting neutrophils in chronic granulomatous disease, in which there are normal neutrophil counts but impaired oxidative killing [29]. In these mice, the absence of appreciable degradation of Cy5-HA cryogels provides additional support for the key role of functional neutrophils in facilitating degradation.

The key role of functional neutrophils in HA cryogel degradation was further validated in post-HSCT mice, modeling transient innate immune deficiency. Unlike antibody-based depletion, irradiating mice achieves full depletion of innate and adaptive immune cells. Neutrophils predominate the earliest immune cells that reconstitute[71] and post-HSCT respiratory burst and phagocytic activity of neutrophils is generally decreased in humans, modeled by gp91^{phox-} mice, and underscores the importance of qualitatively assessing functionality of neutrophils [72]. We found that Cy5-HA cryogel degradation was delayed until neutrophil infiltration into Cy5-HA cryogels recovered, further supporting the role of neutrophils in mediating HA degradation and the immune responsive behavior of HA cryogels. These results are consistent with past reports in which rapid neutrophil infiltration and activation have been identified as one of the earliest cellular events of the foreign body response [2, 73]. In contrast, we show that OxAlg cryogels, which have hydrolytically labile groups but are not a substrate for endogenous enzymes, degrade rapidly in vivo at similar rates in immune competent and post-HSCT mice [31, 32, 74]. These observations characterizing the importance of neutrophils in degradation support the unique immune responsiveness of HA cryogels.

Similar to PEG-G-CSF, we demonstrate the effect of G-CSF release from HA cryogels is neutrophil-dependent [75], and therefore might be characterized as self-regulating. However, in contrast to PEG-G-CSF, G-CSF delivery from HA cryogels avoids the potential of pre-existing or induced anti-PEG antibody (APA)-mediated rapid clearance [76, 77]. In immune competent mice, it has been demonstrated that the administration of PEG-G-CSF at a clinically-relevant single dose elicits anti-PEG IgM antibodies in a dose-dependent manner which subsequently accelerates clearance of a second PEG-G-CSF

dose via an anti-PEG IgM-mediated complement activation [21]. De novo anti-PEG antibody induction may not require T cell activation [78] and therefore could also be induced in post-HSCT immunodeficient hosts. PEG G-CSF may therefore be less effective with pre-existing or induced APA [79].

Therapy-induced neutropenia substantially limits the applicability of therapies that could be life-saving. HA cryogels not only deliver G-CSF in a sustained manner to enhance neutrophil regeneration, while avoiding the potential of APA-mediated enhanced clearance, but also show a responsive degradation behavior. Collectively, our findings support that the HA cryogels might be leveraged to enhance and functionally assess neutrophil functionality and aid in treatment-related decisions for recipients of myelosuppressive therapy.

2.4 Figures

Figure 2.1| Production and characterization of Cy5-HA cryogel
(**a**) Schematic for tetrazine (Tz) and norbornene (Nb) functionalization of HA, Cy5 functionalization of Nb functionalized HA (Cy5-HA-Nb) and crosslinking of Tz functionalized HA with Cy5-HA-Nb. (**b**) Schematic for producing Cy5-HA cryogels. (**c**) Representative photograph of lyophilized Cy5-HA cryogel. Scale bar = 1mm. (**d**) Representative SEM image depicting Cy5-HA cryogels. Top scale bar = 1mm, middle scale bar = 500μm, bottom scale bar = 100μm. (**e**) Confocal microscopy image, overhead and side views, depicting hydrated Cy5-HA cryogels pre- and post-injection incubated with 10μm FITC-labeled microparticles. Scale bar = 100μm. (**f**) Schematic depicting workflow for in vitro Cy5-HA cryogel degradation study. (**g**) Measuring Cy5-HA cryogel degradation in vitro by quantifying the Cy5-signal in supernatant at pre-determined timepoints normalized to total Cy5-signal in supernatant across all timepoints. (**h**) Schematic depicting workflow for in vivo Cy5-HA cryogel degradation study. (**i**) Representative in vivo imaging system (IVIS) fluorescence images of gel degradation in mice and measuring Cy5-HA cryogel degradation in vivo by quantification of total radiant efficiency normalized to initial day 3 timepoint. IVIS Images are on the same scale and analyzed using Living Image Software. Data in **g** represents mean ± s.d. of n=4 HA cryogels. Data in **i** represents mean ± s.e.m. of n=4 HA cryogels. Part of figure **1b, f and h** were created with BioRender.com.

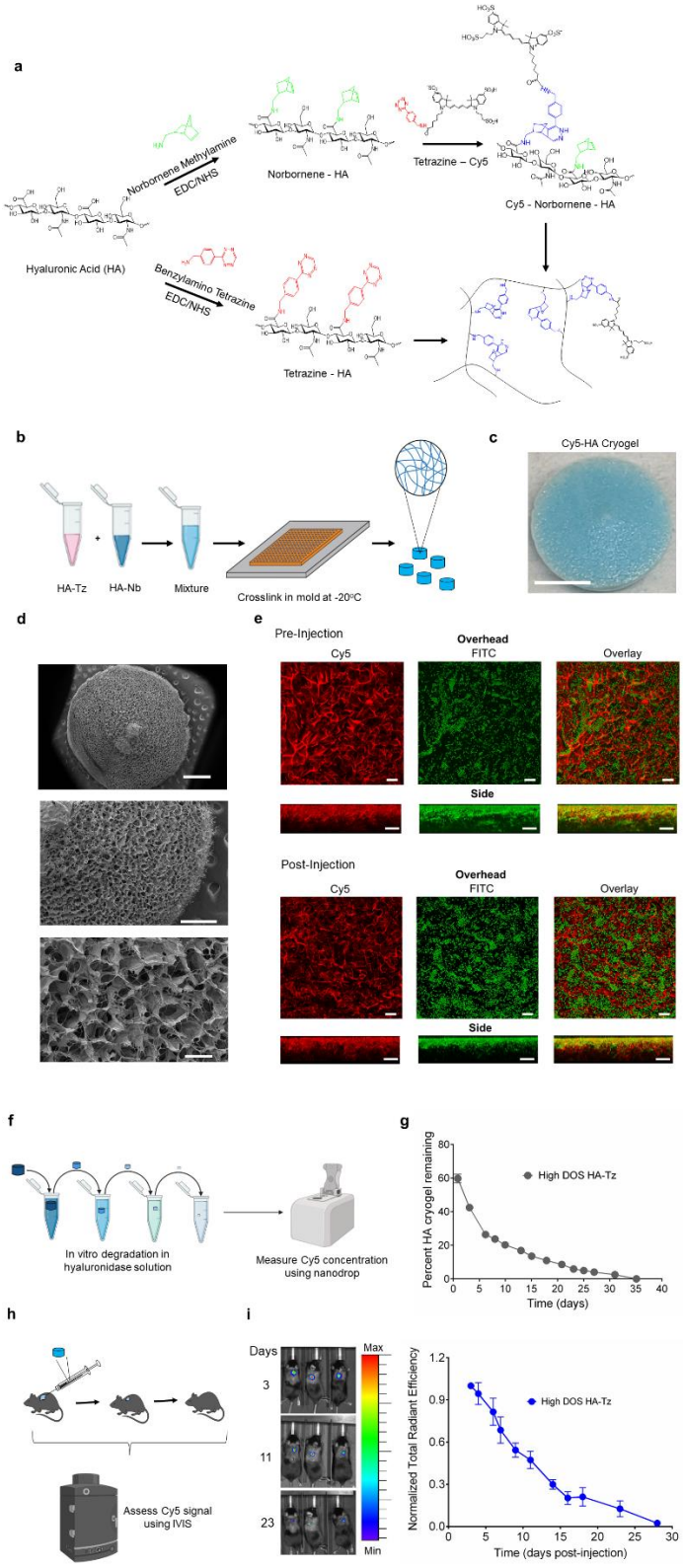
a
Norbornene Methylamine
EDC/NHS
Norbornene - HA
Tetrazine – Cy5
Cy5 - Norbornene - HA
Hyaluronic Acid (HA)
Benzylamino Tetrazine
EDC/NHS
Tetrazine - HA
b
HA-Tz
HA-Nb
Mixture
Crosslink in mold at -20°C
c
Cy5-HA Cryogel
d
e
Pre-Injection
Overhead
Cy5
FITC
Overlay
Side
Post-Injection
Overhead
Cy5
FITC
Overlay
Side
f
In vitro degradation in hyaluronidase solution
Measure Cy5 concentration using nanodrop
g
Percent HA cryogel remaining
High DOS HA-Tz
Time (days)
h
Assess Cy5 signal using IVIS
i
Days
3
11
23
Max
Min
Normalized Total Radiant Efficiency
High DOS HA-Tz
Time (days post-injection)

Figure 2.2| Cy5-HA cryogel degradation in immunodeficient mice
Representative IVIS fluorescence images of Cy5-HA cryogel degradation and quantification by measuring total radiant efficiency normalized to initial day 3 timepoint of (**a**) untreated B6 mice, (**b**) neutrophil depleted B6 mice, (**c**) macrophage depleted B6 mice, and (**d**) NSG mice. IVIS Images are on the same scale and analyzed using Living Image Software. (**e**) Hematoxylin and eosin (H&E) stained histological sections of explanted Cy5-HA cryogels from the above groups, at days 1, 5, and 10 post-injection. Full view scale bar = 800μm, magnified scale bar = 100μm. (**f**) Quantification of cellular density in the sections from **e**. Data in **a**-**d** represent mean ± s.e.m. of n=4-9 and are representative of at least two separate experiments. Data in **f** represents mean ± s.d. of n=7-12 and were compared using student's t-test.

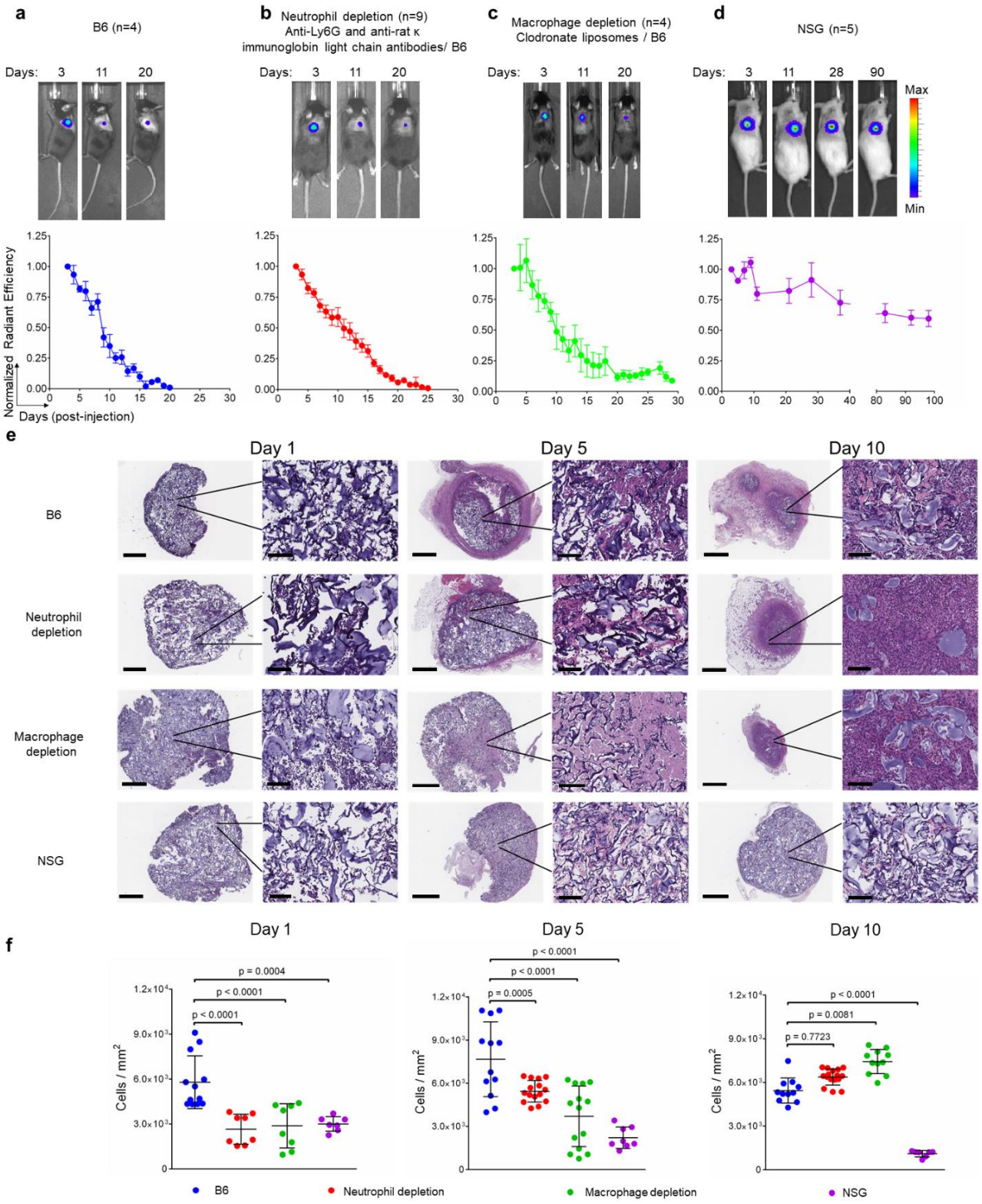
a
B6 (n=4)
b
Neutrophil depletion (n=9)
Anti-Ly6G and anti-rat κ
immunoglobin light chain antibodies/ B6
c
Macrophage depletion (n=4)
Clodronate liposomes / B6
d
NSG (n=5)
Days: 3 11 20
Days: 3 11 20
Days: 3 11 20
Days: 3 11 28 90
Max
Min
Normalized Radiant Efficiency
Days (post-injection)
e
Day 1
Day 5
Day 10
B6
Neutrophil depletion
Macrophage depletion
NSG
f
Day 1
Day 5
Day 10
Cells / mm2
p = 0.0004
p < 0.0001
p < 0.0001
p < 0.0001
p < 0.0001
p = 0.0005
p < 0.0001
p = 0.0081
p = 0.7723
B6
Neutrophil depletion
Macrophage depletion
NSG

Figure 2.3| Assessment of innate immune cell infiltration into Cy5-HA cryogels
(**a**) Schematic for the quantification of innate immune cell content in Cy5-HA cryogels. (**b**) Representative flow cytometry plots depicting gating strategy to determine cellular identity of $CD45^+$ $CD11b^+$ $F4/80^+$ (macrophage) cells, $CD45^+$ $CD11b^+$ $F4/80^-$ $Ly6G^+$ (neutrophil) cells, and $CD45^+$ $CD11b^+$ $F4/80^-$ $Ly6G^-$ $CD115^+$ (monocyte) cells in untreated B6 mice, anti-Ly6G and anti-rat κ immunoglobulin light chain antibody treated B6 mice, clodronate liposome treated B6 mice, and NSG mice. **c-e** Quantification of total number of (**c**) $CD45^+$ $CD11b^+$ (myeloid) cells, (**d**) macrophages, and (**e**) neutrophils infiltrating HA cryogels in untreated B6 mice, anti-Ly6G and anti-rat κ immunoglobulin light chain antibody treated B6 mice, clodronate liposome treated B6 mice, and NSG mice. (**f**) Infiltrating immune cell lineages plotted as a percentage of myeloid cells in untreated, neutrophil depleted, macrophage depleted, and NSG mice. (**g**) Schematic depicting workflow for in vivo Cy5-HA cryogel degradation study with $gp91^{phox-}$ mice. (**h**) Representative IVIS fluorescence images of gel degradation and quantification by measuring total radiant efficiency normalized to initial day 3 timepoint of $gp91^{phox-}$ mice and B6 mice. IVIS Images are on the same scale and analyzed using Living Image Software. Data in **c**, **d**, **e**, **f** represents mean ± s.d. of n=7-10 Cy5-HA cryogels, are representative of at least two separate experiments. Data in **c**, **d**, **e** were compared using student's t-test. Data in **h** represents mean ± s.e.m. of n=4-5 and were compared using two-way ANOVA with Bonferroni's multiple comparison test. Parts of figures **3a and h** were created with BioRender.com.

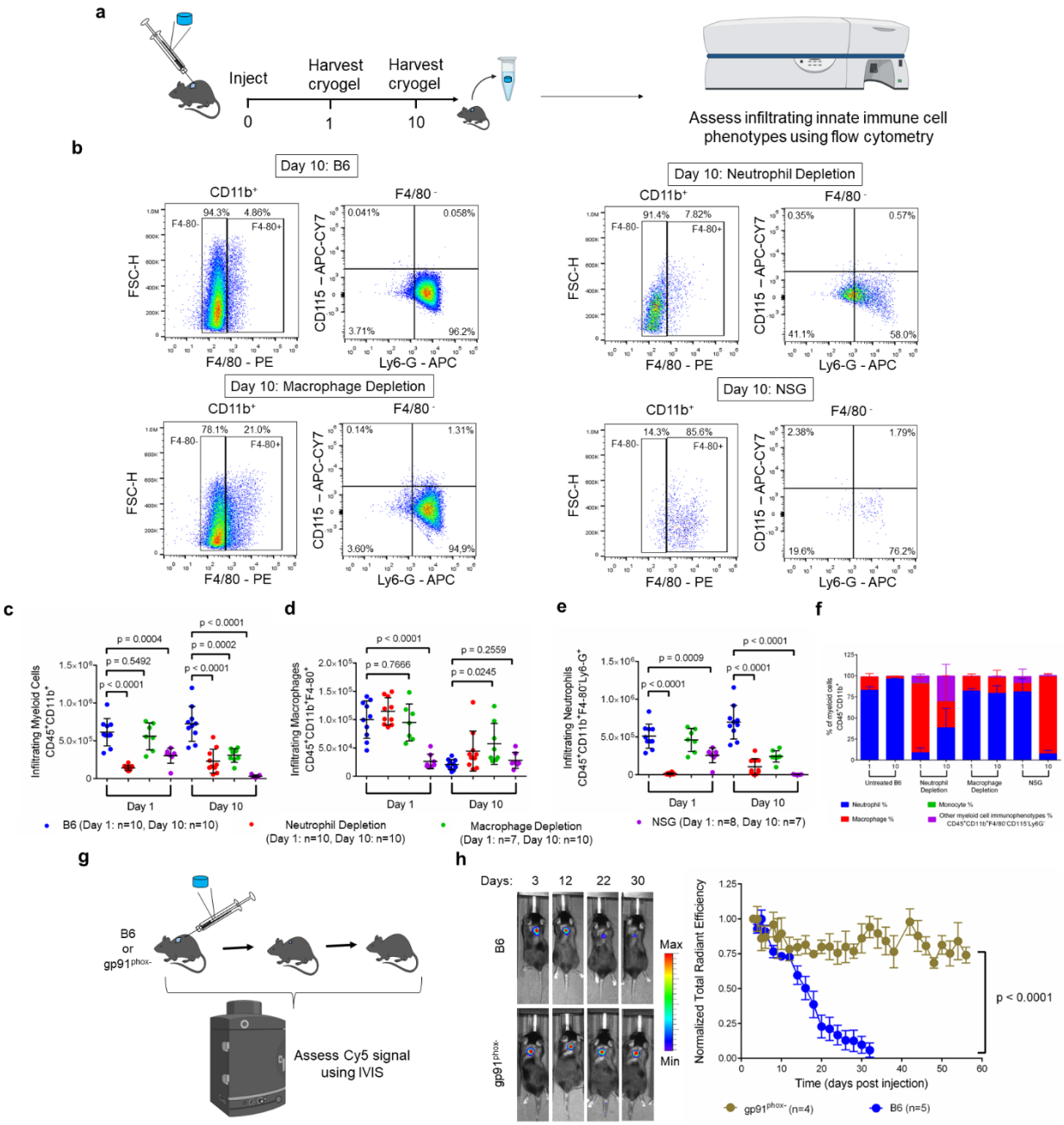
a
Inject
Harvest cryogel
Harvest cryogel
0
1
10
Assess infiltrating innate immune cell phenotypes using flow cytometry
b
Day 10: B6
Day 10: Neutrophil Depletion
Day 10: Macrophage Depletion
Day 10: NSG
CD11b+
F4/80 -
F4-80-
F4-80+
FSC-H
F4/80 - PE
CD115 – APC-CY7
Ly6-G - APC
c
Infiltrating Myeloid Cells CD45+CD11b+
Day 1
Day 10
B6 (Day 1: n=10, Day 10: n=10)
Neutrophil Depletion (Day 1: n=10, Day 10: n=10)
Macrophage Depletion (Day 1: n=7, Day 10: n=10)
d
Infiltrating Macrophages CD45+CD11b+F4-80+
e
Infiltrating Neutrophils CD45+CD11b+F4-80+Ly6-G+
NSG (Day 1: n=8, Day 10: n=7)
f
Untreated B6
Neutrophil Depletion
Macrophage Depletion
NSG
Neutrophil %
Macrophage %
Monocyte %
g
B6 or gp91phox-
Assess Cy5 signal using IVIS
h
Days: 3 12 22 30
B6
gp91phox-
Max
Min
Normalized Total Radiant Efficiency
Time (days post injection)
p < 0.0001
gp91phox- (n=4)
B6 (n=5)

Figure 2.4| Degradation kinetics of HA cryogels is impaired during transient immunodeficiency following HSCT

(**a**) Schematic depicting workflow for quantification of Cy5-HA cryogel degradation and innate immune cell infiltration in control (non-irradiated mice that do not receive a transplant) and post-HSCT B6 mice. (**b**) Representative IVIS fluorescence images of gel degradation in non-irradiated and post-HSCT mice. Tracking gel degradation by quantification of total radiant efficiency normalized to initial day 3 timepoint. (**c**) Photograph of Cy5-HA cryogels in non-irradiated mice 5- and 16-days post-injection and post-HSCT mice on days 5, 16, 21, and 26. **d-f** Cell infiltration of (**d**) $CD45^+CD11b^+$ (myeloid) cells, (**e**) $CD45^+CD11b^+$ $F4/80^+$ (macrophage) cells, and (**f**) $CD45^+$ $CD11b^+$ $F4/80^-$ $Ly6G^+$ (neutrophil) cells into HA cryogels in non-irradiated mice 5- and 16-days post-injection and 5-, 16-, 21-, and 26- days post-HSCT. Data in **b** represents mean ± s.e.m. of n = 7-9 mice and is representative of at least two separate experiments. Data in **d**, **e**, **f** represents mean ± s.d. of n = 6-10 HA cryogels and are representative of at least two separate experiments. Data in **b** were compared using two-way ANOVA with Bonferroni's multiple comparison test. Data in **d**, **e**, **f** were compared using student's t-test. Part of figure **4a** was created with BioRender.com.

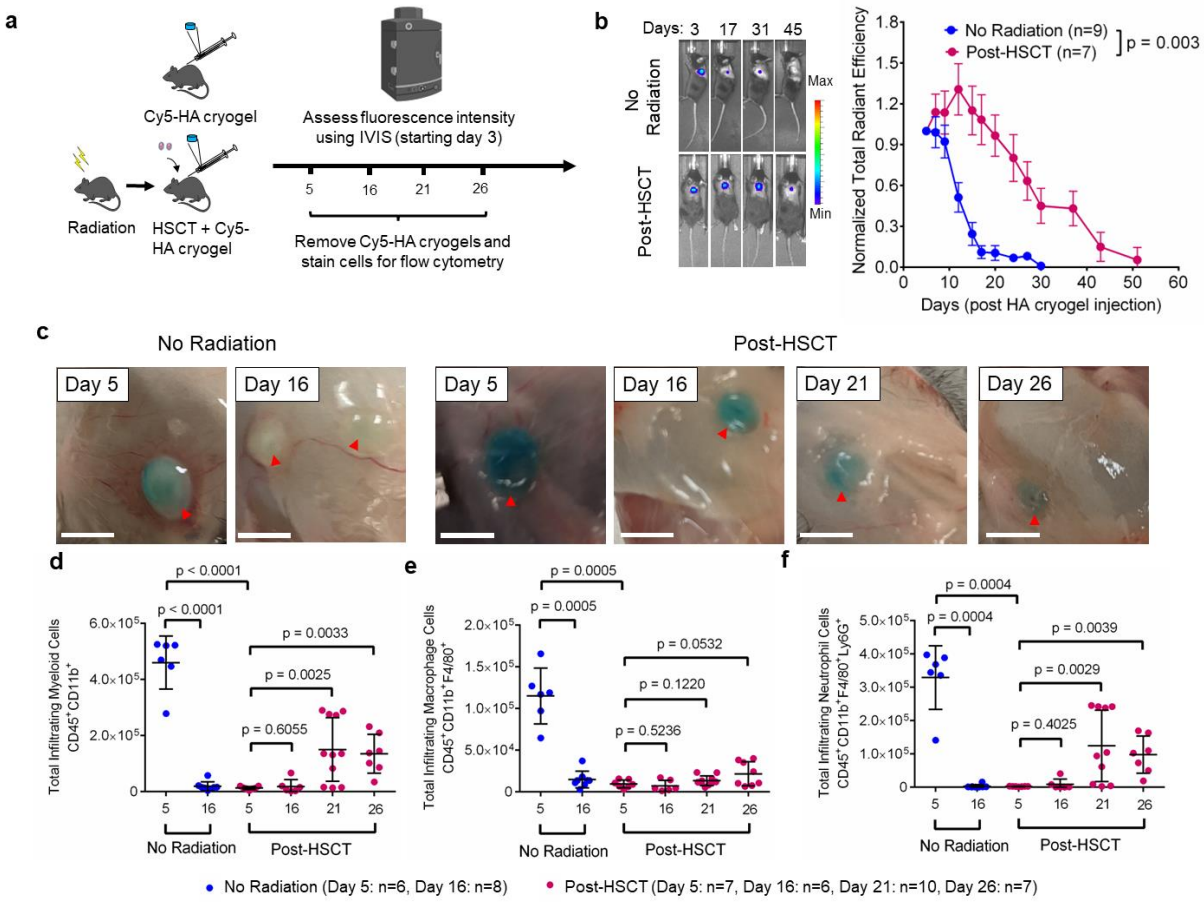
a
Cy5-HA cryogel
Radiation
HSCT + Cy5-HA cryogel
Assess fluorescence intensity using IVIS (starting day 3)
5
16
21
26
Remove Cy5-HA cryogels and stain cells for flow cytometry
b
Days: 3 17 31 45
No Radiation
Post-HSCT
Max
Min
No Radiation (n=9)
Post-HSCT (n=7)
p = 0.003
Normalized Total Radiant Efficiency
Days (post HA cryogel injection)
c
No Radiation
Post-HSCT
Day 5
Day 16
Day 5
Day 16
Day 21
Day 26
d
Total Infiltrating Myeloid Cells CD45+CD11b+
p < 0.0001
p < 0.0001
p = 0.0033
p = 0.0025
p = 0.6055
No Radiation
Post-HSCT
e
Total Infiltrating Macrophage Cells CD45+CD11b+F4/80+
p = 0.0005
p = 0.0005
p = 0.0532
p = 0.1220
p = 0.5236
No Radiation
Post-HSCT
f
Total Infiltrating Neutrophil Cells CD45+CD11b+F4/80+Ly6G+
p = 0.0004
p = 0.0004
p = 0.0039
p = 0.0029
p = 0.4025
No Radiation
Post-HSCT
No Radiation (Day 5: n=6, Day 16: n=8)
Post-HSCT (Day 5: n=7, Day 16: n=6, Day 21: n=10, Day 26: n=7)

Figure 2.5| Enhanced reconstitution of peripheral blood neutrophil cells
(**a**) Schematic depicting outline of study to quantify Cy5 G-CSF release from HA cryogels in non-irradiated, non-transplanted B6 mice and post-HSCT B6 mice. (**b**) Representative IVIS fluorescence images of Cy5 G-CSF release from HA cryogels and quantification by measuring total radiant efficiency normalized to initial 8-hour timepoint. IVIS Images are on the same scale and analyzed using Living Image Software. (**c**) Time to 50% fluorescence intensity for Cy5 G-CSF encapsulated within HA cryogels in non-irradiated and post-HSCT mice. (**d**) Schematic depicting outline of study to quantify neutrophil reconstitution rate and Cy5-HA cryogel degradation rate in post-HSCT mice using G-CSF encapsulated Cy5-HA cryogels. (**e**) Peripheral blood reconstitution of neutrophils in post-HSCT mice, normalized to pre-irradiation neutrophil counts from a random subset of mice. (**f**) Representative in vivo imaging system (IVIS) fluorescence images of gel degradation in mice and measuring Cy5-HA cryogel degradation in vivo by quantification of total radiant efficiency normalized to initial day 3 timepoint. IVIS Images are on the same scale and analyzed using Living Image Software. Data in **b** represents mean ± s.e.m. of n = 6-9 mice. Data in **c** represents mean ± s.d. of n = 6 – 9 mice. Data in **e** represents mean ± s.d. of n = 11-15 mice and is representative of at least two separate experiments. Data in **f** represents ± s.e.m. of n = 11-14 Cy5-HA cryogels and is representative of at least two separate experiments. Data in **b, f** were compared using two-way ANOVA with Bonferroni's multiple comparison test. Data in **c** were compared using student's t-test. Data in **e** were compared using mixed-effect regression model with random intercepts.

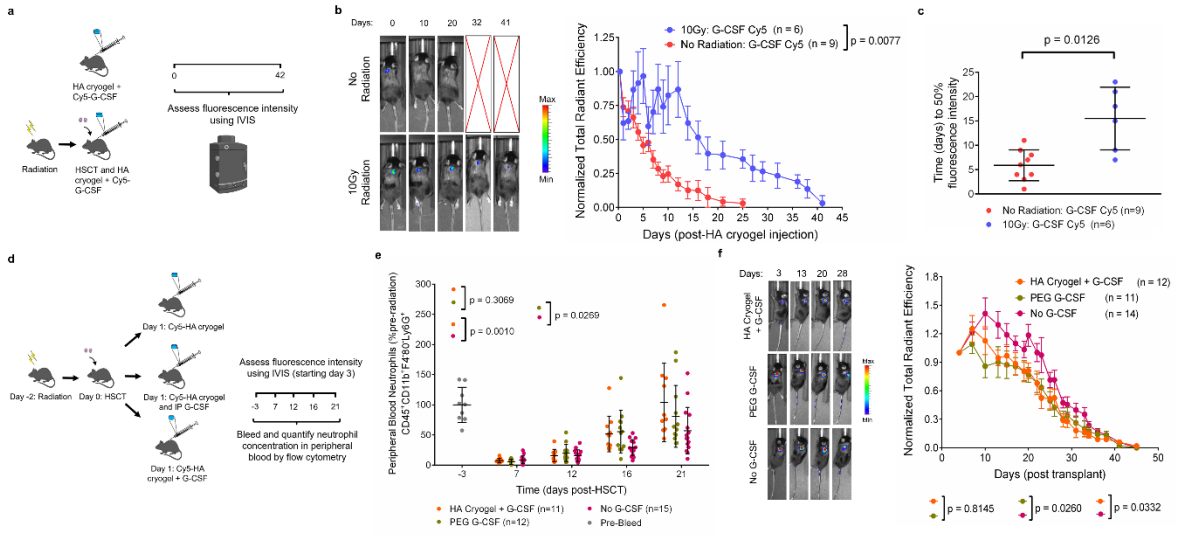

2.5 Appendix

Figure 2.S1| Supplementary HA cryogel materials characterization data
(**a**) Volumetric swelling ratios for low- and high-DOS Cy5-HA cryogels. (**b**) Aqueous weight percentage of low- and high-DOS Cy5-HA cryogels. (**c**) Representative SEM image depicting low-DOS Cy5-HA cryogels. Top scale bar = 500μm, bottom scale bar = 100μm. (**d**) Average pore diameters of HA cryogels made from low- and high-DOS Cy5-HA cryogels measured from SEM images (20 measurements/cryogel, n = 3 each for low- and high-DOS HA cryogels). (**e**) Confocal microscopy images, overhead and side views, depicting low-DOS Cy5-HA cryogels both pre-injection and post-injection incubated with 10μm FITC-labeled microparticles. Scale bar = 100μm. (**f**) Quantification of confocal images showing penetration of 10μm FITC-labeled microparticles into both low- and high-DOS Cy5-HA cryogels pre- and post-injection. (**g**) Representative confocal microscopy images of low- and high-DOS Cy5-HA cryogels after thawing, after lyophilization, and after lyophilization and rehydration. (**h**) Average surface pore diameter of Cy5-HA cryogels measured from confocal images. Data in **a** and **b** represents mean ± s.d. of n=10 Cy5-HA cryogels. Data in **d** represents mean ± s.d. of n=3 Cy5-HA cryogels and was compared using student's t-test. Data in **f** represents mean ± s.d. of n=5 Cy5-HA cryogels. Data in **h** represents mean ± s.d. of n=3 HA cryogels and was compared using student's t-test.

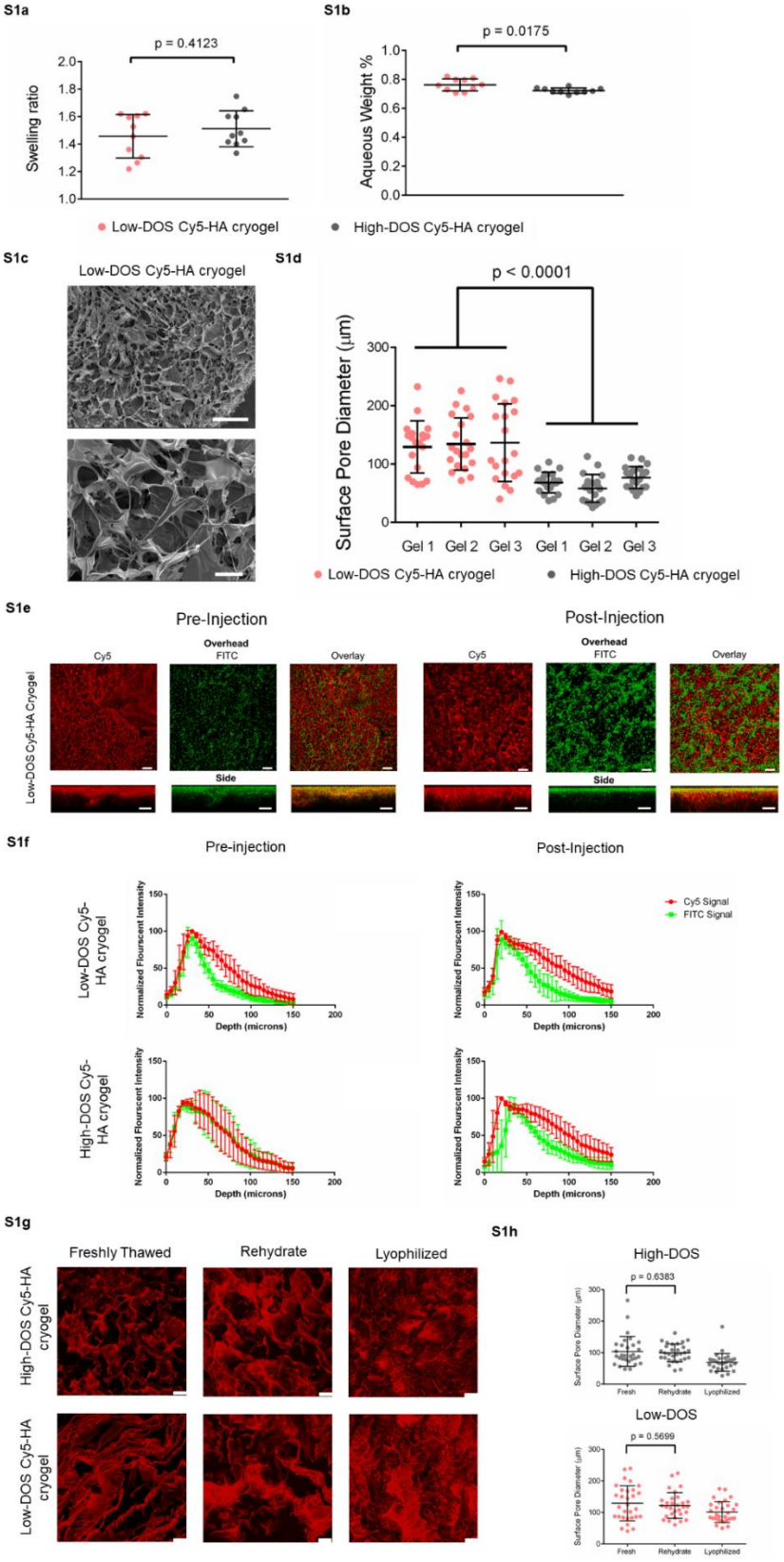
S1a
p = 0.4123
Swelling ratio
2.0
1.8
1.6
1.4
1.2
1.0
Low-DOS Cy5-HA cryogel
S1b
p = 0.0175
Aqueous Weight %
1.0
0.8
0.6
0.4
0.2
0.0
High-DOS Cy5-HA cryogel
S1c
Low-DOS Cy5-HA cryogel
S1d
p < 0.0001
Surface Pore Diameter (μm)
300
200
100
0
Gel 1
Gel 2
Gel 3
Gel 1
Gel 2
Gel 3
Low-DOS Cy5-HA cryogel
High-DOS Cy5-HA cryogel
S1e
Pre-Injection
Post-Injection
Cy5
Overhead
FITC
Overlay
Side
Low-DOS Cy5-HA Cryogel
S1f
Pre-injection
Post-Injection
Low-DOS Cy5-HA cryogel
High-DOS Cy5-HA cryogel
Normalized Flourscent Intensity
Depth (microns)
Cy5 Signal
FITC Signal
S1g
Freshly Thawed
Rehydrate
Lyophilized
High-DOS Cy5-HA cryogel
Low-DOS Cy5-HA cryogel
S1h
High-DOS
p = 0.6383
Low-DOS
p = 0.5699
Surface Pore Diameter (μm)
Fresh
Rehydrate
Lyophilized

Figure 2.S2| Supplementary Cy5-HA cryogel degradation characterization data (**a**) Measuring low-DOS Cy5-HA cryogel degradation in vitro in hyaluronidase-2 (HYAL2) solution by quantification of Cy5-signal in supernatant at pre-determined timepoints normalized to total Cy5-signal in supernatant across all timepoints. (**b**) Representative IVIS fluorescence images of gel degradation in mice and measuring low-DOS Cy5-HA cryogel degradation in vivo by quantification of total radiant efficiency normalized to the initial day 3 timepoint. (**c**) Measuring Cy5-HA cryogel degradation by quantification of total radiant efficiency normalized to initial day 3 timepoint. Data in **a** represents mean ± s.d. of n=4 HA cryogels. Data in **b** represents mean ± s.e.m. of n=4 HA cryogels. Data in **c** represents mean ± s.d. of n=4-5 HA cryogels and were compared using two-way ANOVA with Bonferroni's multiple comparison test.

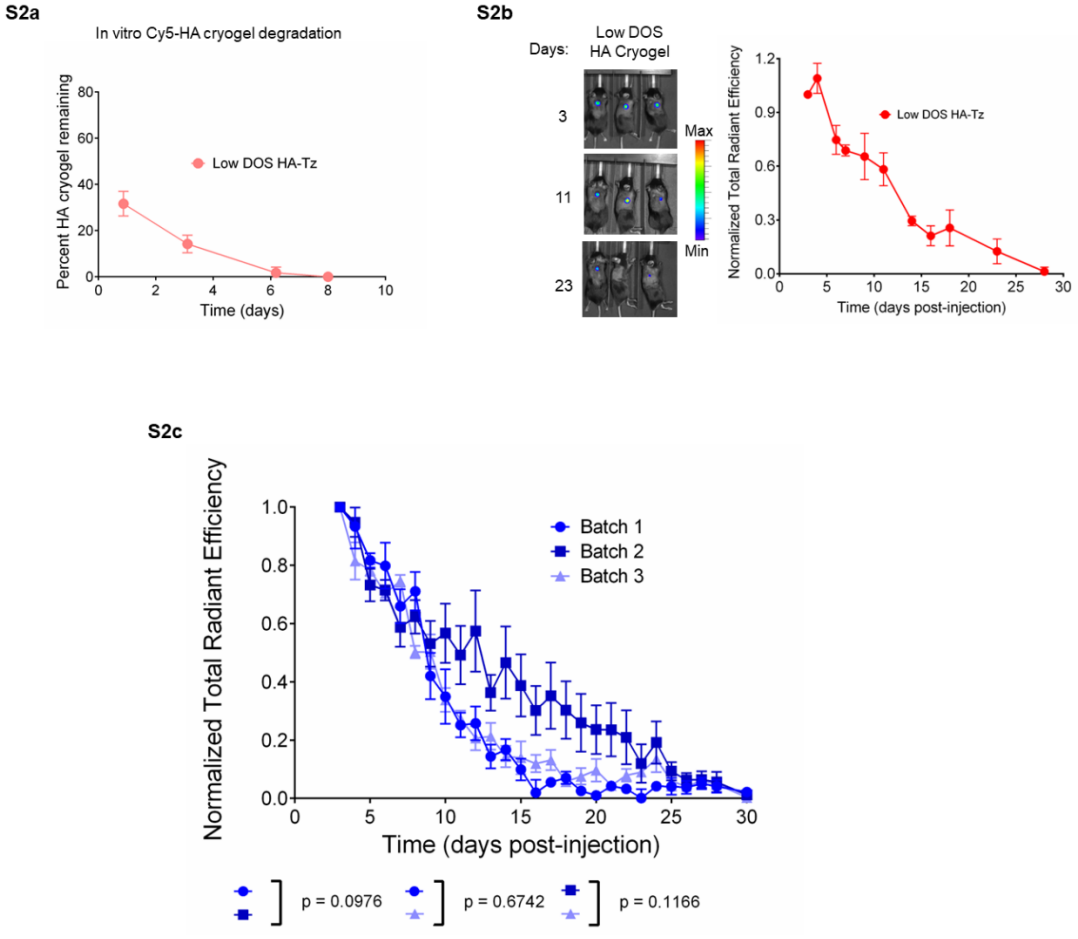

Figure 2.S3| Supplementary Cy5-HA cryogel degradation in immunodeficient mice characterization data

Representative IVIS fluorescence images of gel degradation and quantification by measuring total radiant efficiency normalized to initial day 3 timepoint of (a) T cell depleted B6 mice and (b) B cell depleted B6 mice. c-d Representative gating strategy to determine identity of (c) innate immune cells and (d) adaptive immune cells in peripheral blood. (e) Representative flow cytometry plot of peripheral blood neutrophils pre- and post-administration of neutrophil depleted mice and (f) peripheral blood neutrophil concentration. (g) Representative flow cytometry plot of peripheral blood monocytes pre- and post- administration clodronate liposomes to mice and (h) peripheral blood monocyte concentration. (i) Representative flow cytometry plot of peripheral blood T cells blood pre- and post- administration of anti-CD4 and anti-CD8 antibody treatment to mice and (j) peripheral blood T cell concentration. (k) Representative flow cytometry plot of peripheral blood B cells blood pre- and post- administration of anti-B220 antibody treatment to B6 mice and (l) peripheral blood B cell concentration. (m) Overlay of normalized total radiant efficiency curves and time to 50% fluorescence intensity of untreated B6, neutrophil depleted, macrophage depleted, T cell depleted, and B cell depleted mice. (n) Photograph of a Cy5-HA cryogel retrieved from NSG mice 3 months post-injection. Data in a, b represents mean ± s.e.m. of n=5 and are representative of at least two separate experiments. Data in f, h, j, l represents mean ± s.d. of n=4-5. Data in m represents mean ± s.d. of n=4-9 and were compared using student's t-test.

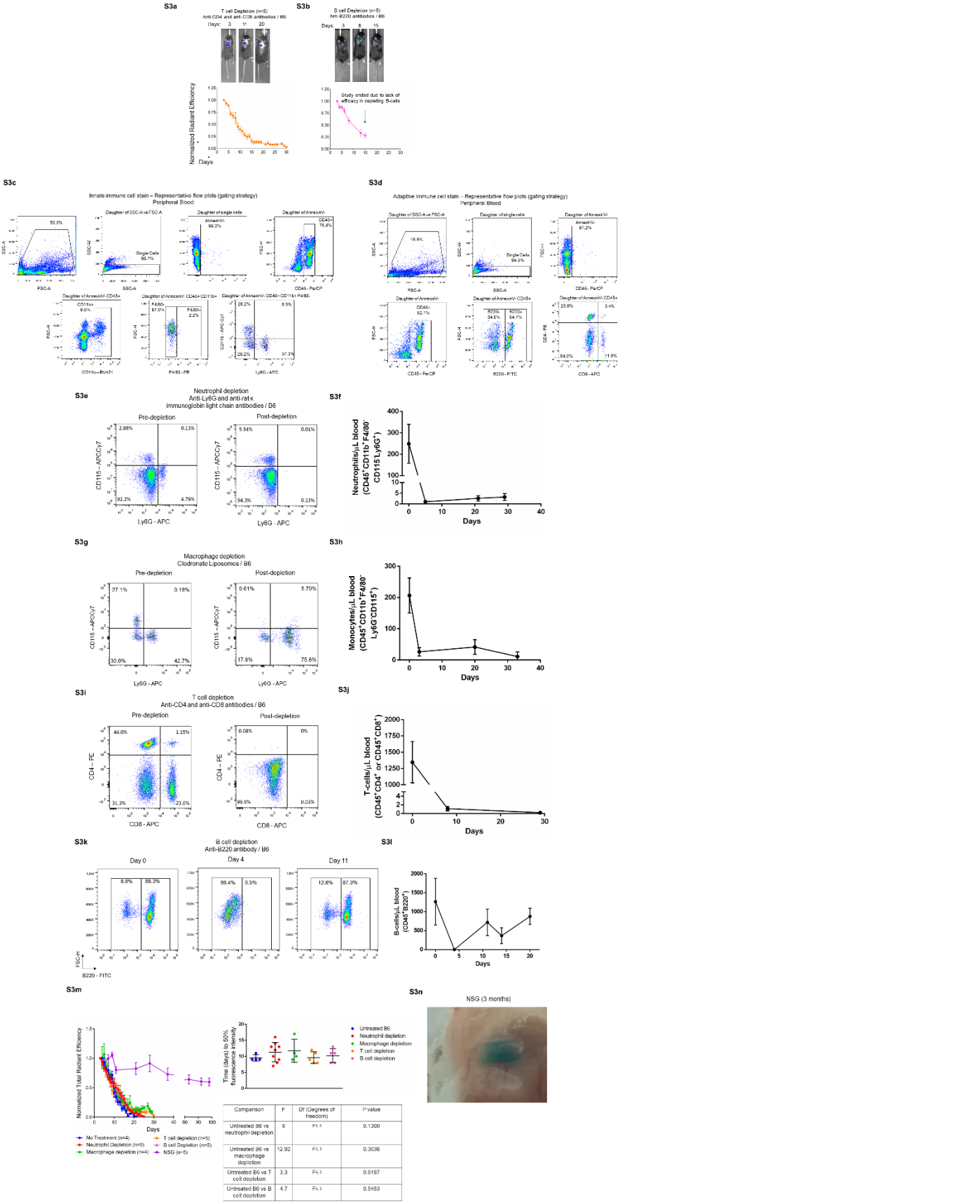

Comparison	F	Df (Degrees of freedom)	P value
Untreated B6 vs neutrophil depletion	9	F8,8	0.1300
Untreated B6 vs macrophage depletion	12.92	F3,3	0.3036
Untreated B6 vs T cell depletion	3.3	F4,3	0.9197
Untreated B6 vs B cell depletion	4.7	F4,3	0.5453

Figure 2.S4| Supplementary histomorphometric analysis of Cy5-HA cryogels retrieved from T- and B- cell depleted mice

(**a**) Hematoxylin and eosin (H&E) stain of explanted Cy5-HA cryogels from T cell depleted and B cell depleted mice at days 1, 5, and 10. Scale bar left = 800μm, scale bar right = 100μm. (**b**) Analysis of H&E stains to quantify cellular density in Cy5-HA cryogel. Data in **b** represents mean ± s.d. of n = 7-12 histological sections and was compared using student's t-test.

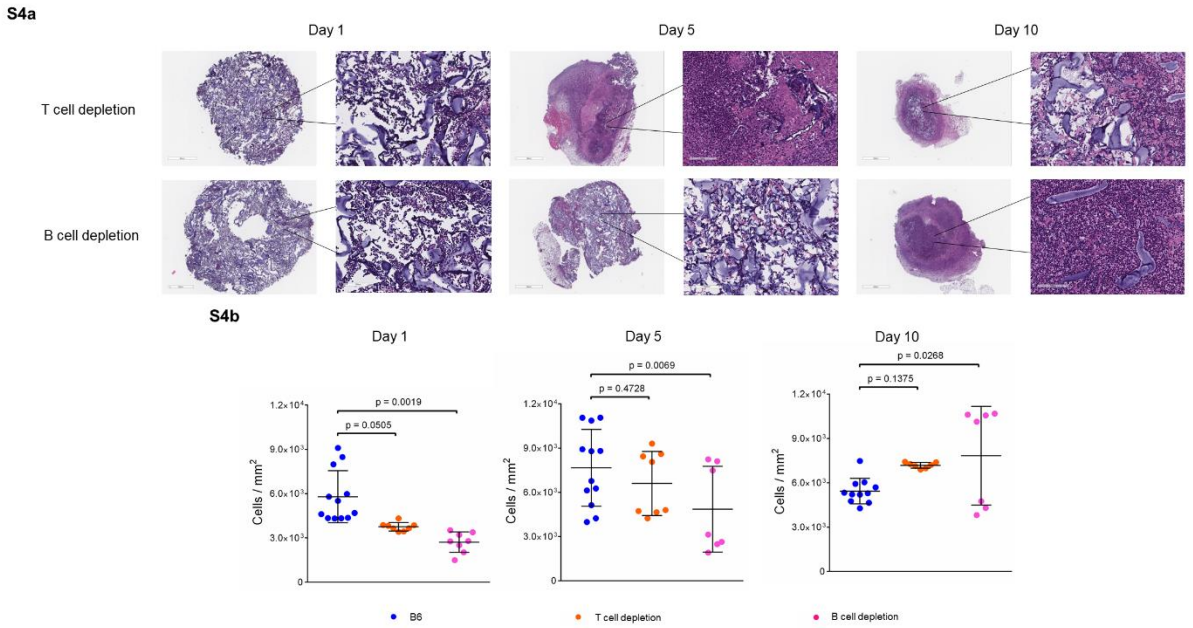

Figure 2.S5| Supplementary analysis of myeloid cell infiltration of Cy5-HA cryogels retrieved from immunodeficient mice

(**a**) Representative gating strategy to determine identity of innate immune cell infiltrates of HA cryogel. (**b**) Representative flow cytometry plots gated to determine cellular identity of $CD45^+$ $CD11b^+$ $F4/80^+$ (macrophage) cells, $CD45^+$ $CD11b^+$ $F4/80^-$ $Ly6G^+$ (neutrophil) cells, and $CD45^+$ $CD11b^+$ $F4/80^-$ $Ly6G^-$ $CD115^+$ (monocyte) cells T cell depleted and B cell depleted mice. (**c**) Percent of $AnnexinV^-$ (live) cells within Cy5-HA cryogels one and ten days after implant from flow cytometry analysis. **d-e** Quantification of total number of (**d**) myeloid cells and (**e**) macrophages infiltrating Cy5-HA cryogels in untreated B6 mice, T cell depleted mice, and B cell depleted mice. (**f**) Representative flow cytometry plots from neutrophil depleted mice with and without intracellular Ly6G staining. Plotted data assessing neutrophils as a percentage of total myeloid cells ($CD45^+CD11b^+$) with and without intracellular Ly6G staining. (**g**) Quantification of total number of neutrophils infiltrating Cy5-HA cryogels in untreated B6 mice, T cell depleted mice, and B cell depleted mice. **h,i** Quantification of total number of (**h**) monocytes and (**i**) infiltrating immune cell lineages plotted as a percentage of myeloid cells in untreated, T cell depleted, and B cell depleted mice. Data in **e** represents mean ± s.d. of n = 10. Data in **c, d, e, g, h, i** represents mean ± s.d. of n = 7-10 and are representative of at least two separate experiments. Data in **d, e, f, g** were compared using student's t-test.

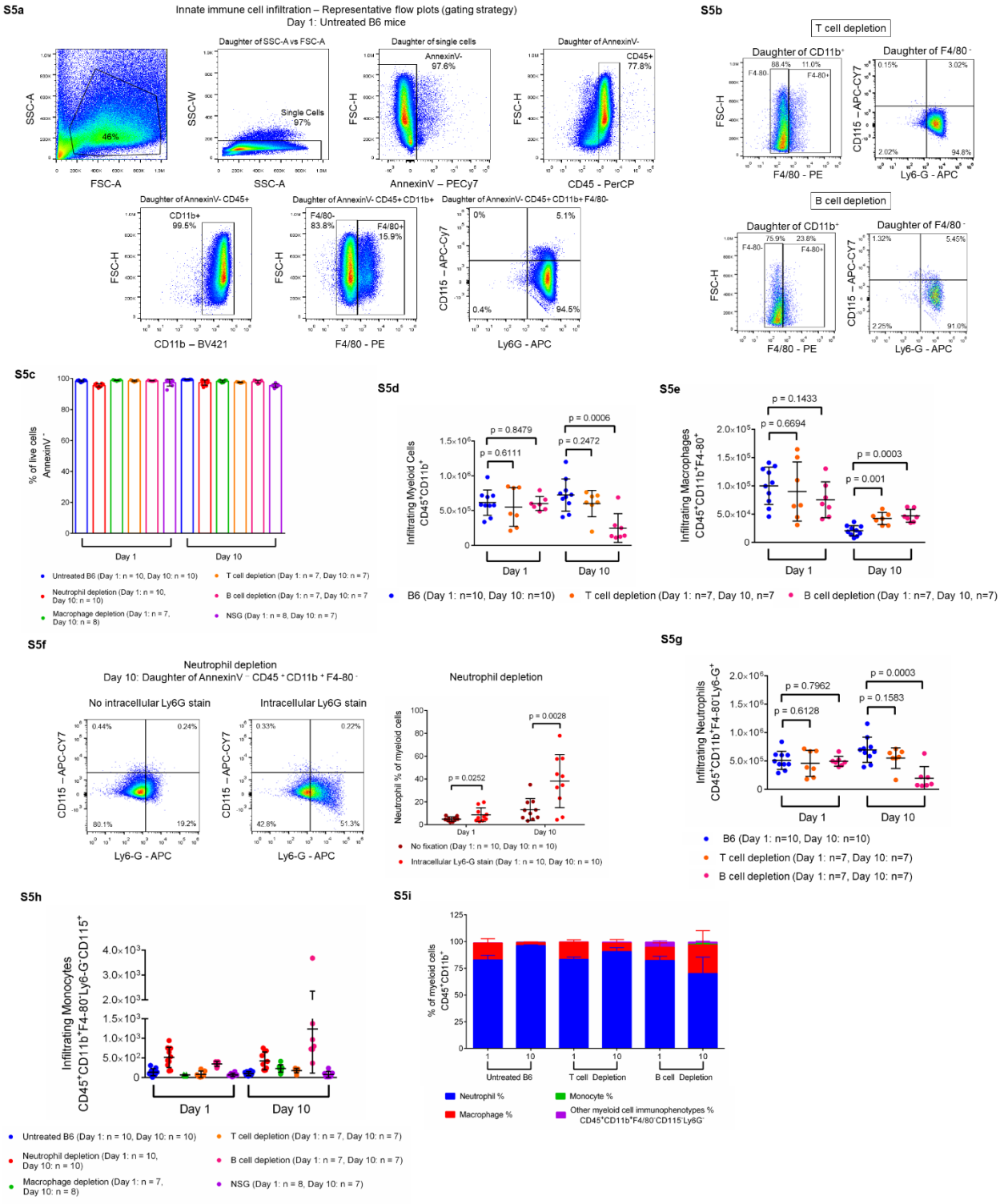
S5a
Innate immune cell infiltration – Representative flow plots (gating strategy)
Day 1: Untreated B6 mice
Daughter of SSC-A vs FSC-A
Daughter of single cells
Daughter of AnnexinV-
Daughter of AnnexinV- CD45+
Daughter of AnnexinV- CD45+ CD11b+
Daughter of AnnexinV- CD45+ CD11b+ F4/80-
SSC-A
FSC-A
SSC-W
FSC-H
AnnexinV – PECy7
CD45 - PerCP
CD11b – BV421
F4/80 - PE
Ly6G - APC
CD115 – APC-CY7
S5b
T cell depletion
B cell depletion
Daughter of CD11b+
Daughter of F4/80-
F4/80 - PE
Ly6-G - APC
S5c
% of live cells AnnexinV-
Day 1
Day 10
Untreated B6 (Day 1: n = 10, Day 10: n = 10)
T cell depletion (Day 1: n = 7, Day 10: n = 7)
Neutrophil depletion (Day 1: n = 10, Day 10: n = 10)
B cell depletion (Day 1: n = 7, Day 10: n = 7
Macrophage depletion (Day 1: n = 7, Day 10: n = 8)
NSG (Day 1: n = 8, Day 10: n = 7)
S5d
Infiltrating Myeloid Cells CD45+CD11b+
p = 0.8479
p = 0.6111
p = 0.0006
p = 0.2472
S5e
Infiltrating Macrophages CD45+CD11b+F4-80+
p = 0.1433
p = 0.6694
p = 0.0003
p = 0.001
B6 (Day 1: n=10, Day 10: n=10)
T cell depletion (Day 1: n=7, Day 10, n=7
B cell depletion (Day 1: n=7, Day 10, n=7)
S5f
Neutrophil depletion
Day 10: Daughter of AnnexinV- CD45+ CD11b+ F4-80-
No intracellular Ly6G stain
Intracellular Ly6G stain
Neutrophil % of myeloid cells
p = 0.0252
p = 0.0028
No fixation (Day 1: n = 10, Day 10: n = 10)
Intracellular Ly6-G stain (Day 1: n = 10, Day 10: n = 10)
S5g
Infiltrating Neutrophils CD45+CD11b+F4-80-Ly6-G+
p = 0.7962
p = 0.6128
p = 0.0003
p = 0.1583
B6 (Day 1: n=10, Day 10: n=10)
T cell depletion (Day 1: n=7, Day 10: n=7)
B cell depletion (Day 1: n=7, Day 10: n=7)
S5h
Infiltrating Monocytes CD45+CD11b+F4-80-Ly6-G-CD115+
Day 1
Day 10
Untreated B6 (Day 1: n = 10, Day 10: n = 10)
T cell depletion (Day 1: n = 7, Day 10: n = 7)
Neutrophil depletion (Day 1: n = 10, Day 10: n = 10)
B cell depletion (Day 1: n = 7, Day 10: n = 7)
Macrophage depletion (Day 1: n = 7, Day 10: n = 8)
NSG (Day 1: n = 8, Day 10: n = 7)
S5i
% of myeloid cells CD45+CD11b+
Untreated B6
T cell Depletion
B cell Depletion
Neutrophil %
Monocyte %
Macrophage %
Other myeloid cell immunophenotypes % CD45+CD11b+F4/80-CD115-Ly6G-

Figure 2.S6| Supplementary Immunohistochemical staining of Cy5-HA cryogels retrieved from untreated B6 and NSG mice

(**a**) Immunohistochemistry (IHC) staining for Ly6G (neutrophils, top, scale bar = 1mm) and F4/80 (macrophages, bottom, scale bar = 60μm) of Cy5-HA cryogels excised from untreated B6 mice 1-, 5-, and 10-days after injection. IHC was conducted on the same Cy5-HA cryogels as in Fig. 2e. (**b**) IHC staining for Ly6G (top, scale bar = 1mm) and F4/80 (bottom, scale bar = 60μm) of Cy5-HA cryogels excised from macrophage depleted, neutrophil depleted, T cell depleted, and B cell depleted B6 mice 1-day after injection. IHC was conducted on the same Cy5-HA cryogels as in Fig. 2e. (**c**) IHC staining for Ly6G (top, scale bar = 1mm) and F4/80 (bottom, scale bar = 60μm) of Cy5-HA cryogels excised from NSG mice 1-, 5-, and 10-days after injection. IHC was conducted on the same Cy5-HA cryogels as in Fig. 2e.

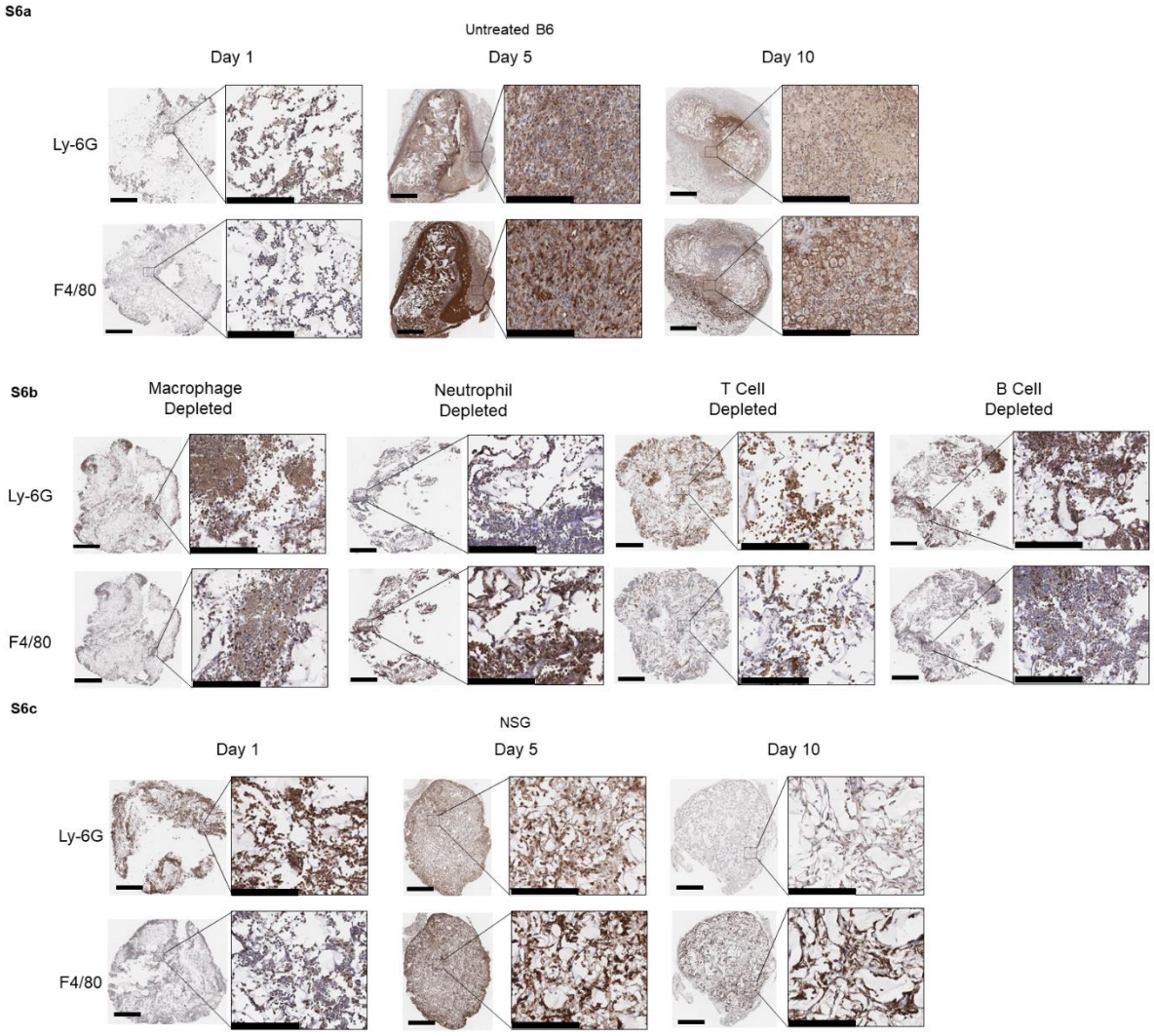

Figure 2.S7| Supplementary data for degradation kinetics of HA cryogels post-HSCT

(**a**) Representative flow cytometry plots of bone marrow before and after lineage depletion. (**b**) Time to 50% fluorescence intensity of Cy5-HA cryogels in non-irradiated and post-HSCT mice. (**c**) Percent of AnnexinV- (live) cells within Cy5-HA cryogels 5- and 16-days post injection in non-irradiated mice and 5-, 16-, 21-, and 26-days post-injection in post-HSCT mice. (**d**) Infiltrating immune cell lineages plotted as a percentage of myeloid cells in non-irradiated and post-HSCT mice. (**e**) Overlay of Cy5-HA cryogel degradation and neutrophil infiltration into in non-irradiated and post-HSCT mice from Fig. 4b, f. (**f**) Schematic for tetrazine (Tz) and norbornene (Nb) functionalization of oxidized alginate (OxAlg), Cy5 functionalization of Nb functionalized OxAlg, and crosslinking of Tz functionalized HA with Cy5 functionalized OxAlg. (**g**) Measuring Cy5-OxAlg cryogel degradation in vitro by quantifying the Cy5-signal in supernatant at pre-determined timepoints normalized to total Cy5-signal in supernatant across all timepoints. (**h**) Representative in vivo imaging system (IVIS) fluorescence images of gel degradation in mice and measuring Cy5-tagged 40% oxidized alginate cryogel degradation in vivo by quantification of total radiant efficiency normalized to initial 2-hour timepoint. IVIS Images are on the same scale and analyzed using Living Image Software. Data in **b** represents n=7-9 Cy5-HA cryogels, is representative of at least two separate experiments and were compared using student's t-test. Data in **c, d** represents mean ± s.d. of n=6-10 Cy5-HA cryogels and is representative of at least two separate experiments. Data in **g** represents mean ± s.d. of n=5 Cy5-OxAlg cryogels. Data in **h** represents mean ± s.e.m. of n=5 Cy5-OxAlg cryogels and were compared using two-way ANOVA with Bonferroni's multiple comparison test.

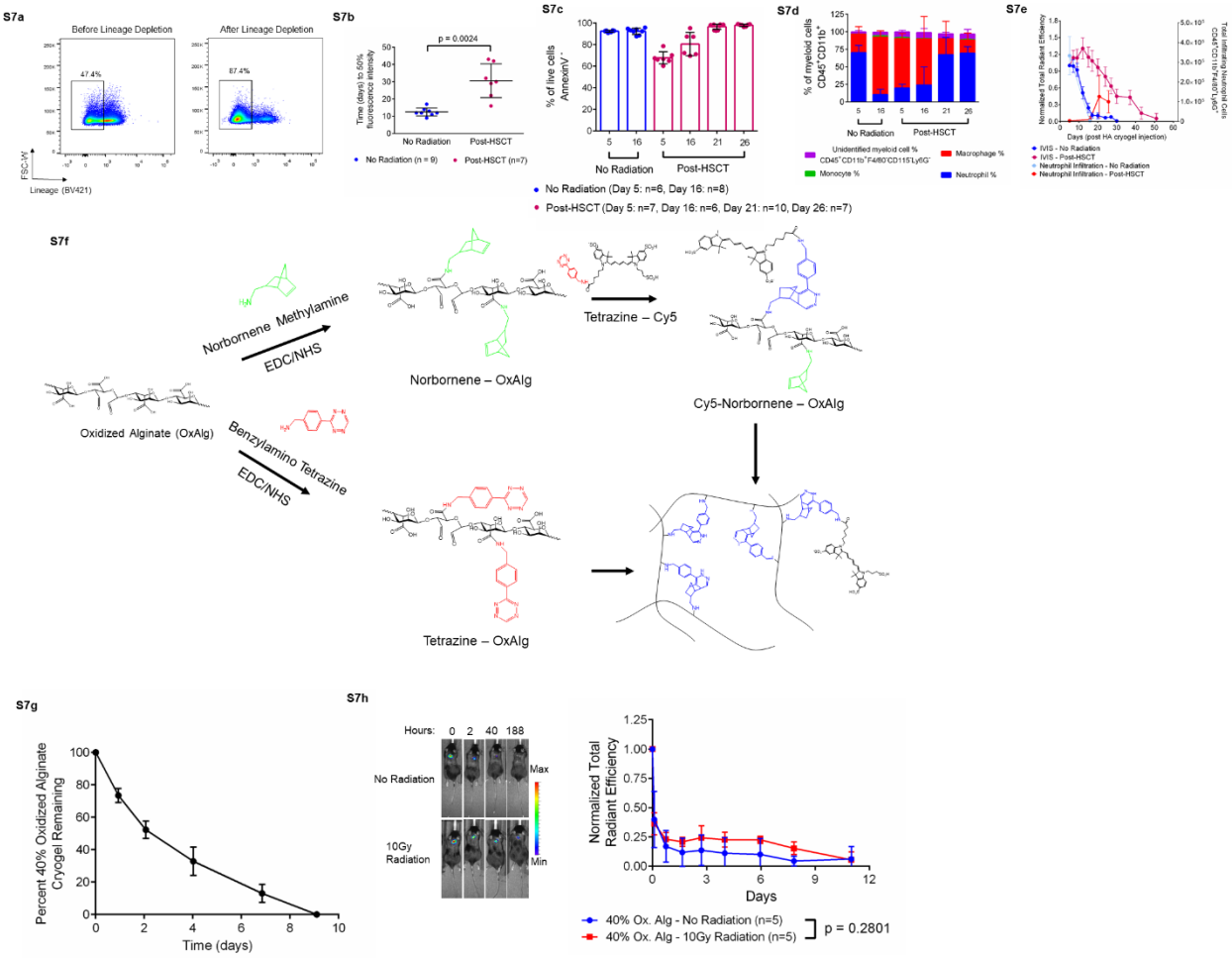
S7a
Before Lineage Depletion
After Lineage Depletion
47.4%
87.4%
FSC-W
Lineage (BV421)
S7b
p = 0.0024
Time (days) to 50% fluorescence intensity
No Radiation
Post-HSCT
No Radiation (n = 9)
Post-HSCT (n=7)
S7c
% of live cells AnnexinV-
No Radiation
Post-HSCT
No Radiation (Day 5: n=6, Day 16: n=8)
Post-HSCT (Day 5: n=7, Day 16: n=6, Day 21: n=10, Day 26: n=7)
S7d
% of myeloid cells CD45+CD11b+
Unidentified myeloid cell %
Macrophage %
Monocyte %
Neutrophil %
S7e
Normalized Total Radiant Efficiency
Days (post HA cryogel injection)
IVIS - No Radiation
IVIS - Post-HSCT
Neutrophil Infiltration - No Radiation
Neutrophil Infiltration - Post-HSCT
S7f
Norbornene Methylamine
EDC/NHS
Oxidized Alginate (OxAlg)
Benzylamino Tetrazine
EDC/NHS
Norbornene – OxAlg
Tetrazine – Cy5
Cy5-Norbornene – OxAlg
Tetrazine – OxAlg
S7g
Percent 40% Oxidized Alginate Cryogel Remaining
Time (days)
S7h
Hours: 0 2 40 188
No Radiation
10Gy Radiation
Max
Min
Normalized Total Radiant Efficiency
Days
40% Ox. Alg - No Radiation (n=5)
40% Ox. Alg - 10Gy Radiation (n=5)
p = 0.2801

Figure 2.S8| Supplementary data for enhanced reconstitution of peripheral blood neutrophil cells

Overlay of peripheral blood neutrophil recovery and Cy5-HA cryogel degradation in post-HSCT mice from Fig. 5 e, f.

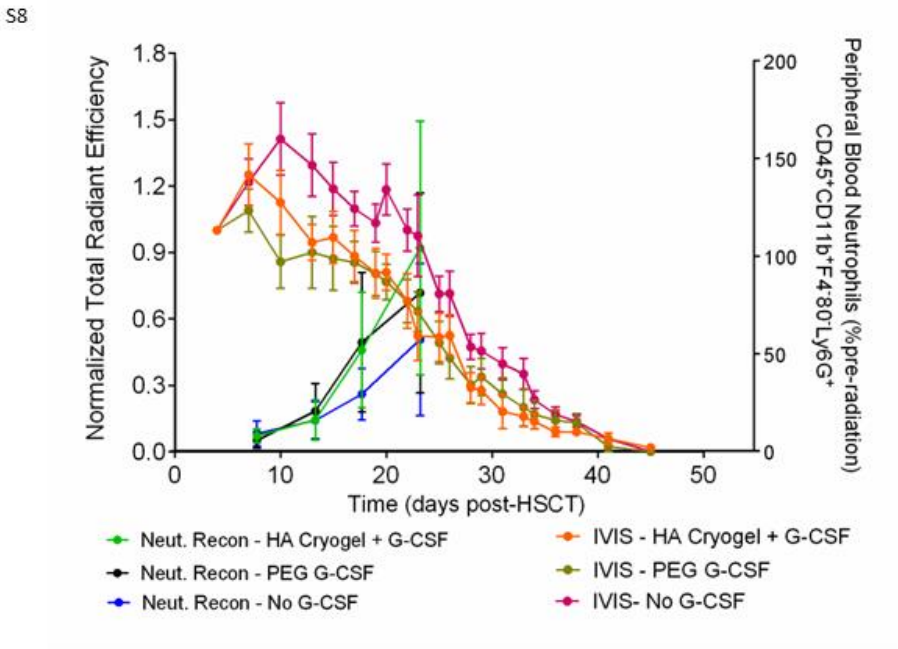

Supplementary Table 2.1

Material	Sample 1 (EU/mL)	Sample 2 (EU/mL)	Sample 3 (EU/mL)
HA-Tz	0.332	0.367	0.362
Cy5-HA-Nb	0.227	0.23	0.229
HA Cryogel Average Endotoxin Content	0.00874 EU		
EU/kg (2 HA cryogels/mouse)	0.874 EU/kg		

Supplementary Table 2.2

Depletion Type	Depletion Agent	Dose, Administration Route, Frequency	Depletion Efficiency
Neutrophil Depletion	Anti-mouse Ly6G antibody (1A8, Bio X Cell) Anti-rat kappa immunoglobulin light chain antibody (MAR 18.5, Bio X Cell)	25µL anti-mouse Ly6G – IP administration – Everyday for 1 week 50µL anti-mouse Ly6G – IP administration – Everyday after first week 50µL anti-rat kappa immunoglobulin light chain – IP administration – Every other day	Consistent – 98% Depletion of neutrophils in peripheral blood (Supplemental 5b, 5c)
Macrophage/Monocyte Depletion	Clodronate Liposomes (Liposoma)	100µL – IP administration – 2x/week	Consistent – 80-95% Depletion of neutrophils in peripheral blood (Supplemental 5d, 5e)
T-cell Depletion	Anti-mouse CD4 antibody (GK1.5, Bio X Cell) Anti-Mouse CD8α antibody (2.43, Bio X Cell)	400µg anti-mouse CD4 – IP administration – 2x/week 400µg anti-mouse CD8α – IP administration – 2x/week	Consistent – 99% Depletion of neutrophils in peripheral blood (Supplemental 5f, 5g)
B-cell Depletion	Anti-mouse B220/CD45R antibody (RA3.31, Bio X Cell)	400µg anti-mouse B220/CD45R – IP administration – 2x/week	Transient – 99% Depletion of B-cells in peripheral blood 4 days after start of depletion. Full reconstitution of B-cells by 3 weeks (Supplemental 5h, 5i)

Supplementary Movie 2.1

Link: https://aiche.onlinelibrary.wiley.com/doi/full/10.1002/btm2.10309

Supplementary Note 2.1

The second order rate constant (k) for Tz-Nb reaction has been previously estimated to be 1.3 - 1.7 $M^{-1}s^{-1}$ at 21°C (room temperature).[1,2] In our system, for high-DOS Tz-HA and Nb-HA the concentration is 0.55mM at the start of the reaction. The reaction rate can be calculated as:

$$rate = k[Nb][Tz] \quad (1)$$

We calculated the rate of reaction to be about 40μM/s from equation 1 and the time to completion to be about 46.3 minutes at 21°C. In our system, the initial temperature is 4°C and therefore the actual time for completion of the reaction would be significantly longer.

As the solution cools and freezes during the crosslinking process, we estimated the freezing time. First, we determined the energy required to freeze 30uL of HA solution starting from 4°C and ending at 0°C using:

$$Q = \frac{\Delta H_i - \Delta H_f}{\rho V} \quad (2)$$

The energy required to freeze 30μL HA solution from 4°C to 0°C is 10.5J[3]. Since the HA solution is very dilute (0.6 wt%), we have approximated the enthalpy of formation and density to that of water.

To calculate the freezing time, we need to estimate the rate of energy extraction from the HA solution. Since the teflon cryomold is pre-cooled to -20^{o}C and rests on a metal shelf in the freezer, we can estimate the rate of freezing using the thermal conductivity of teflon, thickness of teflon (25mm), and conductive heat transfer area (5.75mm) using equation 3. To simplify the analysis, we assume that convective heat loss at air-cryogel interface is negligible.

$$rate\ of\ heat\ transfer\ = \frac{kA\Delta T}{L} \qquad (3)$$

The rate of heat transfer is calculated to be 0.010J/s and therefore the time to reach 0^{o}C is ~16.8 minutes. Since we are ignoring conductive heat loss through the edge of the cryogels and convective heat loss through the top, the calculated time represents an overestimation for the freezing time but is still significantly below that of the time to reaction completion. We have also experimentally verified that a 30uL drop of Tz-HA/Nb-HA solution freezes in about 10 minutes.

References:

1. Vrabel M, Kölle P, Brunner KM, Gattner MJ, López-Carrillo V, de Vivie-Riedle R, Carell T. Norbornenes in inverse electron-demand Diels-Alder reactions. Chemistry. 2013;19(40):13309-12.

2. Devaraj, N. K., Weissleder, R., & Hilderbrand, S. A. (2008). Tetrazine-based cycloadditions: application to pretargeted live cell imaging. Bioconjugate chemistry, 19(12), 2297–2299. https://doi.org/10.1021/bc8004446

3. https://www.engineeringtoolbox.com/saturated-ice-steam-d_970.html

2.6 Methods

2.6.1 General methods and statistics

Sample sizes for animal studies were based on prior work without use of additional statistical estimations. Results were analyzed where indicated using student's t-test and two-way ANOVA with Bonferroni's test using Graphpad Prism software. Mixed-model linear regression was conducted using IBM SPSS statistical package. Alphanumeric coding was used in blinding for pathology samples and cell counting.

2.6.2 Chemicals

Sodium hyaluronate (MW 1.5-2.2 MDa, Pharma Grade 150, lot: 18011K) and sodium alginate (MW ~250 kDa, Pronova UP MVG) were purchased from NovaMatrix. (2-morpholinoethanesulfonic acid (MES), sodium chloride (NaCl), sodium hydroxide (NaOH), *N*-hydroxysuccinimide (NHS), 1-ethyl-3-(3-dimethylaminopropyl)-carbodiimide hydrochloride (EDC), sodium periodate (311448) and ammonia borane (AB) complex (682098) were purchased from Sigma-Aldrich. (4-(1,2,4,5-tetrzain-3-yl)phenyl)methanamine (tetrazine amine) was purchased from Kerafast (FCC659, lot: 2014). 1-bicyclo[2.2.1]hept-5-en-2-ylmethanamine (norbornene amine) was purchased from Matrix Scientific (# 038023, lot: M15S). Cy5-tetrazine amine was purchased from Lumiprobe (lot: 9D2FH). 1kDa molecular weight cutoff (MWCO) mPES membrane was purchased from Spectrum (S02-E001-05-N).

2.6.3 Derivatization of HA

Tetrazine functionalized HA (HA-Tz) or norbornene functionalized HA (HA-Nb) were prepared by reacting tetrazine amine or norbornene amine to HA using EDC/NHS carbodiimide chemistry. Sodium hyaluronate was dissolved in a buffer solution (0.75%

wt/vol, pH ~ 6.5) of 100mM MES buffer. NHS and EDC were added to the mixture to activate the carboxylic acid groups on the HA backbone followed by either tetrazine amine or norbornene amine. HA was assumed to be 1.8 MDa for purposes of conjugation reactions. To synthesize 7% DOS HA-Tz (high-DOS), the molar ratios of HA:EDC:NHS:tetrazine are 1:25000:25000:2500. To synthesize 0.8% DOS HA-Tz (low-DOS), the molar ratios of HA:EDC:NHS:tetrazine are 1:2860:2860:286. To synthesize HA-Nb, the molar ratios of HA:EDC:NHS:norbornene are 1:25000:25000:2500. Each reaction was stirred at room temperature for 24 hours and transferred to a 12,000Da MW cutoff dialysis sack (Sigma Aldrich) and dialyzed in 4L of NaCl solutions of decreasing molarity (0.125M, 0.100M, 0.075M, 0.050M, 0.025M, 0M, 0M, 0M, 0M) for 8 hours per solution. After dialysis, solutions containing HA-Tz or HA-Nb were frozen overnight and lyophilized (Labconco Freezone 4.5) for 48 hours. Cy5 conjugated HA-Nb (Cy5-HA-Nb) was synthesized following a previously described technique with some modifications [80]. 0.8mg of Cy5-Tz was reacted with 100mg of HA-Nb at 0.2 wt/vol in DI water for 24 hours at 37 ^{o}C and purified by dialysis in DI water using a 12,000Da MW cutoff dialysis sack for 48 hours. Dialysis water bath was changed every ~8 hours. The Cy5-HA-Nb solution was then frozen overnight and lyophilized for 48 hours.

2.6.4 Preparation of oxidized alginate

Alginate was oxidized by mixing a 1% wt/vol solution of sodium alginate in DI water with an aqueous solution of 23 mM sodium periodate (Sigma Aldrich) to achieve a 1:586 molar ratio of alginate: periodate. The reaction was stirred in the dark at room temperature overnight. Sodium chloride (1.8 grams/gram of alginate) was added to solution to achieve a 0.3 M solution, followed by purification via tangential flow filtration (TFF) using a mPES

1kDa molecular weight cutoff (MWCO) membrane (Spectrum) and sequential solvent exchanges with 0.15 M – 0.10 M – 0.05 M and 0.0 M sodium chloride in DI water. The resulting solution was treated with ammonia borane (AB) complex (Sigma Aldrich) at 1:4 alginate:AB molar ratio and stirred at room temperature overnight. Sodium chloride (1.8 grams/gram of alginate) was added to solution to achieve a 0.3 M solution, followed by purification via TFF using a 1kDa MWCO mPES membrane and sequential solvent exchanges with 0.15 M – 0.10 M – 0.05 M and 0.0 M sodium chloride in DI water. The resulting solution was lyophilized to dryness.

2.6.5 Derivatization of oxidized alginate

To synthesize tetrazine and norbornene functionalized oxidized alginate (OxAlg-Tz, OxAlg-Nb respectively), oxidized alginate, prepared as described above, was solubilized in 0.1 M MES buffer,0.3 M sodium chloride, pH 6.5 at 1%wt/vol. NHS and EDC were added to the mixture followed by either tetrazine or norbornene. The molar ratio of oxidized alginate:NHS:EDC:tetrazine or norbornene was 1:5000:5000:1000. The reaction is stirred in the dark at room temperature overnight. The resulting solution is centrifuged at 4700 rpm for 15 minutes and filtered through a 0.2-micron filter. The solution is purified via TFF using a mPES 1kDa molecular weight cutoff (MWCO) membrane and sequential solvent exchanges with 0.15 M – 0.10 M – 0.05 M and 0.0 M sodium chloride in DI water. The purified solution is treated with activated charcoal (1 gram / gram of alginate) for 20 minutes at room temperature. The slurry is filtered through 0.2-micron filter and the filtrate is lyophilized to dryness.

2.6.6 Endotoxin Testing

Endotoxin testing of high-DOS HA-Tz and Cy5-HA-Nb were conducted using a commercially available endotoxin testing kit (88282, Thermo Fisher Scientific, lot: VH310729) and following manufacturer's instructions. High-DOS HA-Tz and Cy5-HA-Nb were solubilized at 0.6 wt% in endotoxin free water and samples were tested in technical triplicates. To calculate endotoxin content of a single HA cryogel, the EU/mL concentration for high-DOS HA-Tz and Cy5-HA-Nb were divided by 2 (relative concentrations of HA-Tz and HA-Nb in HA cryogels are 0.3 wt%) and multiplied by 0.03 (30uL of volume per HA cryogel). EU/kg was calculated based on 2 HA cryogels administered into a mouse with an average weight of 20 grams.

2.6.7 Cryogel development

We followed a previously described cryogelation method[80-82]. To form cryogels, aqueous solutions of 0.6% wt/vol HA-Tz and HA-Nb or OxAlg- Tz and OxAlg-Nb were prepared by dissolving lyophilized polymers into deionized water and left on a rocker at room temperature for a minimum of 8 hours to allow for dissolution. The aqueous solutions were then pre-cooled to 4^{o}C before cross-linking to slow reaction kinetics. HA-Tz and HA-Nb or OxAlg- Tz and OxAlg-Nb solutions were mixed at a 1:1 volume ratio, pipetted into 30µL Teflon molds which were pre-cooled to -20 ^{o}C, and quickly transferred to a -20 ^{o}C freezer to allow for overnight cryogelation. Synthesis of Cy5-HA or Cy5-OxAlg cryogels follows the same protocol as above, substituting Cy5-HA-Nb for HA-Nb or Cy5-OxAlg-Nb for OxAlg-Nb.

2.6.8 Pore size analysis of HA cryogels

For scanning electron microscopy (SEM), frozen HA cryogels were lyophilized for 24 hours and in a petri dish. Lyophilized HA cryogels were adhered onto sample stubs using carbon tape and coated with iridium in a sputter coater. Samples were imaged using secondary electron detection on a FEI Quanta 250 field emission SEM in the Nano3 user facility at UC San Diego. Fluorescence images of Cy5-HA cryogels were acquired using a Leica SP8 All experiments were performed at the UC San Diego School of Medicine Microscopy Core. Pore size quantification of SEM images and relative distribution of pore sizes of confocal images was doing using FIJI image processing package [83].

2.6.9 HA cryogel pore-interconnectedness analysis

Cy5-HA cryogels were synthesized with low- and high-DOS HA-Tz and incubated in 1mL of FITC-labeled 10μM diameter melamine resin micro particles (Sigma Aldrich) at 0.29mg/mL concentration on a rocker at room temperature overnight. Fluorescence images of Cy5-HA cryogels with FITC-labeled microparticles were acquired using a Leica SP8 confocal. Interconnectedness of the HA cryogels was determined by generating 3D renderings of confocal z-stacks using FIJI imaging processing package and assessing fluorescence intensity of both the Cy5 and FITC channels with depth starting from the top of the HA cryogel. To determine the effect of injection on pore interconnectedness, HA cryogels were injected through a 16G needle prior to incubation in FITC-labeled microparticle solution. All experiments were performed at the UC San Diego School of Medicine Microscopy Core.

2.6.10 In vitro degradation of Cy5-HA cryogels

Cy5-HA cryogels synthesized with low- and high-DOS HA-Tz and placed into individual 1.5mL microcentrifuge tubes (Thermo Scientific) with 1mL of 100U/mL Hyaluronidase

from sheep testes Type II (HYAL2, H2126, Sigma Aldrich, lot: SLBZ9984) in 1x PBS. Degradation studies were conducted in tissue culture incubators at 37 ^{o}C. Supernatant from samples were collected every 24 – 72 hours by centrifuging the samples at room temperature at 2,000G for 5 minutes and removing 0.9mL of supernatant. Cy5-HA cryogels were resuspended by adding 0.9mL of freshly made 100U/mL HYAL2 in 1x PBS. Fluorescence measurements were conducted using a Nanodrop 2000 Spectrophotometer (Thermo Fisher Scientific) and these values were normalized to sum of the fluorescence values over the course of the experiment. All experiments were performed at UC San Diego.

2.6.11 In vitro degradation of Cy5-OxAlg Cryogels

Cy5-OxAlg cryogels were placed into individual 1.5mL microcentrifuge tube with 1mL of 1x PBS. Degradation studies were conducted in tissue culture incubators at 37^{o}C. Supernatant from samples were collected every 24 – 72 hours by removing visible Cy5-OxAlg cryogel material with tweezers and transferring to new 1.5mL microcentrifuge tube with 1mL of 1x PBS. Fluorescence measurements were conducted using a Nanodrop 2000 Spectrophotometer and these values were normalized to sum of the fluorescence values over the course of the experiment. All experiments were performed at UC San Diego.

2.6.12 In vivo mouse experiments

All animal work was conducted at the Moores Cancer Center vivarium at UC San Diego, except NSG mouse IVIS imaging experiments, which were conducted at the Harvard Biological Research Infrastructure vivarium at Harvard University and approved by the respective Institutional Animal Care and Use Committee (IACUC). All animal experiments

followed the National Institutes of Health guidelines and relevant AALAC-approved procedures. Female C57BL/6J (B6, Jax # 000664) and NOD.Cg-*Prkdc*^{scid} *Il2rg*^{tm1Wjl}/SzJ (NSG, Jax # 005557) mice were 6-8 weeks at the start of the experiments. Male B6.129S-Cybb^{tm1Din} (gp91^{phox-}, Jax # 002365) mice were 6-8 weeks old at the start of experiments. All mice in each experiment were age matched and no randomization was performed. The pre-established criteria for animal omission were failure to inject the desired cell dose in transplanted mice and death due to transplant failure. Health concerns unrelated to the study (e.g. malocclusion) and known mouse-strain specific conditions that affected measurements (e.g. severe dermatitis and skin hyperpigmentation in B6 mice) were criteria for omission.

2.6.13 Immune depletion in mice

Neutrophil depletion in B6 mice was achieved by following the previously established protocol [28, 84]. Briefly, 25μL of anti-mouse Ly6G antibody (1A8, Bio X Cell, lot: 737719A2)) was administered i.p. every day for the first week. Concurrently, 50μL of anti-rat κ immunoglobulin light chain antibody (MAR 18.5, Bio X Cell, lot: 752020J2) was administered every other day starting on the second day of depletion. After one week, the dose of the anti-mouse Ly6G antibody was increased to 50μL. Macrophage depletion in B6 mice was induced by i.p. administration of 100uL of clodronate liposomes (Liposoma, lot: C44J0920) every 3-days. B cell lineage depletion in B6 mice was induced by i.p. administration of 400μg of anti-mouse B220/CD45R antibody (RA3.31/6.1, Bio X Cell, lot: 754420N1) once every 3-days. T cell lineage depletion in B6 mice was induced by i.p. administration of 400μg dose of anti-mouse CD4 antibody (GK1.5, Bio X Cell, lot: 728319M2) and 400μg dose of anti-mouse CD8α antibody (2.43, Bio X Cell,

lot:732020F1) once every 3-days. For all lineage depletion models, mice received intraperitoneal injections of 0.1mL (400µg) of antibodies or 0.1mL of clodronate liposome solution 3 days before subcutaneous HA cryogel or Cy5-HA cryogel injection. Depletion started 3-days prior to Cy5-HA cryogel administration to mice and continued until complete cryogel degradation or until mice were euthanized and cryogels retrieved for analysis. All experiments were performed at the Moores Cancer Center vivarium at UC San Diego.

2.6.14 Transplant models

Irradiations were performed with a Cesium-137 gamma-radiation source irradiator (J.L. Shepherd & Co.). Syngeneic HSCT (B6 recipients) consisted of 1 dose of 1,000 cGy + 1 x 10^5 lineage-depleted bone marrow cells from syngeneic B6 donors. Bone marrow cells for transplantation (from donors) or analysis were harvested by crushing all limbs with a mortar and pestle, diluted in 1x PBS, filtering the tissue homogenate through a 70 µm mesh and preparing a single-cell suspension by passing the cells in the flowthrough once through a 20-gauge needle. Total cellularity was determined by counting cells using a hemacytometer. Bone marrow cells were depleted of immune cells (expressing CD3ε, CD45R/B220, Ter-119, CD11b, or Gr-1) by magnetic selection using a Mouse Hematopoietic Progenitor Cell Enrichment Set (BD Biosciences # 558451, lot: 0114777). To confirm depletion, we incubated cells with a mix of Pacific Blue-conjugated lineage specific antibodies (antibodies to CD3, NK1.1, Gr-1, CD11b, CD19, CD4 and CD8) and with Sca-1 and cKit-specific antibodies for surface staining and quantification of $Lineage^-$ fraction of cells, which were $\geq$ 87% lineage depleted. Subsequently, cells were suspended in 100µL of sterile 1x PBS and administered to anesthetized mice via a single retroorbital

injection. All experiments were performed at the Moores Cancer Animal Facility at UC San Diego Health. All flow cytometry experiments were performed using an Attune® NxT Acoustic Focusing cytometer analyzer (A24858) at UC San Diego.

2.6.15 Subcutaneous cryogel administration

While mice were anesthetized, a subset received a subcutaneous injection of HA cryogel or OxAlg cryogel, which was suspended in 200µL of sterile 1x PBS, into the dorsal flank by means of a 16G needle positioned approximately midway between the hind- and forelimbs. The site of injection was shaved and wiped with a sterile alcohol pad prior to gel injection.

2.6.16 In vivo degradation

In vivo Cy5-HA cryogel degradation was performed with Cy5-HA cryogels synthesized with low- and high-DOS Tz-HA in untreated B6 mice, immune deficient B6 mice, NSG mice, and gp91^{phox-} mice. In vivo Cy5 OxAlg cryogel degradation was performed in non-irradiated, non-transplanted B6 mice and B6 mice post-HSCT. In all cases, cryogels were administered into the dorsal flank of an anesthetized mouse and the fluorescent intensity of the Cy5-HA cryogel was quantified using an IVIS spectrometer (PerkinElmer) at predetermined timepoints and analyzed using LivingImage software (PerkinElmer). At each timepoint, mice were anesthetized and the area around the subcutaneous cryogel was shaved to reduce fluorescence signal attenuation. Fluorescence radiant efficiency, the ratio of fluorescence emission to excitation, was measured longitudinally as a metric to quantify fluorescence from subcutaneous cryogels. These values were normalized to the measured signal on day 3. All experiments were performed at the Moores Cancer Microscopy Core Facility at UC San Diego Health, with the exception of NSG mouse in

vivo degradation experiments, which were performed at the Harvard Biology Research Infrastructure vivarium using an IVIS spectrometer (PerkinElmer).

2.6.17 Flow cytometry analysis

Anti-mouse antibodies to CD45 (30-F11, lot: B280746), CD11b (M1/70, lot: B322056), CD4 (RM4-5, lot: B240051), CD8α (53-6.7, lot: B266721), B220 (RA3-6B2, lot: B298555), Ly6-G/Gr-1 (1A8, lot: B259670), lineage cocktail (17A2/RB6-8C5/RA3-6B2/Ter-119/M1/70, lot: B266946), Ly-6A/E/Sca-1 (D7, lot: B249343), and CD117/cKit (2B8, lot: B272462) were purchased from Biolegend. Anti-mouse F4/80 (BM8, lot: 2229150) and was purchased from eBioscience. All cells were gated based on forward and side scatter characteristics to limit debris, including dead cells. AnnexinV (Biolegend, lot: B300974) stain was used to separate live and dead cells. Antibodies were diluted according to the manufacturer's suggestions. Cells were gated based on fluorescence-minus-one controls, and the frequencies of cells staining positive for each marker were recorded. To quantify T cells, B cells, monocytes, and neutrophils in peripheral blood, blood was first collected from the tail vein of mice into EDTA coated tubes (BD). Samples then underwent lysis of red blood cells and were stained with appropriate antibodies corresponding to cell populations of interest. To quantify infiltrating immune cells within Cy5-HA cryogels, mice were sacrificed, cryogels removed, and HA cryogels crushed against a 70-micron filter screen before antibody staining. Absolute numbers of cells were calculated using flow cytometry frequency. Flow cytometry was analyzed using FlowJo (BD) software. All flow cytometry experiments were performed using a Attune® NxT Acoustic Focusing cytometer analyzer (A24858) at UC San Diego.

2.6.18 Histology

After euthanasia, HA cryogels were explanted and fixed in 4% paraformaldehyde (PFA) for 24 hours. The fixed HA cryogels were then transferred to 70% ethanol solution. Samples were routinely processed and sections (5μm) were stained and digitized using an Aperio AT2 Automated Digital Whole Slide Scanner by the Tissue Technology Shared Resource at the Moores Cancer Center at UC San Diego Health. Digital slides were rendered in QuPath and positive cell detection was used to quantify the total number of mononuclear cells within each image. Quantification of mononuclear cell density was determined for each histological section.

2.6.19 Immunohistochemistry (IHC)

Paraffin embedded HA cryogel sections were baked at 60 ^{o}C for 1 hr. Tissues were then rehydrated through successive washes (3x xylene, 2x 100% ethanol, 2x 95% ethanol, 2x 70% ethanol, di-water). After rehydration, antigen retrieval was conducted using Unmasking solution (Citrate based, pH 6) (Vector Laboratories, H-3300) at 95 ^{o}C for 30 minutes. Staining was performed using Intellipath Automated IHC Stainer (Biocare). A peroxidase block, Bloxall (Vector Laboratories, SP-6000) was performed for 10 minutes, followed by 2x washes in 1x tris-buffered saline with 0.1% Tween 20 (TBST, Sigma Aldrich), and a blocking step using 3% Donkey Serum for 10 minutes. Samples were stained using anti-Ly6G primary antibody (Rabbit, Cell Signaling Technology, 87048S) at 1:100 concentration for 1 hr. Samples were washed twice in TBST and anti-rabbit HRP polymer (Cell IDX, 2HR-100) was added for 30 minutes. Samples were washed twice in TBST and DAB (brown) Chromogen (VWR, 95041-478) was added for 5 minutes. This was followed by 2x washes in di-water, 5-minute incubation with Mayer's Hematoxylin

(Sigma, 51275), 2x washes in TBST, and 1x wash in di-water. Mounting was performed using a xylene-based mountant. IHC was performed by the Tissue Technology Shared Resource at the Moores Cancer Center at UC San Diego Health.

2.6.20 G-CSF encapsulation

To quantify G-CSF release from HA cryogels, recombinant human G-CSF (300-23, Peprotech, lots: 041777 and 041877) was reacted with sulfo-Cy5 NHS ester (13320, Lumiprobe, lot 7FM7C) at a 1:250:25 molar ratio of G-CSF:EDC:sulfo-Cy5 NHS ester in MES buffer to form Cy5 G-CSF. Unreacted EDC and sulfo-Cy5 NHS ester was removed by overnight dialysis on a 10kDa dialysis membrane. 1µg of Cy5 G-CSF was added to 0.6% wt/vol HA-Tz solution before mixing with HA-Nb and cryogelation as described above. To track Cy5-HA cryogel degradation in mice which received G-CSF loaded Cy5-HA cryogels, the same protocol is followed substituting G-CSF for Cy5 G-CSF and Cy5-HA-Nb for HA-Nb.

2.6.21 Neutrophil reconstitution models

Mice were irradiated and administered an autologous HSCT as described above. PEG G-CSF (MBS355608, MyBioSource, lot: R15/2020J) or G-CSF was injected i.p. Cy5-HA cryogel encapsulating G-CSF was injected subcutaneously as described above, 24 hours post-HSCT. Mice were bled at predetermined timepoints and relevant immune subsets were stained for flow cytometry.

2.7 Acknowledgements

Matthew D. Kerr: Conceptualization, methodology, validation, formal analysis, investigation, resources, data curation, writing – original draft, writing – review & editing

and visualization. **David A. McBride:** Methodology, investigation, writing – review and editing. **Wade T. Johnson:** Investigation and writing – review and editing. **Arun K. Chumber:** Investigation and writing – review and editing. **Alexander J. Najibi:** Investigation and writing – review and editing. **Bo Ri Seo.** Investigation and writing – review and editing. **Alexander G. Stafford:** Resources. **David T. Scadden:** Funding acquisition. **David J. Mooney:** Conceptualization, writing – review and editing, and funding acquisition. **Nisarg J. Shah:** Conceptualization, writing - original draft, writing – review and editing, supervision, project administration, funding acquisition. All authors reviewed the manuscript and data, provided input and approved the submission.

The work was supported in part by the American Cancer Society (IRG-15-172-45-IRG), National Multiple Sclerosis Society (PP-1905-34013), the National Institutes of Health (R03DE031009, P30AR073761, and R01DE013349), the Blavatnik Biomedical Accelerator and the Hansjörg Wyss Institute for Biologically Inspired Engineering at Harvard University. M.D.K. and D.A.M. received NIH training grant support through the NCI (T32CA153915) and NIAMS (T32AR064194 and F31AR079921) respectively. The authors acknowledge assistance by the Moores Cancer Center Tissue Technology Shared Resource at UC San Diego Health, the Microscopy Core at UC San Diego School of Medicine, and the Biostatistics Unit of the Clinical and Translational Research Institute at UC San Diego supported by the National Institutes of Health (P30CA23100, P30NS047101 and UL1TR001442 respectively). This work was performed in part at the San Diego Nanotechnology Infrastructure (SDNI) of UCSD, a member of the National Nanotechnology Coordinated Infrastructure (NNCI), which is supported by the National Science Foundation under Grant No. ECCS-1542148. The content is solely the

responsibility of the authors and does not necessarily represent the official views of the National Institutes of Health or the National Science Foundation.

The datasets generated during and/or analyzed during the current study are available from the corresponding authors on reasonable request.

M.D.K., D.J.M. and N.J.S. are named inventors on U.S. Provisional Patent Application No. 63/110,528.

Chapter 2, in full, is a reprint of the material as it appears in Bioengineering & Translational Medicine. 2022, 8(1): e10309, with the following authors Matthew D. Kerr, David A. McBride, Wade T. Johnson, Arun K. Chumber, Alexander J. Najibi, Bo Ri Seo, Alexander G. Stafford, David T. Scadden, David J. Mooney, & Nisarg J. Shah. The dissertation author was the primary investigator and author of this paper.

2.8 References

1. Mócsai, A. Diverse novel functions of neutrophils in immunity, inflammation, and beyond. Journal of Experimental Medicine 210, 1283-1299 (2013).
2. Anderson, J.M., Rodriguez, A. & Chang, D.T. in Seminars in immunology, Vol. 20 86-100 (Elsevier, 2008).
3. Wang, J. et al. Visualizing the function and fate of neutrophils in sterile injury and repair. Science 358, 111-116 (2017).
4. Lakshman, R. & Finn, A. Neutrophil disorders and their management. J Clin Patho 54, 7-19 (2001).
5. Crawford, J., Dale, D.C. & Lyman, G.H. Chemotherapy-induced neutropenia: risks, consequences, and new directions for its management. Cancer 100, 228-237 (2004).

6. Gil, L. et al. Neutropenic enterocolitis after high-dose chemotherapy and autologous stem cell transplantation: incidence, risk factors, and outcome. Transplant Infectious Disease 15, 1-7 (2013).
7. Ley, K. et al. Neutrophils: New insights and open questions. Science immunology 3 (2018).
8. Celebi, H., Akan, H., Akcaglayan, E., Ustun, C. & Arat, M. Febrile neutropenia in allogeneic and autologous peripheral blood stem cell transplantation and conventional chemotherapy for malignancies. Bone marrow transplantation 26, 211-214 (2000).
9. Sadtler, K. et al. The Scaffold Immune Microenvironment: Biomaterial-Mediated Immune Polarization in Traumatic and Nontraumatic Applications<sup/>. Tissue engineering. Part A 23, 1044-1053 (2017).
10. Balletto, E. & Mikulska, M. Bacterial Infections in Hematopoietic Stem Cell Transplant Recipients. Mediterranean journal of hematology and infectious diseases 7, e2015045 (2015).
11. Stoma, I., Karpov, I., Milanovich, N., Uss, A. & Iskrov, I. Risk factors for mortality in patients with bloodstream infections during the pre-engraftment period after hematopoietic stem cell transplantation. Blood research 51, 102-106 (2016).
12. Matsushima, H. et al. Neutrophil differentiation into a unique hybrid population exhibiting dual phenotype and functionality of neutrophils and dendritic cells. Blood 121, 1677-1689 (2013).
13. Weiskopf, K. et al. Myeloid Cell Origins, Differentiation, and Clinical Implications. Microbiology spectrum 4 (2016).

14. Trivedi, M., Martinez, S., Corringham, S., Medley, K. & Ball, E.D. Optimal use of G-CSF administration after hematopoietic SCT. Bone marrow transplantation 43, 895-908 (2009).
15. Mehta, H.M., Malandra, M. & Corey, S.J. G-CSF and GM-CSF in Neutropenia. Journal of immunology (Baltimore, Md. : 1950) 195, 1341-1349 (2015).
16. Bajrami, B. et al. G-CSF maintains controlled neutrophil mobilization during acute inflammation by negatively regulating CXCR2 signaling. The Journal of experimental medicine 213, 1999-2018 (2016).
17. Pinto, L. et al. Comparison of pegfilgrastim with filgrastim on febrile neutropenia, grade IV neutropenia and bone pain: a meta-analysis of randomized controlled trials. Current medical research and opinion 23, 2283-2295 (2007).
18. Singh, A.D. et al. Granulocyte Colony-Stimulating Factor Use after Autologous Peripheral Blood Stem Cell Transplantation: Comparison of Two Practices. Biology of blood and marrow transplantation : journal of the American Society for Blood and Marrow Transplantation 24, 288-293 (2018).
19. Ashrafi, F. & Salmasi, M. Comparison of the effects of pegylated granulocyte-colony stimulating factor and granulocyte-colony stimulating factor on cytopenia induced by dose-dense chemotherapy in breast cancer patients. Journal of research in medical sciences : the official journal of Isfahan University of Medical Sciences 23, 73 (2018).
20. Molineux, G. The design and development of pegfilgrastim (PEG-rmetHuG-CSF, Neulasta). Current pharmaceutical design 10, 1235-1244 (2004).

21. Elsadek, N.E. et al. Pegfilgrastim (PEG-G-CSF) induces anti-PEG IgM in a dose dependent manner and causes the accelerated blood clearance (ABC) phenomenon upon repeated administration in mice. European Journal of Pharmaceutics and Biopharmaceutics 152, 56-62 (2020).
22. Girard, N. et al. Human monocytes synthesize hyaluronidase. British Journal of Haematology 119, 199-203 (2002).
23. Soltes, L. et al. Degradative action of reactive oxygen species on hyaluronan. Biomacromolecules 7, 659-668 (2006).
24. Jiang, D., Liang, J. & Noble, P.W. Hyaluronan as an immune regulator in human diseases. Physiological reviews 91, 221-264 (2011).
25. Ito, M. et al. NOD/SCID/gamma(c)(null) mouse: an excellent recipient mouse model for engraftment of human cells. Blood 100, 3175-3182 (2002).
26. Malyala, P. & Singh, M. Endotoxin limits in formulations for preclinical research. Journal of pharmaceutical sciences 97, 2041-2044 (2008).
27. Burdick, J.A., Chung, C., Jia, X., Randolph, M.A. & Langer, R. Controlled degradation and mechanical behavior of photopolymerized hyaluronic acid networks. Biomacromolecules 6, 386-391 (2005).
28. Boivin, G. et al. Durable and controlled depletion of neutrophils in mice. Nature Communications 11, 2762 (2020).
29. Pollock, J.D. et al. Mouse model of X-linked chronic granulomatous disease, an inherited defect in phagocyte superoxide production. Nature genetics 9, 202-209 (1995).

30. Banerjee, E.R. & Henderson, W.R., Jr. Role of T cells in a gp91phox knockout murine model of acute allergic asthma. Allergy, asthma, and clinical immunology : official journal of the Canadian Society of Allergy and Clinical Immunology 9, 6 (2013).
31. Bouhadir, K.H. et al. Degradation of Partially Oxidized Alginate and Its Potential Application for Tissue Engineering. Biotechnology Progress 17, 945-950 (2001).
32. Gao, C., Liu, M., Chen, J. & Zhang, X. Preparation and controlled degradation of oxidized sodium alginate hydrogel. Polymer Degradation and Stability 94, 1405-1410 (2009).
33. Jagasia, M.H. et al. Pegfilgrastim after high-dose chemotherapy and autologous peripheral blood stem cell transplant: phase II study. Bone Marrow Transplantation 35, 1165-1169 (2005).
34. Martino, M. et al. Pegfilgrastim compared with filgrastim after high-dose melphalan and autologous hematopoietic peripheral blood stem cell transplantation in multiple myeloma patients. European journal of haematology 77, 410-415 (2006).
35. Barr, S., Hill, E.W. & Bayat, A. Functional biocompatibility testing of silicone breast implants and a novel classification system based on surface roughness. Journal of the Mechanical Behavior of Biomedical Materials 75, 75-81 (2017).
36. Carnicer-Lombarte, A., Chen, S.-T., Malliaras, G.G. & Barone, D.G. Foreign Body Reaction to Implanted Biomaterials and Its Impact in Nerve Neuroprosthetics. Frontiers in Bioengineering and Biotechnology 9 (2021).

37. Whitaker, R., Hernaez-Estrada, B., Hernandez, R.M., Santos-Vizcaino, E. & Spiller, K.L. Immunomodulatory Biomaterials for Tissue Repair. Chemical Reviews (2021).

38. Sutherland, K., Mahoney, J.R., Coury, A.J. & Eaton, J.W. Degradation of biomaterials by phagocyte-derived oxidants. The Journal of clinical investigation 92, 2360-2367 (1993).

39. Ye, Q., Harmsen, M.C., van Luyn, M.J. & Bank, R.A. The relationship between collagen scaffold cross-linking agents and neutrophils in the foreign body reaction. Biomaterials 31, 9192-9201 (2010).

40. Labow, R.S., Meek, E. & Santerre, J.P. Neutrophil-mediated biodegradation of medical implant materials. Journal of cellular physiology 186, 95-103 (2001).

41. Shah, N.J. et al. A biomaterial-based vaccine eliciting durable tumour-specific responses against acute myeloid leukaemia. Nature Biomedical Engineering 4, 40-51 (2020).

42. Verbeke, C.S. et al. Multicomponent Injectable Hydrogels for Antigen-Specific Tolerogenic Immune Modulation. Adv Healthc Mater 6, 10.1002/adhm.201600773 (2017).

43. Frantz, C., Stewart, K.M. & Weaver, V.M. The extracellular matrix at a glance. Journal of Cell Science 123, 4195-4200 (2010).

44. Kaderli, S. et al. A novel biocompatible hyaluronic acid-chitosan hybrid hydrogel for osteoarthrosis therapy. International journal of pharmaceutics 483, 158-168 (2015).

45. Kaderli, S. et al. Efficacy study of two novel hyaluronic acid-based formulations for viscosupplementation therapy in an early osteoarthrosic rabbit model. European journal of pharmaceutics and biopharmaceutics : official journal of Arbeitsgemeinschaft fur Pharmazeutische Verfahrenstechnik e.V 96, 388-395 (2015).
46. Buffa, R. et al. Conjugates of modified hyaluronic acid with amino compounds for biomedical applications. Carbohydrate polymers 189, 273-279 (2018).
47. Ma, X. et al. Injectable hydrogels based on the hyaluronic acid and poly (gamma-glutamic acid) for controlled protein delivery. Carbohydrate polymers 179, 100-109 (2018).
48. Purcell, B.P. et al. Injectable and bioresponsive hydrogels for on-demand matrix metalloproteinase inhibition. Nature materials 13, 653-661 (2014).
49. Barker, I.A. et al. Tetrazine-norbornene click reactions to functionalize degradable polymers derived from lactide. Macromolecular rapid communications 32, 1362-1366 (2011).
50. Hansell, C.F. et al. Additive-free clicking for polymer functionalization and coupling by tetrazine-norbornene chemistry. Journal of the American Chemical Society 133, 13828-13831 (2011).
51. Kennedy, S. et al. Rapid and extensive collapse from electrically responsive macroporous hydrogels. Advanced healthcare materials 3, 500-507 (2014).
52. Koshy, S.T., Zhang, D.K.Y., Grolman, J.M., Stafford, A.G. & Mooney, D.J. Injectable nanocomposite cryogels for versatile protein drug delivery. Acta Biomater 65, 36-43 (2018).

53. Qin, X.-H. et al. Enzymatic synthesis of hyaluronic acid vinyl esters for two-photon microfabrication of biocompatible and biodegradable hydrogel constructs. Polym. Chem. 5, 6523-6533 (2014).

54. Chen, F. et al. Self-crosslinking and injectable hyaluronic acid/RGD-functionalized pectin hydrogel for cartilage tissue engineering. Carbohydrate polymers 166, 31-44 (2017).

55. Tavsanli, B. & Okay, O. Mechanically strong hyaluronic acid hydrogels with an interpenetrating network structure. European Polymer Journal 94, 185-195 (2017).

56. Pedron, S. et al. Patterning Three-Dimensional Hydrogel Microenvironments Using Hyperbranched Polyglycerols for Independent Control of Mesh Size and Stiffness. Biomacromolecules 18, 1393-1400 (2017).

57. Šečkutė, J., Yang, J. & Devaraj, N.K. Rapid oligonucleotide-templated fluorogenic tetrazine ligations. Nucleic Acids Research 41, e148-e148 (2013).

58. Johann, K. et al. Tetrazine- and trans-cyclooctene-functionalised polypept(o)ides for fast bioorthogonal tetrazine ligation. Polymer Chemistry 11, 4396-4407 (2020).

59. Yamaguchi, Y., Yamamoto, H., Tobisawa, Y. & Irie, F. TMEM2: A missing link in hyaluronan catabolism identified? Matrix Biology 78-79, 139-146 (2019).

60. Greenwald, R.A. & Moak, S.A. Degradation of hyaluronic acid by polymorphonuclear leukocytes. Inflammation 10, 15-30 (1986).

61. Stern, R., Kogan, G., Jedrzejas, M.J. & Šoltés, L. The many ways to cleave hyaluronan. Biotechnology Advances 25, 537-557 (2007).

62. Greenwald, R.A. & Moy, W.W. Effect of oxygen-derived free radicals on hyaluronic acid. Arthritis & Rheumatism: Official Journal of the American College of Rheumatology 23, 455-463 (1980).

63. McNeil, J., Wiebkin, O., Betts, W. & Cleland, L. Depolymerisation products of hyaluronic acid after exposure to oxygen-derived free radicals. Annals of the Rheumatic Diseases 44, 780-789 (1985).

64. Šoltés, L. et al. Degradative action of reactive oxygen species on hyaluronan. Biomacromolecules 7, 659-668 (2006).

65. Duan, J. & Kasper, D.L. Oxidative depolymerization of polysaccharides by reactive oxygen/nitrogen species. Glycobiology 21, 401-409 (2011).

66. Doloff, J.C. et al. Colony stimulating factor-1 receptor is a central component of the foreign body response to biomaterial implants in rodents and non-human primates. Nature materials 16, 671-680 (2017).

67. Shultz, L.D. et al. Multiple defects in innate and adaptive immunologic function in NOD/LtSz-scid mice. Journal of immunology (Baltimore, Md. : 1950) 154, 180-191 (1995).

68. Shultz, L.D. et al. Human lymphoid and myeloid cell development in NOD/LtSz-scid IL2R gamma null mice engrafted with mobilized human hemopoietic stem cells. Journal of immunology (Baltimore, Md. : 1950) 174, 6477-6489 (2005).

69. Foreman, O., Kavirayani, A.M., Griffey, S.M., Reader, R. & Shultz, L.D. Opportunistic bacterial infections in breeding colonies of the NSG mouse strain. Veterinary pathology 48, 495-499 (2011).

70. Patton, J.B. et al. Methylprednisolone acetate induces, and Δ7-dafachronic acid suppresses, Strongyloides stercoralis hyperinfection in NSG mice. Proceedings of the National Academy of Sciences of the United States of America 115, 204-209 (2018).

71. Pavlů, J. et al. Analysis of hematopoietic recovery after autologous transplantation as method of quality control for long-term progenitor cell cryopreservation. Bone Marrow Transplant 52, 1599-1601 (2017).

72. Ramaprasad, C., Pouch, S. & Pitrak, D.L. Neutrophil function after bone marrow and hematopoietic stem cell transplant. Leukemia & Lymphoma 51, 756-767 (2010).

73. Grainger, D.W. All charged up about implanted biomaterials. Nature biotechnology 31, 507-509 (2013).

74. Freedman, B.R. et al. Degadable and Removable Tough Adhesive Hydrogels. Advanced Materials 33, 2008553 (2021).

75. Zamboni, W.C. Pharmacokinetics of pegfilgrastim. Pharmacotherapy 23, 9S-14S (2003).

76. Zhang, P., Sun, F., Liu, S. & Jiang, S. Anti-PEG antibodies in the clinic: Current issues and beyond PEGylation. Journal of Controlled Release 244, 184-193 (2016).

77. McSweeney, M.D. et al. A minimal physiologically based pharmacokinetic model that predicts anti-PEG IgG-mediated clearance of PEGylated drugs in human and mouse. Journal of Controlled Release 284, 171-178 (2018).

78. Ishida, T., Wang, X., Shimizu, T., Nawata, K. & Kiwada, H. PEGylated liposomes elicit an anti-PEG IgM response in a T cell-independent manner. Journal of Controlled Release 122, 349-355 (2007).

79. Yang, Q. et al. Analysis of Pre-existing IgG and IgM Antibodies against Polyethylene Glycol (PEG) in the General Population. Anal Chem 88, 11804-11812 (2016).

80. Koshy, S.T. et al. Click-Crosslinked Injectable Gelatin Hydrogels. Advanced healthcare materials 5, 541-547 (2016).

81. Shah, N.J. et al. An injectable bone marrow-like scaffold enhances T cell immunity after hematopoietic stem cell transplantation. Nat Biotechnol 37, 293-302 (2019).

82. Desai, R.M., Koshy, S.T., Hilderbrand, S.A., Mooney, D.J. & Joshi, N.S. Versatile click alginate hydrogels crosslinked via tetrazine-norbornene chemistry. Biomaterials 50, 30-37 (2015).

83. Schindelin, J. et al. Fiji: an open-source platform for biological-image analysis. Nature Methods 9, 676-682 (2012).

84. Stackowicz, J., Jönsson, F. & Reber, L.L. Mouse models and tools for the in vivo study of neutrophils. Frontiers in immunology 10, 3130 (2020).

CHAPTER 3

COMBINING THERAPEUTIC VACCINES WITH CHEMO- AND IMMUNOTHERAPIES IN THE TREATMENT OF CANCER

3.0 Abstract

Breakthroughs in cancer immunotherapy have spurred interest in the development of vaccines to mediate prophylactic protection and therapeutic efficacy against primary tumors or to prevent relapse. However, immunosuppressive mechanisms employed by cancer cells to generate effective resistance has hampered clinical translation of therapeutic cancer vaccines. To enhance vaccine efficacy, the immunomodulatory properties of cytoreductive therapies such as chemotherapy and radiation could amplify a cancer-specific immune response. In pre-clinical and clinical applications, key considerations have been identified in the application of combination therapies. Along with checkpoint inhibitors, the development of combination cancer therapies has been a key focus area to enhance a durable anti-tumor immune response.

In this review, we discuss therapeutic cancer vaccines that harness whole cells and antigen targeted vaccines. First, recent advancements in both autologous and allogenic whole cell vaccines and combinations with checkpoint blockade and chemotherapy are reviewed. Next, tumor antigen targeted vaccines using peptide-based vaccines and DNA-vaccines are discussed. Finally, combination therapies using antigen targeted vaccines are reviewed. These sections discuss both pre-clinical research and clinical trials that test combination chemo- and immunotherapies for multiple types of cancers.

A deeper understanding of the immunostimulatory properties of cytoreductive therapies has supported their utility in combination therapies involving cancer vaccines as a potential strategy to induce a durable anti-tumor immune response for multiple types of

cancers. Based on current evidence, combination therapies may have synergies which depend on the identity of the cytotoxic agent, vaccine target, dosing schedule, and cancer type. Together, these observations suggest that combining cancer vaccines with immunomodulatory cytoreductive therapy, including checkpoint blockade and chemotherapy, is a promising strategy for cancer therapy.

3.1 Introduction

Harnessing the immune system for cancer therapy has long been the goal in oncology and is now being realized in clinical practice with cancer immunotherapy [1]. Recent clinical successes have transformed the treatment of aggressive and difficult-to-treat cancers, such as melanoma and lymphoma [2]. Most notable has been the ability of the checkpoint inhibitors to achieve a significant increase in survival for patients with metastatic cancer, for which conventional therapies have failed [3]. In the context of advances towards understanding how tolerance, immunity and immunosuppression regulate antitumor immune responses, alongside the advent of targeted therapies, these successes suggest that active immunotherapy represents a path to obtain a robust and long-lasting response in cancer patients [4].

The discovery of $CD8^+$ and $CD4^+$ T cells specific for cancer-testis or differentiation antigens expressed in patient tumor samples was the harbinger of systematic efforts to characterize tumor-specific or tumor-associated antigens to broaden the effectiveness of immunotherapies using cancer vaccines [5-7]. These efforts focused on actively helping educate the immune system to identify and eliminate cancer cells. Histopathological evaluations of tumor sections have indicated a strong positive association between patient survival, the presence of intratumoral T cells and production of the cytotoxic

molecule interferon-γ (IFN-γ) [8-10]. Vaccination might reasonably be expected to amplify the frequency and strength of these pre-existing responses or perhaps induce de novo reactions. Similar to conventional vaccines for preventing infectious disease, some cancer vaccines have been developed as effective prophylactic (or preventative) agents. This strategy has been deployed with considerable success in the clinic for the prevention of cancers of viral origin, such as hepatitis B virus and human papillomavirus (HPV), where the etiological agent is known, and is now part of the recommended vaccination schedule in children and young adults [11-13].

In contrast, the development of therapeutic vaccines as a monoagent to treat existing disease has proved elusive. Unlike prophylactic cancer vaccines, which confer protection against a known agent, therapeutic vaccines seek to activate an immune response against tumor antigens expressed selectively or exclusively by cancer cells [14]. In designing therapeutic cancer vaccines, the greatest difficulty has been in identifying the combinations of tumor antigens that might be incorporated in a vaccine formulation as expression on cancer cells alone may be inadequate for predicting the ability of a vaccine to generate a protective T cell response [15]. Even when an antigen is identified, it may not be sufficiently immunogenic or uniformly expressed on the tumor to generate a potent and durable immune response [16]. Beyond expression of checkpoint molecules and the mutational burden in cells comprising the tumor, the determinants of an immune response are not well understood [17]. Additionally, the optimal adjuvant that can be used safely and effectively in a cancer vaccine formulation in humans is not yet clear [18]. The desired adjuvant (or adjuvant combination) will be one capable of triggering the maturation of dendritic cells to a state where they can facilitate the generation of tumor-reactive,

cytotoxic T cells [19]. Finally, although it is likely that formulations for human immunization will eventually be optimized, the effectiveness of a tumor-specific T cell may still be limited by the immunosuppression mechanisms deployed by tumors to escape immune cells [20].

Despite the current limitations, conferring immunity against cancer relapse in patients that are in remission can be lifesaving. Therefore, oncologists are employing the strategy of using two or more therapeutic agents to target multiple cancer cell survival pathways, which has been successfully employed as a standard treatment regimen for multiple types of cancers for decades [21]. For example, in advanced non-small cell lung cancer (NSCLC) patients, 42% of patients with programmed death ligand 1 (PD-L1) expressing tumors fail to respond to anti PD-L1, Pembrolizumab [22,23]. However, checkpoint inhibitor in combination with chemotherapy is associated with significantly longer overall survival and progression-free survival as compared to chemotherapy or PD-1 inhibition alone in NSCLC patients [24]. Similarly, in a recent phase III clinical trial (NCT00861614), patients with castration-resistant prostate cancer that had metastasized to the bone marrow after unsuccessful docetaxel treatment, received a combination administration of a single dose of bone directed radiotherapy with anti-cytotoxic T-lymphocyte-associated protein 4 (CTLA-4), Ipilimumab, or placebo every 3 weeks for up to 4 doses [25]. Patients that were co-administered Ipilimumab exhibited a survival benefit as compared to the placebo arm [26]. Furthermore, the effect of cytotoxic chemotherapy and radiation on the cells of the immune system or in modifying the tumor microenvironment to enhance the immune clearance of tumor cells is only now being characterized [27]. Although conventional wisdom might suggest that non-specific cytotoxic chemotherapy might have

deleterious effect on immune mechanisms, such effects may be more nuanced than previously believed and strongly drug-, dose- and/or schedule-dependent [28,29]. The use of combinations of these therapies, in a scientifically guided manner has proved to broaden the anti-tumor response.

To stimulate a durable immune response, the combination of therapeutic cancer vaccines with traditional cancer treatments including radiation and chemotherapy, or targeted immunotherapies is a promising strategy. Towards the goal of enhancing immune responses as potentially curative therapies, a number of cancer vaccine platforms including irradiated whole cancer-cell vaccines, peptide-based vaccines, and virus-vector vaccines, in combination with immunotherapies, are in various phases of clinical and pre-clinical development. Combination strategies with radiation and chemotherapy have been demonstrated to induce tumor cell death and enhance breadth of tumor-specific T cell response and those with immune checkpoint blockade act to accentuate the vaccine mediated cytotoxic T cell response. As the same agent may prove inhibitory, benign or even stimulatory depending on the stage of immune response being targeted and the dose/schedule being used, great care must be exercised when designing strategies and suboptimal dosing schedules. In this review, we examine existing cancer vaccine approaches and highlight the enhanced therapeutic potential of combination cancer vaccine strategies. We first discuss existing cancer vaccine approaches including those that failed to show efficacy in clinical trials. We then discuss various combination approaches involving both pre-clinical cancer vaccine platforms and existing vaccines platforms. Lastly, we conclude with some thoughts on the future directions for both cancer vaccines as monotherapies and cancer vaccine combinations.

3.2 Engineered cell-based combination cancer vaccines

Dendritic cells (DC) are specialized immune cells that play a vital role in promoting an antigen-specific immune response [30-33]. Cancer vaccines that harness DCs have been developed to initiate and shape the tumor-specific immune response and/or boost existing spontaneous antitumor T cell responses. The common strategy for cancer vaccination is to harness the DC function of priming naïve T cells and boost a memory T cell response against tumor associated antigens (TAAs) that are expressed by cancer cells. While there are a variety of different DC vaccine formulations, common elements include – (i) a source of TAAs such as tumor cell lysate or irradiated tumor cells and (ii) a pro-inflammatory chemoattractant, such as granulocyte-macrophage colony stimulating factor (GM-CSF), to recruit and activate DCs.

3.2.1 Autologous DC vaccines

Autologous DC vaccines, derived from patient-specific immune cells, are currently the only type of FDA approved cell-based cancer vaccine. An example of this approach is Provenge, which is approved for the treatment of castration-resistant metastatic prostate cancer (mCRPC) [34]. It is a patient-specific cell therapy in which the patient's peripheral blood mononuclear cells (PBMCs) are cultured with a recombinant fusion protein comprised of prostatic acid phosphatase (PAP) and GM-CSF, which induces dendritic cell (DC) differentiation and presentation of PAP-derived epitopes. These PAP-epitope derived DCs are administered to patients and induce a PAP-specific cytotoxic T cell response [34-36]. Using autologous DCs mitigates concerns of off-target immune responses and reduces the risk of the development of autoimmune-like disorders, which is observed with PD-1/PD-L1 or CTLA-4 checkpoint blockade therapy [37,38]. While this

approach has been shown to improve overall survival as compared to chemotherapy alone, the therapy has limited scalability, since PBMCs must first be isolated from the patient and differentiated into DCs in vitro.

For hematological malignancies, such as acute myeloid leukemia (AML), AML-DCs have the advantage of expressing the full spectrum of antigens [39]. In this approach, hybridomas of AML cells and autologous patient derived DCs have been developed as a potential cell-based cancer vaccine. Notably, among 17 patients vaccinated in complete remission after chemotherapy, 12 (71%) remain in remission at a median follow-up of 57 months. Vaccination was associated with expansion of TAA-specific T cells that lasted more than 6 months [40]. The multicenter study testing this approach is ongoing (NCT01096602) and is estimated to be completed in 2024.

Tumor biopsies are often used to assess the histopathology of the tumor. In addition to characterizing the cytological composition of the tumor, such biopsies may also be used as a source for collecting tumor cells for a cell-based vaccine. The subsequent formulation may be deployed via an injection or implantation [41-43]. One of the major benefits of this approach is that it eschews the need for defined TAAs and could promote a cytotoxic T cell response against multiple TAAs. To manufacture autologous DC vaccines at scale, Ali et al. developed a macroporous poly(lactic-co-glycolic acid) (PLG) scaffold, designed to mediate sustained release of GM-CSF to recruit DCs [44]. Cytosine-guanosine oligonucleotide (CpG-ODN) was incorporated onto the PLG matrix to enhance the fraction of plasmacytoid DCs (pDCs) and promoted local production of tumor necrosis factor α (TNF- α) nd IFN-γ. Tumor cell lysates from freeze-thawing murine B16 melanoma cells were loaded into these scaffolds and resulted in systemic cytotoxic T cell response

against melanoma antigens. This scaffold was able to mediate prophylactic protection against B16 melanoma if administered before B16 melanoma inoculation and provide therapeutic protection against B16 melanoma if administered after inoculation [45]. This platform, termed WDVAX, in now in phase I clinical trials (NCT01753089) for metastatic melanoma.

3.2.2 Allogeneic DC vaccines

Allogenic DC vaccines are an alternative approach to autologous vaccines. The main advantage of this approach is that it precludes the need for isolation and transformation of PBMCs into DCs prior to each administration, allowing for less patient-to-patient variability and enhanced scalability. However, they differ from autologous vaccines in that they do not necessarily contain patient specific TAAs. Thus, even if they can induce an immune response, they may not be able to mediate effective tumor lysis. Commonly used allogenic cells are established cancer cell lines known to express specific TAAs. These allogenic cells are generally transfected to express chemoattractant molecules, such as GM-CSF, prior to administration. The first GM-CSF transfected allogenic pancreatic cancer vaccine, termed GVAX was studied in a 2001 phase I clinical trial. In this dose escalation study, patients with pancreatic cancer were administered irradiated GM-CSF expressing pancreatic cancer cell doses ranging from 1 x 107 to 5 x 108 cells. The highest dose was determined to increase eosinophil and macrophage infiltration into tumors and did not cause any significant adverse effects [46]. As a result of this successful phase I clinical trial, a phase II clinical trial was initiated in which patients with pancreatic cancer received 5 x 108 irradiated GM-CSF secreting allogenic pancreatic cancer cells administered to 3 different lymph node regions. Patients were administered 5 doses over

the course of a year. The overall survival (OS) of patients administered the allogeneic cancer vaccine was 15 to 20 months which is comparable to standard tumor resection. Further, it was found that the vaccine lead to increased induction and maintenance of mesothelin specific T cells which was correlated with longer disease-free survival [47]. However, despite promising phase II clinical data, two phase III clinical trials (Identifiers: NCT00089856, NCT00133224) did not demonstrate therapeutic efficacy and were halted early.

Cancer vaccines against hematological cancers are an attractive therapeutic option, especially for older patients who have fewer treatment options available and are at a higher risk of treatment-related mortality from allogenic hematopoietic stem cell transplantation. For the treatment of acute myeloid leukemia (AML), an allogeneic DC cancer vaccine, DCP-001, was developed by differentiating CD34+ acute myeloid leukemia (AML) cells into DCs. These AML-derived DCs are morphologically and phenotypically identical to myeloid derived-DCs and induced a strong antigen-specific immune response against AML-associated antigens [48]. A phase I clinical trial (NCT01373515) initiated to determine the safety profile of this vaccine when administered intradermally to AML patients within 2 months after having achieved complete remission or patients who have stable disease for at least two months. Patients received 4 bi-weekly vaccinations of DCP-001 cells and T cell reactivity to AML-related antigens WT-1, PRAME, NY-ESO-1, and MAGE-A3 were accessed by IFNγ ELISpot analysis. WT-1 and PRAME are both expressed by DCP-001, and NY-ESO-1 and MAGE-A3 were included to access epitope spreading. Four of eight patients showed DCP-001 induced or enhanced T cell response to at least one of the AML-associated antigens. Further,

antibody responses against blast antigens were evaluated in ten patients, five of whom showed vaccination-induced humoral responses. Overall, patients whose immune-monitoring data demonstrated positive response to the vaccine showed statistically significant improvement in survival over patients who did not respond favorably . As a result of these promising phase I clinical trial results, a phase II clinical trial (NCT03697707) was initiated in 2018.

3.2.3 Combination DC cancer vaccines and approved chemo/immune therapies

Promoting tumor-specific immunity with a vaccine and subsequent amplification of tumor-specific T cells with checkpoint blockade therapy is an attractive hypothesis. The effectiveness of such an approach has been tested using clinically approved PD-1/PD-L1 and CTLA4 blockade using Pembrolizumab or Ipilimumab respectively with cell-based vaccines in preclinical mouse studies and early stage clinical trials [50-53]. In pre-clinical studies, anti-CTLA-4 checkpoint therapy in combination with cancer vaccines (e.g. GVAX) demonstrated synergistic reduction in tumor size and increase in the antitumor immune response in a mouse model of melanoma and prostate cancer. The timing of the combination of anti-CTLA-4/GVAX vaccine has been identified as an important parameter in cancer vaccines. For example, in the prostate cancer model Pro-TRAMP, it has been demonstrated that anti-CTLA-4 mAbs should be administered after vaccination for an additive effect. The effect of timing on treatment efficacy is likely due to higher anti CTLA-4 mAb concentrations in sites of high CTLA-4 expression, such as the gut, since the expression of CTLA-4 on TAA-specific T cells is not upregulated until after vaccination. Therefore, if anti CTLA-4 is administered before or concurrent to vaccination, the anti CTLA-4 mAbs may be unavailable to bind to TAA-specific T cells. Furthermore, the

addition of low-dose cyclophosphamide depletes immune cells, including regulatory T cells (Tregs), and thereby augments the anti-tumor efficacy of GVAX + anti-CTLA-4 combination therapy [51]. In the CT26 murine model of colorectal cancer, dual PD-1 and CTLA-4 checkpoint blockade in combination with GVAX lead to tumor rejection of 100% of mice. This same combination leads to rejection of ID8-VEGF ovarian carcinoma in 75% of mice [52]. Results from mouse studies suggests that anti-CTLA-4 and anti-PD-1 mAbs increase the frequency of activated T cells and the effector T cell/Treg ratio in vaccinated tumors. While studies have focused on the scheduling of anti-CTLA-4 mAbs with vaccination, this variable has been less studied for the combination of anti-PD-1 mAbs and vaccine [54]. The pre-clinical studies with combination checkpoint blockade and GVAX supported clinical trials for patients with metastatic pancreatic cancer (NCT01417000, NCT02243371, NCT02004262) with several that are still ongoing (NCT03161379, NCT03190265, NCT03153410, NCT03006302, NCT02648282, NCT02451982) in which GVAX was combined with cyclophosphamide and/or nivolumab seem promising.

There are also a number of clinical trials in which Provenge is used in combination with cytoreductive therapies including chemotherapy, radiation, immune checkpoint blockade and secondary hormone therapy to better treat mCRPC (NCT00779402, NCT02793765, NCT01807065). Cytoreductive strategies provide a transient decrease in tumor size whereas the Provenge cancer vaccine decreases tumor growth rate. The combination of these approaches could allow for better therapeutic outcomes than a monotherapy. However, many cytoreductive therapies impair immune cell number and function.

Therefore the timing and dose of combination therapies will be an important factor to consider when designing clinical studies [55].

3.3 Cancer-antigen specific subunit cancer vaccines

While whole-cancer cell vaccines are promising, their manufacturing process is labor-intensive and has limited scalability. For example, Provenge is administered intravenously in a three-dose schedule at two-week intervals. Each dose requires leukapheresis three days prior to administration to allow time to differentiate peripheral blood monocytes into DCs. This manufacturing process is not only time consuming and expensive, but also operationally prohibitive in many clinical settings, especially in low-resource settings. As an alternative, peptide and DNA-based cancer vaccines are a potentially cheaper, and more accessible treatment option than whole cell-based vaccines. These vaccines operate in a manner similar to cell-based cancer vaccines, that is, by recruiting DCs and facilitating the expansion of cytotoxic T cells against TAAs. In contrast to whole cell-based vaccines, antigen targeted cancer vaccines are defined and might be manufactured at scale for off-the-shelf use, without the need for cell collection from the patient. However, antigen targeted cancer vaccines require that patient tumors express specific TAAs, which in most types of cancers limits their utility to a subset of patients. Further, the initial cytotoxic T cell response from an antigen targeted vaccine is more restricted than that from whole cell-lysate. Most TAA targets for antigen-targeted cancer vaccines can be grouped into the categories: oncofetal mutations, germline/cancer testis mutations, and lineage differentiation antigens [56].

3.3.1 Oncofetal mutations

Oncofetal antigens are primarily expressed during fetal development but may be mutated and/or over-expressed by cancer cells and is associated with head-and-neck [57], hepatocellular [58], colorectal [59], squamous esophageal [60], and breast carcinoma [61]. Oncofetal TAA targets for vaccine development include carcinoembryonic antigen (CEA), insulin-like growth factor II mRNA-binding protein 3 (IMP-3) [62] and alpha-fetoprotein (AFP) [63]. In a recent pre-clinical study, Hirayama et al. generated IMP3 derived long peptides (IMP-3-LPs) capable of eliciting both TAA specific effector and helper T cells. IMP-3-LPs-specific Th-cells responded to autologous DCs loaded with the recombinant IMP-3 proteins in vitro, suggesting that these IMP-3-LPs can be successfully processed by DCs. Co-culturing IMP-3 specific Th-cells with IMP-3 effector T cells on autologous DCs pulsed with both short peptides derived from IMP-3 and IMP-3-LPs augmented the expansion of IMP-3 effector T cells. Further, IMP-3-LPs were able to induce IMP-3 specific Th-cells from PBMCs isolated from head-and-neck cancer patients [62]. Together, these results highlight the potential for IMP-3 derived peptide-based cancer vaccines in the treatment of head-and-neck cancer. In a separate study, Hensel et al. developed a recombinant adeno-associated virus vector encoding CEA (rAAV-CEA) to mediate prophylactic protection against CEA syngeneic MC38-CEA colon adenocarcinoma model. The rAAV-CEA was administered intramuscularly, followed by multiple administrations of GM-CSF encoding plasmid to the same intramuscular site. Subsequent MC38-CEA tumor challenge in mice resulted in tumor free survival. Notably, tumor challenge in mice with MC38 cells which did not express CEA did not result in enhancement in survival, indicating CEA specific immunity [64].

3.3.2 Germline/cancer testis mutations

Similar to oncofetal mutations, germline/cancer testis mutations may be upregulated by cancer cells and is generally restricted to immune privileged germline cells. Common therapeutic vaccine target mutations include Wilms tumor 1 (WT1) protein, melanoma-associated antigen (MAGE) superfamily, and cancer/testis antigen 1 (NY-ESO-1). A National Cancer Institute consensus study on prioritization of cancer antigens ranked the WT1 protein as the top immunotherapy target in cancer, which is overexpressed on multiple tumor types, including acute myeloid leukemia [65,66]. A multivalent WT1 peptide vaccine (galinpepimut-S) has been developed and tested in acute myeloid leukemia (AML) patients in phase 1 and 2 clinical trials [67]. In the most recent phase 2 trial (NCT01266083), patients in complete remission received 6 vaccinations administered over 10 weeks with the potential to receive 6 additional monthly doses if they remained in remission. Immune responses (IRs) were evaluated after the 6th and 12th vaccinations by CD4+ T cell proliferation, CD8+ T cell IFN-γ secretion, or the CD8-relevant WT1 peptide major histocompatibility complex tetramer assay. In terms of compliance, 14 patients (64%) completed ≥6 vaccinations, and only 9 (41%) received all 12 vaccine doses. Fifteen patients (68%) relapsed, and 10 (46%) died. The vaccine was well tolerated, with the most common toxicities being grade 1/2 injection site reactions (46%), fatigue (32%), and skin induration (32%). Median disease-free survival from first complete remission was 16.9 months, whereas the overall survival from diagnosis was estimated to be ≥ 5 years. Nine of 14 tested patients (64%) had an IR in ≥1 assay (CD4 or CD8) [67].

There has been extensive pre-clinical research showing efficacy of MAGE-based therapeutic peptide cancer vaccines in the treatment of cancers including melanoma [68-70], NSCLC [71], and breast cancer [72,73]. Deuperret et al. developed a MAGE-A immunogen with cross-reactivity for multiple MAGE-A isoforms. The general domain structure of MAGE-A family is conserved between mice and humans; however, the sequence homology is poor. As a result, separate consensus vaccines were developed for proof-of-concept murine cancer models and for human pre-clinical studies. Mice were vaccinated with the murine MAGE-A consensus vaccine, and the vaccine induced robust CD8+ IFNγ responses to all 6 isoforms predicted to cross-react with this vaccine. To test the antitumoral response, melanoma was induced in Tyr::CreER;BrafCA/þ;Ptenlox/lox mice by administration of topical 4-OHT (tamoxifen). In this melanoma model, the murine MAGE-A consensus vaccine was able to extend survival by 50 days as compared to control cohort [74]. Similar to targeting MAGE epitopes, pre-clinical studies with NY-ESO-1 derived peptides have been conducted in combination with an adjuvant [75-78]. In one study, Albershardt et al. engineered a lentiviral vector, LV305, to deliver NY-ESO-1 to dendritic cells in vivo. Mice immunized with LV305 developed NY-ESO-1 specific cytotoxic T cells within 2 weeks post-immunization, which conferred protection against NY-ESO-1 expressing CT26 lung metastasis. Further, adoptive cell transfer of NY-ESO-1 cytotoxic T cells conferred protection in tumor-bearing recipient mice, confirming transferable immunity [78]. Notably, in 2014 a phase I clinical trial (NCT02122861) to determine the safety profile of LV305 therapeutic cancer vaccine was initiated. There were no significant side effects noted in any of the 30 patients as a result of the cancer vaccine. Anti-NY-ESO-1 specific Th-cells and cytotoxic T cells were induced in 57% of

evaluable sarcoma patients and one patient with synovial sarcoma achieved a partial response lasting more than 3 years. Further, the induction of anti-NY-ESO-1 immune response was found to improve 1-year survival over patients in which vaccination failed to elicit a T cell response [79].

3.3.3 Cell lineage differentiation antigens

Cell lineage differentiation antigens are among the first identified cancer antigens. These include MART-1, gp100, prostate-specific antigen (PSA), and tyrosinase (Tyr). Expression of MART-1 and gp100 is most associated with melanoma. It was first recognized in 1994 that HLA-A*02 restricted cytotoxic T cells derived from tumor infiltrating lymphocytes (TILs) of melanoma patients recognized nonmutated proteins expressed by most melanoma cells. The most frequently recognized proteins were MART-1 and gp100, which was recognized by TILs from 90% and 40% patients, respectively [80,81]. As a result of these early investigations, the MART-127-35 peptide, AAGIGLTV, was among the first to be employed in humans in 1999. In a phase I clinical trial, 23 HLA-A*0201 patients with metastatic melanoma received subcutaneous administration of the MART-127-35 peptide, doses ranging from 0.1 to 10mg, emulsified in incomplete Freund's adjuvant (IFA). Dosing schedule consisted of 4 doses separated by 3-week intervals. While the phase I clinical trial did not induce any clinically significant toxicities, it also failed to demonstrate any therapeutic efficacy at all doses. Furthermore, an analysis of PBMCs from the peripheral blood indicated that there was no correlation between MART-1 specific T cell activation and vaccine dose [82]. Given current understanding of tolerogenic immune cells, in particular the role of myeloid derived suppressor cells (MDSCs) and the role of regulatory T cells in the maintenance of the

immunosuppressive tumor microenvironment, the lack of clinical efficacy might not be surprising.

Despite these suboptimal initial results, the development of cell lineage differentiation targeted vaccines has persisted due to their expression on a variety of cancers. In melanoma, recent studies have focused on developing vaccine strategies which both expand cancer antigen-specific T cells while also suppressing MDSCs. In a pre-clinical study, Yan et al. developed a novel synthetic consensus DNA vaccine against Tyr and tested its efficacy in the highly metastatic and poorly immunogenic B16-F10 murine melanoma model. The DNA vaccine was administered three times at 2-week intervals either in a prophylactic setting 7 days prior B16-F10 inoculation or in a therapeutic setting 7 days after B16-F10 inoculation. The induction of IFN-γ producing T cells by vaccination was assessed by ELISpot assay with T cells isolated from spleen of transfected mice. These studies confirmed the vaccine was able to illicit expansion of Tyr-specific T cells, with Tyr epitopes ‘DWRDAEKCDICTDEY’ and ‘AKHTISSDYVIPIGT’ being dominant. In a prophylactic setting, the vaccine slowed the recruitment of MDSCs to the tumor and was associated with a reduction in the concentration of immunosuppressive IL-10, and MDSC chemoattractant molecules MCP-1 and CXCL5, and decreased tumor growth rate. In a therapeutic setting, similar effects contributed to improving overall survival [83].

3.4| Co-administration of cancer antigen vaccines with immunomodulators

TAA targeted cancer vaccines have been shown to induce antigen specific T cell and antibody responses in pre-clinical studies and in clinical trials. Recent efforts have focused on characterizing the effects of combining TAA targeted cancer vaccines with

existing cancer therapeutics which can modulate the immunosuppressive tumor microenvironment and further improve outcomes.

The presence of TILs is correlated with favorable outcomes with checkpoint blockade therapy, which is a logical prelude for combination with TAA targeted cancer vaccines [84]. Conniot et al. combined a nanoparticle-based cancer vaccine with PD-1 blockade and OX40 co-stimulation. The nanoparticle delivered the Melan-A/MART-126-35 MHC I-restricted peptide and Melan-A/MART-151-73 MHC II-restricted peptide to DCs in the draining lymph nodes, which were shown to potentiate cytotoxic and helper T cell responses, respectively. OX40 is a co-stimulatory receptor member of the TNF family, expressed on activated T cells. Once activated, OX40 induces expansion, trafficking, and pro-inflammatory cytokine production by effector T cells. In mice inoculated with Ret-melanoma cells, this combination therapy restricted melanoma growth and prolonged survival when administered as a prophylactic. When administered as a therapeutic, it was found that the infiltration of MDSCs compromises the effect of the combination therapy. To overcome this limitation, ibrutinib, a small molecule inhibitor which has been shown to limit the generation and migration of MDSCs, was utilized to enhance the effect of the combination therapy. The combination of nanoparticle vaccine, anti-PD-1, OX-40 stimulation, and ibrutinib was able to greatly extend survival in both the ret-melanoma and B16-F10 models of murine melanoma as compared to the combination therapy without ibrutinib [85]. In another study, Sahin et al. developed a personalized melanoma vaccine by developing a computational model to predict cancer neo-epitopes in melanoma patients. First, non-synonymous mutations were identified by comparative exome and RNA sequencing of tumor biopsies and healthy blood cells. The mutations

were ranked according to expression level of mutation-encoding RNA and predicted high binding affinity to autologous HLA class I / class II. 10 mutations were selected per patient and engineered into synthetic RNAs and used as the basis of an RNA vaccine to be administered to DCs in draining lymph nodes, which in mouse studies, showed efficient uptake by DCs and antigenicity [86]. In clinical trials, the vaccine was well tolerated in all patients, with each patient developing T cells against at least 3 mutations and pre-existing weak responses against 1/3 of immunogenic neo-epitopes were augmented upon vaccination. One patient experienced multiple relapses and progressing metastases at the start of vaccination despite a strong T cell response against six neo-antigens. For this patient, a compassionate pembrolizumab treatment program was initiated which, strikingly, lead to an 80% decrease in size of multiple melanoma lesions and, eventually, complete response. Notably, neo-epitope specific T cell subsets were PD-1+ and post-vaccine lesions were shown to upregulate PD-L1 [87].

Combination therapies involving chemotherapeutics have also shown promise in treating various types of cancers. For example, numerous clinical studies have shown that checkpoint inhibitors in combination with chemotherapy are associated with significantly longer overall survival and progression-free survival as compared to chemotherapy alone in patients with advanced non-small cell lung carcinoma [24]. This is not entirely unexpected as many chemotherapeutics increase the number of tumor infiltrating cytotoxic T cells or reduce the number of Tregs [88-90]. Therefore, combining chemotherapeutics and TAA-targeted cancer vaccines may have a synergistic effect which is corroborated by the results of recent pre-clinical studies [91-93]. In one such study, Shah et al. developed an AML-vaccine comprised of a macroporous PEG-alginate-

based scaffold and incorporation of GM-CSF, CpG-ODN, and AML-associated antigens in the form of either freeze-thaw lysates derived from bone marrow of AML-infected mice or WT1 peptide [93]. Both vaccine formulations were associated with expansion of WT1 tetramer specific cytotoxic T cells in the peripheral blood within a week of vaccination. Notably, both vaccine formulations provided prophylactic protection against MLL-AF9 AML in 100% of mice when administered 10 days prior to AML inoculation and mice survived an AML re-challenge approximately 3 months later. Next, the WT1 AML-vaccine was tested in a therapeutic model of established AML in combination with standard induction chemotherapy (iCt) regimen of cytarabine (Ara-C) and doxorubicin [94]. Leukemia burden was reduced in mice after iCt treatment, but AML relapsed between day 25 and 35. The WT1 AML-vaccine alone provided prolonged survival, but ultimately did not improve overall survival. However, the iCt and WT1 AML-vaccine combination therapy was effective in mediating therapeutic protection in 100% of mice. Interestingly, combining iCt with an antigen-free vaccine durably depleted leukemia in all mice, dependent on both encapsulation and release of GM-CSF and CpG-ODN, and in which immunogenic cell death of AML cells recruited to the cryogel scaffold may have contributed to the efficacy of this strategy.

In a study to stimulate the endogenous immune response to overcome established advanced tumors, Moynihan et. al. used combination cancer vaccine and immunotherapy to potentiate an immune response [95]. The study was motivated by the development of a strategy to efficiently target peptide vaccines to lymph nodes, and the clinical success with checkpoint blockade therapy [96]. The combinations consisted of A (tumor-antigen-specific antibody), I (MSA–IL-2), P (anti-PD-1) and V (amphiphile–vaccine). Component

V was a potent lymph-node (LN)-targeted vaccine composed of peptide antigens and CpG DNA conjugated to albumin-binding lipids that reversibly bind to interstitial albumin and efficiently traffic to LNs, leading to robust T cell responses. In multiple syngeneic tumor models, this quaternary combination immunotherapy cured a majority of mice with established tumors and elicited long-lived protective T cell memory responses. Notably, all four components incorporated in AIPV were required for treatment of several difficult-to-treat tumor models. The results from the multiple tumor models revealed distinct hierarchies of importance for the four components. For example, the monoclonal antibody component was a critical contributor to efficacy in the B16F10 model, but it was the least important component in the DD-Her2/neu model. A key aspect of AIPV treatment was that this set of four agents collectively mounted an integrated response that overcomes tumor resistance mechanisms in all of the models evaluated here, suggesting that the appropriate combination of immune effectors can overcome a range of obstacles present in tumor microenvironments.

3.4 Conclusions

The studies reviewed here highlight advances in the development of cancer vaccines and synergies afforded by combining cancer vaccines with chemotherapy and immune checkpoint blockade. Therapeutic cancer vaccinations strategies can be broadly categorized by their delivery vehicle and antigen target, each with their own distinct properties.

DC vaccines induce expansion of T cells with a broad T cell receptor repertoire, allowing for a more sustained and robust immune response. Thus far, the only FDA approved DC vaccine formulation is Provenge [34]. While this is an attractive personalized cancer vaccine cell therapy, the labor-intensive manufacturing process and a modest improvement in overall survival has hindered its applicability. Vaccines such as WDVAX and allogenic DC vaccines such as GVAX and DCP-001 are attractive alternatives as they avoid the need for personalized cell-manufacturing, and are scalable therapies [44-46]. Further, new DC vaccine formulations preclude identification of specific cancer antigens, which may broaden their applicability to a larger number of cancer patients.

DNA- or peptide-based cancer antigen targeted vaccines act on DCs in the lymph nodes. The vaccines expand antigen specific T cells which mediate cancer cell lysis, which in turn allows for DC priming of tumor-associated antigens in a manner analogous to DC vaccines. While these therapies are generally scalable, their scope is limited by variability in expression levels of antigen targets and are therefore available to a subset of cancer patients. In addition, since distribution of expressed cancer antigens is dependent on the cancer type, different formulations must be designed and tested to treat different cancers. To allow antigen targeted vaccines to reach more patients, the development of personalized cancer vaccine strategies is an important research area [87,97]. Beyond reaching more patients, personalized vaccines incorporate multiple antigen targets, thus enhancing T cell receptor repertoire of initial immune response. However, since the antigen targets of these vaccines would likely differ between patients, the regulatory approval of such an approach may require a new mechanism.

In many of the clinical studies, cancer vaccines elicited a robust T cell response but were unable to mediate sustained tumor regression, in part, due to the immunosuppressive tumor microenvironment. Thus, combining cancer vaccines with immunomodulators such as chemotherapy or checkpoint blockade was thought to enhance their efficacy. Indeed, pre-clinical and early clinical data suggests that combining therapeutic cancer vaccines with either chemotherapy or checkpoint blockade allows for enhanced synergy when compared to a monotherapy. Based on existing research, the combination of cancer vaccines with chemotherapy or immune checkpoint blockade represent the most probable path towards clinical translation of therapeutic cancer vaccines.

3.5 Expert Opinion

Vaccination as a means to prevent cancer or cancer relapse has been a long-sought goal of cancer therapy, supported by decades of research in preclinical models and in patients that T cells can be educated to target tumor cells. For cancers with a microbial etiology, vaccination has been highly effective in reducing the incidence of disease [98]. However, vaccination against established malignancy has been largely disappointing [99]. Until recently, it was generally believed that when used in combination with a cancer vaccine, cytoreductive therapy would invariably have a negative effect on vaccine-mediated immune responses and antitumor activity. However, a greater depth of understanding has suggested that the immunomodulatory properties of cytoreductive regimens might be exploited to enhance vaccine-mediated antitumor effects [100]. This synergy can be mediated by multiple mechanisms, depending on the type of cytotoxic agent and the specific vaccine employed, as well as the dosing schedule of each modality. Therefore, an increasing amount of clinical and pre-clinical data supports the use of a combination

approach involving immunotherapy and front-line chemotherapy drugs as the standard method to effectively treat multiple types of cancers [101]. Therapeutic cancer vaccines have been shown to be immunogenic in clinical trials, and many of them have demonstrated efficacy in at least small numbers of patients [102]. Dendritic cell-based therapeutic cancer vaccines have been approved for clinical use, and their combination with checkpoint inhibitors is highly developed for clinical applications. Cancer-specific subunit cancer vaccines offer the possibility of an off-the-shelf approach for therapeutic cancer vaccines. Cancer vaccines are an effective means to address 'immune ignorant' tumors, which have a poor prognosis regardless of any current intervention. The efficient delivery of vaccine components will support the successful development of methods to activate tumor specific immune responses [103].

Given the complex interactions between cancer cells and the many components of their environment, it is reasonable to postulate that the future of immunotherapy lies in the combination of complementary immunotherapeutic strategies with chemotherapeutics or other oncogenic pathway inhibitors. The optimal approach will likely vary substantially between tumor types and may even be patient specific. This is a particularly important consideration as the rate of progress in the understanding of tumor immunology and clinical application of immunomodulatory agents has varied substantially between different types of cancers [104]. Tumors may be heterogeneous and develop clinical resistance to monotherapies and efficient antitumor strategies must focus on hitting different targets concurrently. In general, greater host and disease heterogeneity are associated with fewer options and poorer outcomes. Combination strategies will need to account for the unique genetic, epigenetic, and complexity of the cancer. By modulating

inhibitory molecules, regulatory immune cells, and the metabolic resources and demands of T cells, vaccine-stimulated T cells might be induced to be fully functional within the immunosuppressive tumor microenvironment. In making therapy decisions identifying reliable biomarkers to improve patient selection, standardizing metrics for monitoring toxicities and comprehensive knowledge about the timing and dose of combination therapies will be important factors for successful development. The process will likely be iterative, as new cancer vaccine technologies are developed and more targeted immunotherapies are available which may lower toxicities while providing durable protection against cancer relapse.

3.6 Figure

Figure 3.1| Targets of Cancer Immunotherapies
To generate a sustained T cell response against tumors, dendritic cells (DCs) uptake and present cancer antigens to T cells. Subsequently, T cells migrate to the tumor site and seek to induce cancer cell death. (1) Cancer vaccines aim to facilitate the process of antigen presentation of DCs by providing an initial source of cancer antigens. T cells that recognize these cancer antigens are activated and migrate to the tumor site to initiate cancer-cell lysis. (2) Many cancer cells upregulate immunosuppressive checkpoint blockade ligands to inactivate T cells. Thus, combining therapeutic cancer vaccines with checkpoint blockade therapy may enhance anti-tumoral efficacy and allow for better clinical outcomes. (3) Chemotherapies are generally cytoreductive and may enhance the effect of cancer vaccines by reducing concentration of immunosuppressive regulatory T cells within the tumor microenvironment thereby accentuating the vaccine mediated cytotoxic T cell response.

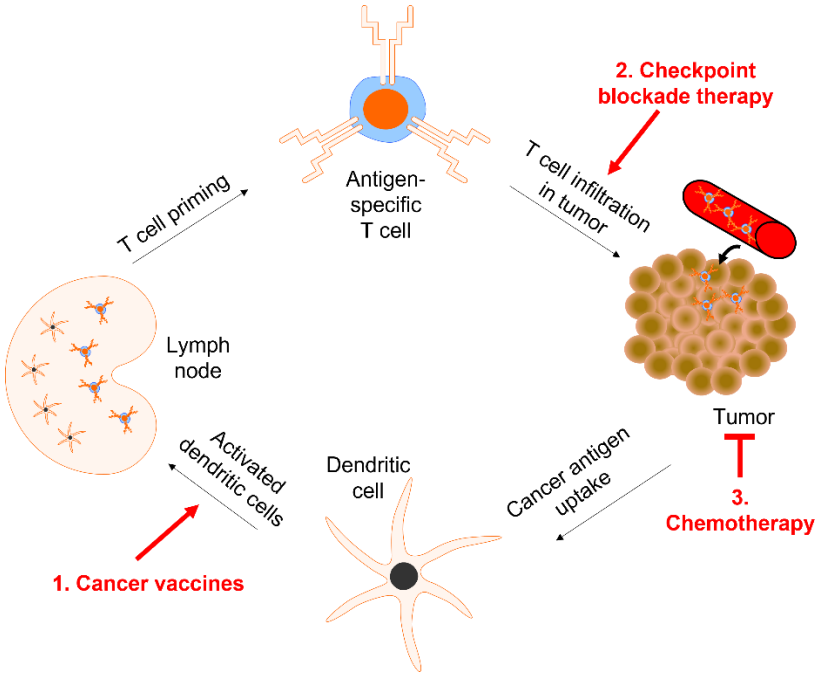

3.7 Table

Table 3.1| Selected Pre-Clinical Cancer Vaccine Results

PLG, poly(lactic-co-glycolic acid); GM-CSF, granulocyte-macrophage colony stimulating factor; CpG-ODN, Cytosine-guanosine oligonucleotide; CTLA-4, cytotoxic T-lymphocyte-associated protein 4; CEA, carcinoembryonic antigen; NY-ESO-1, cancer/testis antigen 1; WT1, Wilms tumor 1

Components	Cancer Type	Key Takeaways	Reference Number
PLG scaffold loaded with tumor lysis, GM-CSF, and CpG-ODN	Melanoma (B16-F10)	Vaccine formulation was able to provide both prophylactic and therapeutic protection in mice.	45
GVAX cancer vaccine and anti-CTLA-4 combination	Prostate cancer (Pro-TRAMP)	Timing of checkpoint blockade and cancer vaccine administration are important. Administration of anti-CTLA-4 before or concurrent to GVAX showed no enhancement in anti-tumoral response whereas administration after GVAX showed improved survival.	51
Viral vector encoding CEA and GM-CSF plasmid	Colon adenocarcinoma (MC38-CEA)	Viral vector encoding CEA administered in combination with GM-CSF plasmid can provide prophylactic protection against MC38-CEA colon adenocarcinoma model.	64
Lentiviral vector encoding NY-ESO-1	Lung Cancer (CT26 expressing NY-ESO-1)	Viral vaccine generated NY-ESO-1 specific T-cells and was able to provide prophylactic protection against NY-ESO-1 expressing lung cancer model.	78
DNA vaccine against tyrosinase	Melanoma (B16-F10)	DNA vaccine was effective in both prophylactic and therapeutic setting against B16-F10 melanoma.	83
Alginate-based scaffold loaded with GM-CSF, CpG-ODN, and WT1 peptide in combination with cytarabine and doxorubicin	Acute myeloid leukemia (MLL-AF9)	Vaccine was able to provide prophylactic protection against MLL-AF9 acute myeloid leukemia. In therapeutic setting, it was able to provide complete protection if administered alongside standard induction chemotherapy regimen of cytarabine and doxorubicin.	94

3.8 Author Disclosures

The authors have no relevant competing financial interests or relationships that could have influenced the content in this paper.

Chapter 3, in full, is a reprint of the material as it appears in Expert Opinion on Drug Discovery. 2020, with the following authors Matthew D. Kerr, David A. McBride, Arun K. Chumber, Nisarg J. Shah. The dissertation author was the primary author of this review paper.

3.9 References

1. Mellman I, Coukos G, Dranoff G: Cancer immunotherapy comes of age. Nature 2011, 480:480-489.
2. Farkona S, Diamandis EP, Blasutig IM: Cancer immunotherapy: the beginning of the end of cancer? BMC medicine 2016, 14:73.
3. Pardoll DM: The blockade of immune checkpoints in cancer immunotherapy. Nature Reviews Cancer 2012, 12:252-264.
4. Tseng D, Schultz L, Pardoll D, Mackall C: Cancer Immunology. In Abeloff's Clinical Oncology. Edited by: Elsevier; 2020:84-96. e85.
5. Wu R, Forget M-A, Chacon J, Bernatchez C, Haymaker C, Chen JQ, Hwu P, Radvanyi L: Adoptive T-cell therapy using autologous tumor-infiltrating lymphocytes for metastatic melanoma: current status and future outlook. Cancer journal (Sudbury, Mass.) 2012, 18:160.
6. Lee PP, Yee C, Savage PA, Fong L, Brockstedt D, Weber JS, Johnson D, Swetter S, Thompson J, Greenberg PD: Characterization of circulating T cells specific for

tumor-associated antigens in melanoma patients. Nature medicine 1999, 5:677-685.

7. Yee C, Greenberg P: Modulating T-cell immunity to tumours: new strategies for monitoring T-cell responses. Nature Reviews Cancer 2002, 2:409-419.

8. Zhang L, Conejo-Garcia JR, Katsaros D, Gimotty PA, Massobrio M, Regnani G, Makrigiannakis A, Gray H, Schlienger K, Liebman MN: Intratumoral T cells, recurrence, and survival in epithelial ovarian cancer. New England journal of medicine 2003, 348:203-213.

9. John SY, Liu G, Ying H, Yong WH, Black KL, Wheeler CJ: Vaccination with tumor lysate-pulsed dendritic cells elicits antigen-specific, cytotoxic T-cells in patients with malignant glioma. Cancer research 2004, 64:4973-4979.

10. Tosolini M, Kirilovsky A, Mlecnik B, Fredriksen T, Mauger S, Bindea G, Berger A, Bruneval P, Fridman W-H, Pagès F: Clinical impact of different classes of infiltrating T cytotoxic and helper cells (Th1, th2, treg, th17) in patients with colorectal cancer. Cancer research 2011, 71:1263-1271.

11. Franco EL, Harper DM: Vaccination against human papillomavirus infection: a new paradigm in cervical cancer control. Vaccine 2005, 23:2388-2394.

12. Martin D, Gutkind J: Human tumor-associated viruses and new insights into the molecular mechanisms of cancer. Oncogene 2008, 27:S31-S42.

13. Saraiya M, Unger ER, Thompson TD, Lynch CF, Hernandez BY, Lyu CW, Steinau M, Watson M, Wilkinson EJ, Hopenhayn C: US assessment of HPV types in cancers: implications for current and 9-valent HPV vaccines. JNCI: Journal of the National Cancer Institute 2015, 107.

14. Melief CJ, van Hall T, Arens R, Ossendorp F, van der Burg SH: Therapeutic cancer vaccines. The Journal of clinical investigation 2015, 125:3401-3412.

15. Yadav M, Jhunjhunwala S, Phung QT, Lupardus P, Tanguay J, Bumbaca S, Franci C, Cheung TK, Fritsche J, Weinschenk T: Predicting immunogenic tumour mutations by combining mass spectrometry and exome sequencing. Nature 2014, 515:572-576.

**Describes novel method of identifying novel neo-epitopes in murine tumor models.

16. Gilboa E: How tumors escape immune destruction and what we can do about it. Cancer Immunology, Immunotherapy 1999, 48:382-385.

17. Havel JJ, Chowell D, Chan TA: The evolving landscape of biomarkers for checkpoint inhibitor immunotherapy. Nature Reviews Cancer 2019, 19:133-150.

18. Moyer TJ, Zmolek AC, Irvine DJ: Beyond antigens and adjuvants: formulating future vaccines. The Journal of clinical investigation 2016, 126:799-808.

19. Overwijk WW: Cancer vaccines in the era of checkpoint blockade: the magic is in the adjuvant. Current opinion in immunology 2017, 47:103-109.

20. Majzner RG, Mackall CL: Clinical lessons learned from the first leg of the CAR T cell journey. Nature medicine 2019, 25:1341-1355.

21. Pusuluri A, Wu D, Mitragotri S: Immunological consequences of chemotherapy: Single drugs, combination therapies and nanoparticle-based treatments. Journal of Controlled Release 2019, 305:130-154.

22. Reck M, Rodríguez-Abreu D, Robinson AG, Hui R, Csőszi T, Fülöp A, Gottfried M, Peled N, Tafreshi A, Cuffe S, et al.: Pembrolizumab versus Chemotherapy for PD-

L1–Positive Non–Small-Cell Lung Cancer. New England Journal of Medicine 2016, 375:1823-1833.

23. Shen X, Zhang L, Li J, Li Y, Wang Y, Xu Z-X: Recent Findings in the Regulation of Programmed Death Ligand 1 Expression. Frontiers in Immunology 2019, 10:1337-1337.

24. Addeo A, Banna GL, Metro G, Di Maio M: Chemotherapy in Combination With Immune Checkpoint Inhibitors for the First-Line Treatment of Patients With Advanced Non-small Cell Lung Cancer: A Systematic Review and Literature-Based Meta-Analysis. Frontiers in Oncology 2019, 9.

25. Nuhn P, De Bono JS, Fizazi K, Freedland SJ, Grilli M, Kantoff PW, Sonpavde G, Sternberg CN, Yegnasubramanian S, Antonarakis ES: Update on systemic prostate cancer therapies: management of metastatic castration-resistant prostate cancer in the era of precision oncology. European urology 2019, 75:88-99.

26. Kwon ED, Drake CG, Scher HI, Fizazi K, Bossi A, van den Eertwegh AJM, Krainer M, Houede N, Santos R, Mahammedi H, et al.: Ipilimumab versus placebo after radiotherapy in patients with metastatic castration-resistant prostate cancer that had progressed after docetaxel chemotherapy (CA184-043): a multicentre, randomised, double-blind, phase 3 trial. The Lancet. Oncology 2014, 15:700-712.

27. Ozpiskin OM, Zhang L, Li JJ: Immune targets in the tumor microenvironment treated by radiotherapy. Theranostics 2019, 9:1215.

28. Weiss T, Weller M, Roth P: Immunological effects of chemotherapy and radiotherapy against brain tumors. Expert review of anticancer therapy 2016, 16:1087-1094.

29. Hader M, Frey B, Fietkau R, Hecht M, Gaipl US: Immune biological rationales for the design of combined radio-and immunotherapies. Cancer Immunology, Immunotherapy 2020, 69:293-306.

30. Jung S, Unutmaz D, Wong P, Sano G-I, De los Santos K, Sparwasser T, Wu S, Vuthoori S, Ko K, Zavala F, et al.: In Vivo Depletion of CD11c+ Dendritic Cells Abrogates Priming of CD8+ T Cells by Exogenous Cell-Associated Antigens. Immunity 2002, 17:211-220.

31. Mempel TR, Henrickson SE, von Andrian UH: T-cell priming by dendritic cells in lymph nodes occurs in three distinct phases. Nature 2004, 427:154-159.

32. Torralba D, Baixauli F, Villarroya-Beltri C, Fernández-Delgado I, Latorre-Pellicer A, Acín-Pérez R, Martín-Cófreces NB, Jaso-Tamame ÁL, Iborra S, Jorge I, et al.: Priming of dendritic cells by DNA-containing extracellular vesicles from activated T cells through antigen-driven contacts. Nature Communications 2018, 9:2658.

33. Palucka K, Banchereau J: Dendritic-cell-based therapeutic cancer vaccines. Immunity 2013, 39:38-48.

34. Cheever MA, Higano CS: PROVENGE (Sipuleucel-T) in Prostate Cancer: The First FDA-Approved Therapeutic Cancer Vaccine. Clinical Cancer Research 2011, 17:3520.

**Overviews of clinical data leading to approval of Provenge vaccine.

35. Arlen Philip M, Skarupa L, Pazdur M, Seetharam M, Tsang Kwong Y, Grosenbach Douglas W, Feldman J, Poole Diane J, Litzinger M, Steinberg Seth M, et al.: Clinical Safety of a Viral Vector Based Prostate Cancer Vaccine Strategy. Journal of Urology 2007, 178:1515-1520.

36. Kantoff PW, Schuetz TJ, Blumenstein BA, Glode LM, Bilhartz DL, Wyand M, Manson K, Panicali DL, Laus R, Schlom J, et al.: Overall survival analysis of a phase II randomized controlled trial of a Poxviral-based PSA-targeted immunotherapy in metastatic castration-resistant prostate cancer. Journal of clinical oncology : official journal of the American Society of Clinical Oncology 2010, 28:1099-1105.

37. Guo Y, Walsh AM, Canavan M, Wechalekar MD, Cole S, Yin X, Scott B, Loza M, Orr C, McGarry T, et al.: Immune checkpoint inhibitor PD-1 pathway is down-regulated in synovium at various stages of rheumatoid arthritis disease progression. PloS one 2018, 13:e0192704-e0192704.

38. Weinmann SC, Pisetsky DS: Mechanisms of immune-related adverse events during the treatment of cancer with immune checkpoint inhibitors. Rheumatology (Oxford, England) 2019, 58:vii59-vii67.

39. Avigan D, Rosenblatt J: Vaccine therapy in hematologic malignancies. Blood 2018, 131:2640-2650.

40. van de Loosdrecht AA, van Wetering S, Santegoets SJ, Singh SK, Eeltink CM, den Hartog Y, Koppes M, Kaspers J, Ossenkoppele GJ, Kruisbeek AM: A novel allogeneic off-the-shelf dendritic cell vaccine for post-remission treatment of elderly patients with acute myeloid leukemia. Cancer Immunology, Immunotherapy 2018, 67:1505-1518.

*Describes phase I study of novel allogenic DC vaccine, DCP-001.

41. Simons JW, Jaffee EM, Weber CE, Levitsky HI, Nelson WG, Carducci MA, Lazenby AJ, Cohen LK, Finn CC, Clift SM, et al.: Bioactivity of autologous irradiated renal

cell carcinoma vaccines generated by ex vivo granulocyte-macrophage colony-stimulating factor gene transfer. Cancer research 1997, 57:1537-1546.

42. Shirota H, Klinman DM: CpG-conjugated apoptotic tumor cells elicit potent tumor-specific immunity. Cancer immunology, immunotherapy : CII 2011, 60:659-669.

43. Curry WT, Jr., Gorrepati R, Piesche M, Sasada T, Agarwalla P, Jones PS, Gerstner ER, Golby AJ, Batchelor TT, Wen PY, et al.: Vaccination with Irradiated Autologous Tumor Cells Mixed with Irradiated GM-K562 Cells Stimulates Antitumor Immunity and T Lymphocyte Activation in Patients with Recurrent Malignant Glioma. Clinical cancer research : an official journal of the American Association for Cancer Research 2016, 22:2885-2896.

44. Ali OA, Huebsch N, Cao L, Dranoff G, Mooney DJ: Infection-mimicking materials to program dendritic cells in situ. Nature materials 2009, 8:151-158.

**Describes development of PLG scaffold designed to release GM-CSF to recruit DCs.

45. Ali OA, Emerich D, Dranoff G, Mooney DJ: In situ regulation of DC subsets and T cells mediates tumor regression in mice. Science translational medicine 2009, 1:8ra19-18ra19.

**PLG based cancer vccine mediates prophylactic and therapeutic protection against B16 melanoma in mice.

46. Jaffee EM, Hruban RH, Biedrzycki B, Laheru D, Schepers K, Sauter PR, Goemann M, Coleman J, Grochow L, Donehower RC, et al.: Novel Allogeneic Granulocyte-Macrophage Colony-Stimulating Factor–Secreting Tumor Vaccine for Pancreatic

Cancer: A Phase I Trial of Safety and Immune Activation. Journal of Clinical Oncology 2001, 19:145-156.

**Phase I study of GVAX, a GM-CSF transfected allogenic pancreatic cancer cell based therapeutic cancer vaccine.

47. Lutz E, Yeo CJ, Lillemoe KD, Biedrzycki B, Kobrin B, Herman J, Sugar E, Piantadosi S, Cameron JL, Solt S, et al.: A lethally irradiated allogeneic granulocyte-macrophage colony stimulating factor-secreting tumor vaccine for pancreatic adenocarcinoma. A Phase II trial of safety, efficacy, and immune activation. Annals of surgery 2011, 253:328-335.

48. Santegoets SJAM, Schreurs MWJ, Masterson AJ, Liu YP, Goletz S, Baumeister H, Kueter EWM, Lougheed SM, van den Eertwegh AJM, Scheper RJ, et al.: In vitro priming of tumor-specific cytotoxic T lymphocytes using allogeneic dendritic cells derived from the human MUTZ-3 cell line. Cancer Immunology, Immunotherapy 2006, 55:1480-1490.

49. van de Loosdrecht AA, van Wetering S, Santegoets SJAM, Singh SK, Eeltink CM, den Hartog Y, Koppes M, Kaspers J, Ossenkoppele GJ, Kruisbeek AM, et al.: A novel allogeneic off-the-shelf dendritic cell vaccine for post-remission treatment of elderly patients with acute myeloid leukemia. Cancer Immunology, Immunotherapy 2018, 67:1505-1518.

50. Li B, VanRoey M, Wang C, Chen T-hT, Korman A, Jooss K: Anti–Programmed Death-1 Synergizes with Granulocyte Macrophage Colony-Stimulating Factor–Secreting Tumor Cell Immunotherapy Providing Therapeutic Benefit to Mice with Established Tumors. Clinical Cancer Research 2009, 15:1623.

51. Wada S, Jackson CM, Yoshimura K, Yen H-R, Getnet D, Harris TJ, Goldberg MV, Bruno TC, Grosso JF, Durham N, et al.: Sequencing CTLA-4 blockade with cell-based immunotherapy for prostate cancer. Journal of Translational Medicine 2013, 11:89-89.

**Relative timing of administration of GVAX cancer vaccine and checkpoint blockade, anti-CTLA-4, is an important parameter in enhancing cancer vaccine efficacy.

52. Duraiswamy J, Kaluza KM, Freeman GJ, Coukos G: Dual blockade of PD-1 and CTLA-4 combined with tumor vaccine effectively restores T-cell rejection function in tumors. Cancer Research 2013, 73:3591-3603.

*Enhanced efficacy of GVAX vaccine when combined with dual PD-1 and CTLA-4 checkpoint blockade.

53. Santos PM, Adamik J, Howes TR, Du S, Vujanovic L, Warren S, Gambotto A, Kirkwood JM, Butterfield LH: Impact of checkpoint blockade on cancer vaccine–activated CD8+ T cell responses. Journal of Experimental Medicine 2020, 217.

54. Versteven M, Van den Bergh JM, Marcq E, Smits EL, Van Tendeloo VF, Hobo W, Lion E: Dendritic cells and programmed death-1 blockade: a joint venture to combat cancer. Frontiers in immunology 2018, 9:394.

55. Mouraviev V, Mariados N, Albala D, Concepcion RS, Shore ND, Sims RB, Emberton M, Pieczonka CM: The Rationale for Optimal Combination Therapy With Sipuleucel-T for Patients With Castration-resistant Prostate Cancer. Reviews in urology 2014, 16:122-130.

56. Hollingsworth RE, Jansen K: Turning the corner on therapeutic cancer vaccines. NPJ vaccines 2019, 4:1-10.

57. Kerk SA, Finkel KA, Pearson AT, Warner KA, Zhang Z, Nör F, Wagner VP, Vargas PA, Wicha MS, Hurt EM: 5T4-targeted therapy ablates cancer stem cells and prevents recurrence of head and neck squamous cell carcinoma. Clinical Cancer Research 2017, 23:2516-2527.

58. Wang L, Pan L, Yao M, Cai Y, Dong Z, Yao D: Expression of oncofetal antigen glypican-3 associates significantly with poor prognosis in HBV-related hepatocellular carcinoma. Oncotarget 2016, 7:42150.

59. Kalyan A, Kircher S, Shah H, Mulcahy M, Benson A: Updates on immunotherapy for colorectal cancer. Journal of gastrointestinal oncology 2018, 9:160.

60. Warnecke-Eberz U, Metzger R, Hölscher AH, Drebber U, Bollschweiler E: Diagnostic marker signature for esophageal cancer from transcriptome analysis. Tumor Biology 2016, 37:6349-6358.

61. Cua S, Tan HL, Fong WJ, Chin A, Lau A, Ding V, Song Z, Yang Y, Choo A: Targeting of embryonic annexin A2 expressed on ovarian and breast cancer by the novel monoclonal antibody 2448. Oncotarget 2018, 9:13206.

62. Hirayama M, Tomita Y, Yuno A, Tsukamoto H, Senju S, Imamura Y, Sayem MA, Irie A, Yoshitake Y, Fukuma D, et al.: An oncofetal antigen, IMP-3-derived long peptides induce immune responses of both helper T cells and CTLs. Oncoimmunology 2016, 5:e1123368-e1123368.

63. Tamai T, Mizukoshi E, Kumagai M, Terashima T, Iida N, Kitahara M, Shimakami T, Kitamura K, Arai K, Yamashita T, et al.: A novel α-fetoprotein-derived helper T-

lymphocyte epitope with strong immunogenicity in patients with hepatocellular carcinoma. Scientific Reports 2020, 10:4021.

64. Hensel JA, Khattar V, Ashton R, Ponnazhagan S: Recombinant AAV-CEA Tumor Vaccine in Combination with an Immune Adjuvant Breaks Tolerance and Provides Protective Immunity. Molecular therapy oncolytics 2018, 12:41-48.

**Describes development of rAAV-CEA cancer vaccine and its ability to mediate prophylactic protection against murine MC38-CEA colon adenocarcinoma.

65. Cheever MA, Allison JP, Ferris AS, Finn OJ, Hastings BM, Hecht TT, Mellman I, Prindiville SA, Viner JL, Weiner LM, et al.: The prioritization of cancer antigens: a national cancer institute pilot project for the acceleration of translational research. Clinical cancer research : an official journal of the American Association for Cancer Research 2009, 15:5323-5337.

66. Chapuis AG, Egan DN, Bar M, Schmitt TM, McAfee MS, Paulson KG, Voillet V, Gottardo R, Ragnarsson GB, Bleakley M: T cell receptor gene therapy targeting WT1 prevents acute myeloid leukemia relapse post-transplant. Nature Medicine 2019, 25:1064-1072.

67. Maslak PG, Dao T, Bernal Y, Chanel SM, Zhang R, Frattini M, Rosenblat T, Jurcic JG, Brentjens RJ, Arcila ME, et al.: Phase 2 trial of a multivalent WT1 peptide vaccine (galinpepimut-S) in acute myeloid leukemia. Blood Adv 2018, 2:224-234.

68. Batchu RB, Gruzdyn O, Potti RB, Weaver DW, Gruber SA: MAGE-A3 With Cell-Penetrating Domain as an Efficient Therapeutic Cancer Vaccine. JAMA Surgery 2014, 149:451-457.

69. Gérard C, Baudson N, Ory T, Louahed J: Tumor mouse model confirms MAGE-A3 cancer immunotherapeutic as an efficient inducer of long-lasting anti-tumoral responses. PloS one 2014, 9:e94883-e94883.

70. Junwei W, Xiumin Z, Jing Y, Shoujing Y, Zengshan L: In vivo enhancement of the MAGE-specific cellular immune response by a recombinant MAGE1-MAGE3-TBHSP70 tumor vaccine. Cancer Cell International 2016, 16:45.

71. Gérard C, Baudson N, Ory T, Louahed J: Tumor Mouse Model Confirms MAGE-A3 Cancer Immunotherapeutic As an Efficient Inducer of Long-Lasting Anti-Tumoral Responses. PloS one 2014, 9:e94883.

72. Sypniewska RK, Hoflack L, Tarango M, Gauntt S, Leal BZ, Reddick RL, Gravekamp C: Prevention of metastases with a Mage-b DNA vaccine in a mouse breast tumor model: potential for breast cancer therapy. Breast Cancer Research and Treatment 2005, 91:19-28.

73. Castro F, Leal B, Denny A, Bahar R, Lampkin S, Reddick R, Lu S, Gravekamp C: Vaccination with Mage-b DNA induces CD8 T-cell responses at young but not old age in mice with metastatic breast cancer. British journal of cancer 2009, 101:1329-1337.

74. Duperret EK, Liu S, Paik M, Trautz A, Stoltz R, Liu X, Ze K, Perales-Puchalt A, Reed C, Yan J, et al.: A Designer Cross-reactive DNA Immunotherapeutic Vaccine that Targets Multiple MAGE-A Family Members Simultaneously for Cancer Therapy. Clinical cancer research : an official journal of the American Association for Cancer Research 2018, 24:6015-6027.

**Describes development of MAGE-A cancer vaccine with cross-reactivity for multiple MAGE-A isoforms.

75. Parvanova I, Rettig L, Knuth A, Pascolo S: The form of NY-ESO-1 antigen has an impact on the clinical efficacy of anti-tumor vaccination. Vaccine 2011, 29:3832-3836.

76. Li M, Shi H, Mu Y, Luo Z, Zhang H, Wan Y, Zhang D, Lu L, Men K, Tian Y, et al.: Effective inhibition of melanoma tumorigenesis and growth via a new complex vaccine based on NY-ESO-1-alum-polysaccharide-HH2. Molecular cancer 2014, 13:179-179.

77. Xue W, Metheringham RL, Brentville VA, Gunn B, Symonds P, Yagita H, Ramage JM, Durrant LG: SCIB2, an antibody DNA vaccine encoding NY-ESO-1 epitopes, induces potent antitumor immunity which is further enhanced by checkpoint blockade. OncoImmunology 2016, 5:e1169353.

78. Albershardt TC, Campbell DJ, Parsons AJ, Slough MM, ter Meulen J, Berglund P: LV305, a dendritic cell-targeting integration-deficient ZVexTM-based lentiviral vector encoding NY-ESO-1, induces potent anti-tumor immune response. Molecular Therapy - Oncolytics 2016, 3:16010.

**Describes development of LV305 cancer vaccine to provide protection against NY-ESO-1 expressing CT26 lung cancer model.

79. Somaiah N, Block MS, Kim JW, Shapiro GI, Do KT, Hwu P, Eder JP, Jones RL, Lu H, ter Meulen J, et al.: First-in-Class, First-in-Human Study Evaluating LV305, a Dendritic-Cell Tropic Lentiviral Vector, in Sarcoma and Other Solid Tumors Expressing NY-ESO-1. Clinical Cancer Research 2019:clincanres.1025.2019.

80. Kawakami Y, Eliyahu S, Delgado CH, Robbins PF, Rivoltini L, Topalian SL, Miki T, Rosenberg SA: Cloning of the gene coding for a shared human melanoma antigen recognized by autologous T cells infiltrating into tumor. Proceedings of the National Academy of Sciences of the United States of America 1994, 91:3515-3519.

81. Kawakami Y, Eliyahu S, Sakaguchi K, Robbins PF, Rivoltini L, Yannelli JR, Appella E, Rosenberg SA: Identification of the immunodominant peptides of the MART-1 human melanoma antigen recognized by the majority of HLA-A2-restricted tumor infiltrating lymphocytes. The Journal of experimental medicine 1994, 180:347-352.

82. Cormier JN, Salgaller ML, Prevette T, Barracchini KC, Rivoltini L, Restifo NP, Rosenberg SA, Marincola FM: Enhancement of cellular immunity in melanoma patients immunized with a peptide from MART-1/Melan A. The cancer journal from Scientific American 1997, 3:37-44.

83. Yan J, Tingey C, Lyde R, Gorham TC, Choo DK, Muthumani A, Myles D, Weiner LP, Kraynyak KA, Reuschel EL, et al.: Novel and enhanced anti-melanoma DNA vaccine targeting the tyrosinase protein inhibits myeloid-derived suppressor cells and tumor growth in a syngeneic prophylactic and therapeutic murine model. Cancer Gene Therapy 2014, 21:507-517.

**Describes development of DNA vaccine against Tyr and its effectiveness in both prophylactic and therapeutic protection against

84. Tumeh PC, Harview CL, Yearley JH, Shintaku IP, Taylor EJM, Robert L, Chmielowski B, Spasic M, Henry G, Ciobanu V, et al.: PD-1 blockade induces responses by inhibiting adaptive immune resistance. Nature 2014, 515:568-571.

*Presence of TILs is assoicated with favorable outcomes with checkpoint blockade therapy.

85. Conniot J, Scomparin A, Peres C, Yeini E, Pozzi S, Matos AI, Kleiner R, Moura LIF, Zupančič E, Viana AS, et al.: Immunization with mannosylated nanovaccines and inhibition of the immune-suppressing microenvironment sensitizes melanoma to immune checkpoint modulators. Nature Nanotechnology 2019, 14:891-901.

86. Kreiter S, Selmi A, Diken M, Koslowski M, Britten CM, Huber C, Türeci Ö, Sahin U: Intranodal Vaccination with Naked Antigen-Encoding RNA Elicits Potent Prophylactic and Therapeutic Antitumoral Immunity. Cancer Research 2010, 70:9031.

87. Sahin U, Derhovanessian E, Miller M, Kloke B-P, Simon P, Löwer M, Bukur V, Tadmor AD, Luxemburger U, Schrörs B, et al.: Personalized RNA mutanome vaccines mobilize poly-specific therapeutic immunity against cancer. Nature 2017, 547:222-226.

88. Liang Y, Lü W, Zhang X, Lü B: Tumor-infiltrating CD8+ and FOXP3+ lymphocytes before and after neoadjuvant chemotherapy in cervical cancer. Diagnostic pathology 2018, 13:93-93.

89. Gao Q, Wang S, Chen X, Cheng S, Zhang Z, Li F, Huang L, Yang Y, Zhou B, Yue D, et al.: Cancer-cell-secreted CXCL11 promoted CD8+ T cells infiltration through docetaxel-induced-release of HMGB1 in NSCLC. Journal for ImmunoTherapy of Cancer 2019, 7:42.

90. Opzoomer JW, Sosnowska D, Anstee JE, Spicer JF, Arnold JN: Cytotoxic Chemotherapy as an Immune Stimulus: A Molecular Perspective on Turning Up the Immunological Heat on Cancer. Frontiers in immunology 2019, 10:1654-1654.

91. Bauer C, Sterzik A, Bauernfeind F, Duewell P, Conrad C, Kiefl R, Endres S, Eigler A, Schnurr M, Dauer M: Concomitant gemcitabine therapy negatively affects DC vaccine-induced CD8+ T-cell and B-cell responses but improves clinical efficacy in a murine pancreatic carcinoma model. Cancer Immunology, Immunotherapy 2014, 63:321-333.

92. Petrizzo A, Mauriello A, Luciano A, Rea D, Barbieri A, Arra C, Maiolino P, Tornesello M, Gigantino V, Botti G, et al.: Inhibition of tumor growth by cancer vaccine combined with metronomic chemotherapy and anti-PD-1 in a pre-clinical setting. Oncotarget; Vol 9, No 3 2017.

93. Shah NJ, Najibi AJ, Shih T-Y, Mao AS, Sharda A, Scadden DT, Mooney DJ: A biomaterial-based vaccine eliciting durable tumour-specific responses against acute myeloid leukaemia. Nature Biomedical Engineering 2020, 4:40-51.

**Describes developent of alginate-based cancer vaccine against murine AML.

94. Zuber J, Radtke I, Pardee T, Zhao Z, Rappaport A, Luo W, McCurrach M, Yang M-M, Dolan M, Kogan S, et al.: Mouse models of human AML accurately predict chemotherapy response. Genes & development 2009, 23:877-889.

95. Moynihan KD, Opel CF, Szeto GL, Tzeng A, Zhu EF, Engreitz JM, Williams RT, Rakhra K, Zhang MH, Rothschilds AM: Eradication of large established tumors in mice by combination immunotherapy that engages innate and adaptive immune responses. Nature medicine 2016, 22:1402.

96. Liu H, Moynihan KD, Zheng Y, Szeto GL, Li AV, Huang B, Van Egeren DS, Park C, Irvine DJ: Structure-based programming of lymph-node targeting in molecular vaccines. Nature 2014, 507:519-522.

97. Ott PA, Hu Z, Keskin DB, Shukla SA, Sun J, Bozym DJ, Zhang W, Luoma A, Giobbie-Hurder A, Peter L, et al.: An immunogenic personal neoantigen vaccine for patients with melanoma. Nature 2017, 547:217-221.

98. Grenier JM, Yeung ST, Khanna KM: Combination Immunotherapy: Taking Cancer Vaccines to the Next Level. Front Immunol 2018, 9:610.

99. Romero P, Banchereau J, Bhardwaj N, Cockett M, Disis ML, Dranoff G, Gilboa E, Hammond SA, Hershberg R, Korman AJ, et al.: The Human Vaccines Project: A roadmap for cancer vaccine development. Sci Transl Med 2016, 8:334ps339.

100. Chen G, Emens LA: Chemoimmunotherapy: reengineering tumor immunity. Cancer Immunol Immunother 2013, 62:203-216.

101. Wong KK, Li WA, Mooney DJ, Dranoff G: Advances in therapeutic cancer vaccines. In Advances in immunology. Edited by: Elsevier; 2016:191-249. vol 130.]

102. Schreiber TH, Raez L, Rosenblatt JD, Podack ER: Tumor immunogenicity and responsiveness to cancer vaccine therapy: the state of the art. Semin Immunol 2010, 22:105-112.

103. Bookstaver ML, Tsai SJ, Bromberg JS, Jewell CM: Improving vaccine and immunotherapy design using biomaterials. Trends in immunology 2018, 39:135-150.

104. Galon J, Bruni D: Approaches to treat immune hot, altered and cold tumours with combination immunotherapies. Nature Reviews Drug Discovery 2019, 18:197-218.

CHAPTER 4

BIODEGRADABLE SCAFFOLDS FOR ENHANCING VACCINE EFFICACY

4.0 Abstract

Sustained release of vaccine components is a potential method to boost efficacy compared to traditional bolus injection. Here, we show that a biodegradable hyaluronic acid (HA)-scaffold, termed HA cryogel, mediates sustained antigen and adjuvant release in vivo leading to a durable immune response. Sustained release of vaccines components from HA cryogels was assessed and a formulation which enhanced the immune response while minimizing the inflammation associated with the foreign body response was identified, termed CpG-OVA-HAC2. Dose escalation studies with CpG-OVA-HAC2 demonstrated that both the antibody and T cell responses were dose-dependent and strongly dependent on competency of neutrophils to perform oxidative burst. In immunodeficient post-hematopoietic stem cell transplanted mice, immunization with CpG-OVA-HAC2 elicited a strong antibody response, three orders of magnitude higher than dose-matched bolus injection. In a melanoma model, CpG-OVA-HAC2 induced dose-responsive prophylactic protection, slowing the tumor growth rate and enhancing overall survival. Upon rechallenge, none of the mice developed new tumors suggesting the development of robust immunological memory and long-lasting protection against repeat infections. CpG-OVA-HAC2 also enhanced survival in mice with established tumors. The results from this work support the potential for CpG-OVA-HAC2 to enhance vaccine delivery.

4.0.1 Translational Impact Statement

Biomaterials have been shown to be effective at mediating potent immune responses. While sustained delivery is desirable to achieve a durable immune response, the biomaterial components may induce a foreign body response that could limit clinical utility. Here, we show that a biodegradable hyaluronic acid-based vaccine mediates strong cellular and humoral immunity with a well-tolerated foreign body response. The results support the potential of hyaluronic acid-based scaffolds in immunotherapy.

4.1 Introduction

Biomaterial-based vaccines have been used to potentially address challenges with conventional bolus vaccination strategies. In particular, biomaterials focused on sustained release of vaccine components antigen and adjuvant have been demonstrated to induce a more potent, durable protective immune response compared to bolus vaccination[1–8]. These studies have strongly supported a key role of sustained release of vaccine components in enhancing the immune response. While effective at inducing an immune response, the formulation itself could include components that could result in a persistent foreign body response (FBR), such as those that use long-lasting polymers[2,9,10], that could be limiting in clinical settings[9,11]. On the other hand, a degradable biomaterial-based vaccine which maximizes activation of the adaptive immune responses while avoiding a long-lasting FBR could be a potential alternative.

Hyaluronic acid (HA) is a polysaccharide-based polymer that is abundant in tissues including skin, cartilage, and synovial fluid. It has been widely studied in biomedical applications including drug delivery as HA can be modified to form a matrix to encapsulate drugs, such as growth factors and chemotherapeutic agents, and release them in a

sustained manner via controlled degradation[12]. We have previously demonstrated that the degradation of HA can be immune-responsive, mediated by oxidative burst of neutrophils[12], and is also processed by endogenous hyaluronidases[13,14] (HYAL). The degradation generates low molecular weight HA fragments which have been shown to activate toll-like receptors (TLRs) and act as adjuvants in vaccine formulations[4–6].

Here, we hypothesized that a HA-based vaccine formulation would enhance immune cell activation and sustain release of encapsulated vaccine components to generate a durable protective immune response. We had previously developed a macroporous injectable HA hydrogel, termed HA cryogel, made with bioorthogonal crosslinking chemistry[12]. HA cryogels mediated sustained release of protein therapeutics to enhance innate immune cell regeneration[12]. In this work, we extend our previous findings to further develop HA cryogels as depots for sustained release of vaccine components. After evaluating cryogel formulations generated from commercially sourced HA by immunophenotypic and histological assessments, we selected low endotoxin HA, termed HAC2 for evaluation with encapsulated model antigen OVA, adjuvants CpG-ODN 1826 (CpG) and granulocyte macrophage colony stimulating factor (GM-CSF). Both CpG and GM-CSF comparably enhanced the response to the vaccine, but GM-CSF increased inflammation and the FBR at the injection site. We selected CpG-loaded OVA-HAC2 (CpG-OVA-HAC2) for dose ranging studies. The intensity of the adaptive immune response was dose dependent on CpG-OVA-HAC2 and significantly delayed in settings of neutrophil dysfunction. In post-hematopoietic stem cell transplant (HSCT) mice, CpG-OVA-HAC2 enhanced antibody induction three orders of magnitude greater than dose-matched bolus vaccination. In a

B16-OVA melanoma mouse model, prophylactic and therapeutic administration of CpG-OVA-HAC2 slowed the tumor growth rate and enhanced overall survival.

4.2 Results

4.2.1 Synthesis and characterization of HA cryogels

HA cryogels are formulated by first conjugating either tetrazine (Tz) amine or norbornene (Nb) methylamine to HA to form tetrazine-functionalized HA (HA-Tz) and norbornene-functionalized HA (HA-Nb). Vaccine components were solubilized with the polymer solution prior to mixing and overnight incubation at -20^{o}C to form HA cryogel vaccines (**Fig. 4.1a**). HA was initially sourced from two commercial suppliers and resulting HA cryogels are referred to as HAC1 and HAC2 for HA sourced from supplier 1 and 2 respectively. For confocal imaging and in vivo degradation tracking, HA-Nb was reacted with Tz-Cy5 to form Cy5-labeled HA-Nb (Cy5-HA-Nb) which was mixed with HA-Tz to form Cy5-labeled HA cryogels, referred to as HAC1:Cy5 and HAC2:Cy5 (**Supplementary Fig. 4.1a**). To visualize pores and assess pore interconnectedness, HAC1:Cy5 and HAC2:Cy5 were incubated with fluorescein isothiocyanate (FITC)-labeled 10μm diameter melamine resin particles and imaged using confocal microscopy. FITC-particles were co-localized with Cy5-labled HA polymer to the confocal depth limit for HAC1:Cy5 and HAC2:Cy5 (**Fig. 4.1b**). Next, we lyophilized HA cryogels and measured surface porosity using scanning electron microscopy (SEM) (**Fig. 4.1c**). Average pore diameter for HAC1 and HAC2 were found to be 59.5 ± 19.4 and 53.8 ± 15.8 μm, respectively (**Supplementary Fig. 4.1b**).

To test the magnitude of an adaptive immune response to the HA cryogel alone, 100 μg of OVA was encapsulated in HAC1 and HAC2 (OVA-HAC1 and OVA-HAC2) and in vitro

degradation kinetics of OVA-HAC1 and OVA-HAC2 were assessed by incubating cryogels in hyaluronidase 2 (HYAL2) solution. The degradation profiles of of OVA-HAC1 and OVA-HAC2 were comparable, with most of the degradation occurring within the first week and full degradation occurring over the course of three weeks (**Fig. 4.1d**). To characterize in vivo degradation profile of OVA-encapsulated HAC1:Cy5 (OVA-HAC1:Cy5) and OVA-encapsulated HAC2:Cy5 (OVA-HAC2:Cy5) we utilized in vivo imaging system (IVIS). A single OVA-HAC1:Cy5 or OVA-HAC2:Cy5 was injected subcutaneously in the hind flank of C57Bl/6J (B6) mice. Strikingly, OVA-HAC1:Cy5 degraded over the course of 5 weeks whereas OVA-HAC2:Cy5 degraded over the course of 3 months (**Fig. 4.1e, f**). The degradation half-life of OVA-HAC1:Cy5 and OVA-HAC2:Cy5, as determined by the time to achieve a 50% reduction in fluorescence intensity was 20 ± 2 and 54 ± 5 days, respectively (**Supplementary Fig. 4.1c**).

We next sought to quantify the effect of degradation on OVA release. In vitro release assays for OVA-HAC1 and OVA-HAC2 were conducted with or without HYAL2 solution in phosphate buffered saline (PBS). In HYAL2 solution, 88.8 ± 6.6% and 86.3 ± 6.8% of OVA released from OVA-HAC1 and OVA-HAC2, respectively, over the first day with the remaining OVA released throughout the course of the study until the gels were fully degraded (**Fig. 4.1g**). In PBS, 22.2 ± 2.8% and 23.0 ± 0.7% of OVA burst release from OVA-HAC1 and OVA-HAC2, respectively, within the first day with minimal release over the rest of the study (**Fig. 4.1g**). The encapsulation efficiency of OVA, based on in vitro release, was 77.8% for OVA-HAC1 and 77.0% for OVA-HAC2. To determine in vivo OVA release kinetics, OVA was functionalized with Cy5 (OVA:Cy5) prior to encapsulation within HAC1 (OVA:Cy5-HAC1) and HAC2 (OVA:Cy5-HAC2) and measured using IVIS

Release was quantified by measuring the attenuation of the fluorescence signal relative to the initial measurement. The release of OVA:Cy5 from HAC1 and HAC2 was sustained over multiple weeks with accelerated OVA:Cy5 release from HAC1 as compared to HAC2 (**Fig. 4.1h, i**).

4.2.2 HAC1 and HAC2 are infiltrated with a distinct innate immune cell profile

As endotoxin content of polymers is known to influence the immune response, the endotoxin content of HAC1 and HAC2 was quantified by measuring lipopolysaccharide (LPS) content. Endotoxin content was measured to be 7.3 x 10^{-3} EU and 6.7 x 10^{-4} EU for HAC1 and HAC2 respectively (**Table 4.1**). Innate immune cells infiltrating OVA-HAC1 and OVA-HAC2 were assessed 7-days post-injection using flow cytometry (**Fig. 4.2a, b; Supplementary Fig. 4.2a**). The viability of infiltrating cells (Aqua Zombie negative) was consistently greater than 95% in OVA-HAC1 and OVA-HAC2 (**Supplementary Fig. 4.2b**). Total $CD45^+CD11b^+$ (myeloid) cells were 2.4-fold higher in OVA-HAC1 compared to OVA-HAC2 (**Fig. 4.2c**). Notably, $CD45^+CD11b^+Ly6G^+$ (neutrophil) cells constituted most of the cellular infiltrates in OVA-HAC1 but were nearly absent in OVA-HAC2 (**Fig. 4.2d, e**). Conversely, OVA-HAC1 had minimal $CD45^+CD11b^+Ly6G^-CD115^+$ (monocyte) and $CD45^+CD11b^+Ly6G^-CD115^-F4/80^+$ (macrophage) cells whereas monocytes and macrophages constituted a majority of cellular infiltrates in OVA-HAC2 (**Fig. 4.2d, f, g**). $CD45^+CD11b^+Ly6G^-CD115^-F4/80^-CD11c^+$ (dendritic) cells (DCs) were sparsely found in both OVA-HAC1 and OVA-HAC2 (less than 3% of total myeloid cells), but on average higher in OVA-HAC2 (**Fig. 4.2d, h**).

Cryogels were explanted from mice 7-days post-injection for histomorphometric analysis using hematoxylin and eosin (H&E). Both OVA-HAC1 and OVA-HAC2 were infiltrated and

encased in a fibrotic capsule (**Fig. 4.2i**). Cellularity and capsule thickness were increased in OVA-HAC1 (**Fig. 4.2j, k**). In a separate cohort of mice, we measured the host immune response to OVA-HAC1 and OVA-HAC2. Mice received a single subcutaneous injection of OVA-HAC1 or OVA-HAC2 each in a prime and boost setting 11-days apart and were bled at pre-determined timepoints post-prime. OVA-HAC1 induced higher anti-OVA IgG1 antibody titers compared to OVA-HAC2 (**Fig. 4.2l**).

Next, we sought to determine whether the aforementioned differences in innate immune cell infiltration and anti-OVA antibody titers might be due to differences in endotoxin content. We added LPS, the major constituent of endotoxin, in HA-Tz and Cy5-HA-Nb from to generate OVA-HAC2 with endotoxin content of 5.2×10^{-3} EU (low-LPS) and 5.2×10^{-2} EU (high-LPS), corresponding to approximately 80% and 800% of OVA-HAC1 endotoxin content (**Supplementary Table 4.1**). Innate immune cell infiltration into OVA-HAC2 with LPS was assessed 7-days post-injection and compared to OVA-HAC2 without added LPS. Inclusion of LPS had no effect on total myeloid, neutrophil, monocyte, macrophage, or DC infiltration in OVA-HAC2 (**Supplementary Fig. 4.2c-h**). Mice were administered OVA-HAC2, low-LPS OVA-HAC2, and high-LPS OVA-HAC2 in a prime and boost setting 11-days apart and were bled at pre-determined timepoints. No significant differences were quantified with anti-OVA IgG1 antibody titers between any of the test groups (**Supplementary Fig. 4.2i**). Based on these results, we selected HAC2 for further assessment.

4.2.3 Encapsulation of adjuvants enhances HA cryogel-based vaccine efficacy and alters foreign body response

To assess the effect of including an adjuvant in OVA-HAC2, we selected CpG-ODN 1826 (CpG, 100 µg), a TLR9 agonist[15–17], and granulocyte-colony stimulating factor (GM-CSF,

1 μg), a DC maturation factor[18–21] and alternative adjuvant[22–24]. GM-CSF and CpG were encapsulated in OVA-HAC2 (GMCSF-CpG-OVA-HAC2) and in vitro release studies were conducted with or without HYAL2 solution in PBS. In HYAL2 solution, 88.7 ± 4.5% and 97.1 ± 0.4% of CpG and GM-CSF, respectively, released from OVA-HAC2 over the first day with the remaining release throughout the course of the study with cryogel degradation (**Supplementary Fig. 4.3a, b**). In PBS, 53.8 ± 7.1% and 15.8 ± 3.6% of CpG and GM-CSF, respectively, burst release from the cryogels over the course of the first day with minimal release over the rest of the study (**Supplementary Fig. 4.3a, b**). From the release in PBS, encapsulation efficiency was calculated to be 46.2% and 84.2% for CpG and GM-CSF, respectively.

Three OVA-HAC2 adjuvanted formulations were made by inclusion of either CpG (CpG-OVA-HAC2), GM-CSF (GMCSF-OVA-HAC2), or both (GMCSF-CpG-OVA-HAC2) and degradation kinetics were assessed and compared to OVA-HAC2:Cy5 (**Fig. 4.3a**). All components were tested for endotoxin content (**Supplementary Table 4.2**). Mice were administered a prime and boost with adjuvanted OVA-HAC2:Cy5 formulations or OVA-HAC2:Cy5 11-days apart. Degradation profile was comparable between all groups and cryogels were fully degraded 10-weeks post-injection (**Fig. 4.3b-e**).

Innate immune cell infiltrates in the HAC2 and OVA-HAC2 vaccine formulations were compared 10-days and 21-days after injection (**Fig. 4.4a**). The viability of infiltrating cells was consistently greater than 93% in al groups 10-days after injection (**Supplementary Fig. 4.4a**). In cryogels removed 10-days after injection, total myeloid cell infiltration was similar between HAC2, OVA-HAC2, and all adjuvanted OVA-HAC2 formulations (**Fig. 4.4b**). The fraction of $Ly6G^+$ neutrophils was enhanced in both GMCSF-OVA-HAC2 and

GMCSF-CpG-OVA-HAC2 and constituted the majority of infiltrating cells in GMCSF-CpG-OVA-HAC2 (**Fig. 4.4c**). Neutrophil cell counts were 14.5- and 83.2-fold higher in GMCSF-OVA-HAC2 and GMCSF-CpG-OVA-HAC2 respectively, compared to OVA-HAC2 (**Fig. 4.4d**). On the other hand, neutrophil count in CpG-OVA-HAC2 and OVA-HAC2 was similar (**Fig. 4.4d**). Monocytes were lower in all adjuvanted OVA-HAC2 formulations compared to OVA-HAC2. However, GMCSF-CpG-OVA-HAC2 had the lowest number of monocytes (**Fig. 4.4e**). Macrophage infiltration was modestly lower in GMCSF-CpG-OVA-HAC2, but similar in the other formulations (**Fig. 4.4f**). DC infiltration was similar between the test groups and constituted less than 3% of total cellular infiltrates in all formulations (**Fig. 4.4c, g**). In the cryogel formulations removed 21-days after injection, live cell percentages were greater than 75% on average in all groups. Myeloid cell infiltration and the constituent cells of the infiltrates were similar between groups (**Supplementary Fig. 4.4b-h**).

HAC2, OVA-HAC2, and adjuvanted OVA-HAC2 formulations were administered in mice and removed 10-days post injection for histomorphometry-based H&E staining. All formulations were infiltrated with cells and encased in a fibrotic capsule (**Fig. 4.4h**). The cellularity was greater the OVA-HAC2 vaccine formulations which included GM-CSF as a constituent (**Fig. 4.4i**). However, only mice which received GMCSF-CpG-OVA-HAC2 had increased capsule thickness (**Fig. 4.4j**).

Initial immunization studies were conducted without HA in which mice received a single prime and boost bolus subcutaneous injection of vaccine components 11-days apart. Mice received either (i) OVA only, (ii) OVA + GM-CSF, (iii) OVA + CpG, or (iv) OVA + GM-CSF + CpG and periodically bled post-prime to assess anti-OVA IgG1 antibody

concentrations (**Supplementary Fig. 4.5a**). OVA + GM-CSF and OVA + GM-CSF + CpG enhanced antibody titers compared to OVA only (**Supplementary Fig. 4.5b**). OVA + CpG generated a minimal antibody response, comparable to mice which received OVA only (**Supplementary Fig. 4.5b**).

Next, the aforementioned OVA-HAC2 vaccine formulations were administered to mice in a prime and boost 11-days apart. Assessments of anti-OVA IgG1 antibody titers showed a significant difference between OVA-HAC2 and all other adjuvanted formulations (**Fig. 4.4k**). There was no difference in antibody titers between any adjuvanted OVA-HAC2 formulations (**Fig. 4.4k**). The same cohorts of mice were used to measure degradation of the OVA-HAC2:Cy5 formulations using IVIS. In a separate study, mice were administered prime and boost adjuvanted OVA-HAC2 and OVA-HAC2 only and sacrificed 3-weeks post prime to assess $CD45^{+}B220^{-}CD8^{+}SIINFEKL^{+}$ cells (OVA-specific cytotoxic T cell) in both the draining axillary lymph nodes (LNs) and spleen (**Supplementary Fig. 4.5c, d**). The test groups and unvaccinated mice had comparable antigen-specific cytotoxic T cells in the lymph node and spleens (**Supplementary Fig. 4.5e, f**).

We concluded that all adjuvanted OVA-HAC2 vaccine formulations comparably enhanced antigen-specific adaptive immune response. However, formulations that included GM-CSF were associated with an exacerbated the foreign body response. Therefore, we selected CpG-OVA-HAC2 for further studies.

4.2.4 CpG-OVA-HAC2 induces a dose dependent adaptive immune response

We evaluated the release of CpG from CpG-OVA-HAC2 in vivo. Cy5-labeled CpG (Cy5:CpG) was encapsulated within OVA-HAC2 to from CpG:Cy5-OVA-HAC2. Release was assessed using IVIS. CpG:Cy5 release was sustained over a period of three weeks

with 85.0 ± 3.1% of release occurring within the first week (**Fig. 4.5a**). The effect of vaccine dose escalation on the adaptive immune response was assessed by increasing the number of CpG-OVA-HAC2 administered. Mice received either a single dose prime, two-dose prime, single dose prime and boost, or two-dose prime and boost. Assessment of anti-OVA IgG1 antibody titers showed that a single prime vaccination induced significantly lower antibody titers than mice which received higher doses (**Fig. 4.5b**). Notably, there was no difference in anti-OVA IgG1 antibody titers in mice which received any of the other higher vaccine doses (**Fig. 4.5b**). $CD45^{+}B220^{-}CD8^{+}SIINFEKL^{+}$ cells (OVA-specific cytotoxic T cells) were assessed 3-weeks post-prime in the draining axillary lymph nodes (LNs) (**Fig. 4.5c**). Only mice which received two CpG-OVA-HAC2 as both a prime and boost had a significantly elevated percentage of OVA-specific cytotoxic T cells in axillary LN compared to other groups (**Fig. 4.5d**). There was no difference in OVA-specific cytotoxic T cell percentage in any of the groups in the spleen 3-weeks post prime (**Supplementary Fig 4.6**).

To better study the effect of polymer degradation and the development of an adaptive immune response, we utilized $gp91^{phox-}$ mice which have neutrophils that lack the ability to perform oxidative burst[12,25,26]. We have also previously demonstrated that HA cryogel degradation in this model is impaired[12]. Two CpG-OVA-HAC2:Cy5 were administered in $gp91^{phox-}$ or B6 mice as a prime and boost 11-days apart. IVIS measurements on mice showed minimal degradation of CpG-OVA-HAC2:Cy5 in $gp91^{phox-}$ mice and complete degradation in B6 mice (**Fig. 4.5e**). The same cohorts of mice were bled at pre-determined timepoints for assessment of anti-OVA IgG1 antibody titers. There was a

significant delay in the development of anti-OVA IgG1 antibodies in gp91^{phox-} mice with none having detectable anti-OVA IgG1 antibody titers two-weeks post prime (**Fig. 4.5f**). To demonstrate the utility of CpG-OVA-HAC2 in mediating enhanced immunity, we measured the effect of treating immunodeficient mice post autologous hematopoietic stem cell transplant (HSCT) in B6 mice. Mice received lethal radiation followed by HSCT consisting of both 15M whole bone marrow cells and 10M splenocytes 2-days later (**Fig. 4.5g**). Two CpG-OVA-HAC2:Cy5 or bolus CpG + OVA were administered to mice in a prime and boost 11-days apart and bled at pre-determined timepoints (**Fig. 4.5g**). Mice that received CpG-OVA-HAC2 had measurable anti-OVA IgG1 antibody titers whereas there were no detectable anti-OVA IgG1 antibodies in mice which received bolus vaccination (**Fig. 4.5h**). The immunization study was repeated in the context of post-allogenic HSCT, with BALB/cJ donor mice and B6 recipients. All the mice in this study succumbed to graft-versus-host disease-like pathology within 5-weeks post-HSCT. Blood was collected once at 2-weeks post prime, 4-weeks post-HSCT. There were no detectable anti-OVA IgG1 antibodies in either group.

4.2.5 CpG-OVA-HAC2 mediates prophylactic protection in a B16-OVA melanoma mouse model

We sought to assess whether CpG-OVA-HAC2 enhanced prophylactic protection in a mouse melanoma model. Mice were administered either one or two CpG-OVA-HAC2 or two bolus CpG + OVA injections in a prime and boost setting. Mice received one hundred thousand B16-OVA cells administered subcutaneously 3-weeks post prime or in unvaccinated mice and tumor growth rate and survival were compared (**Fig. 4.6a**). In all unvaccinated mice, tumors were visible two-weeks post tumor inoculation with rapid tumor growth thereafter (**Fig 4.6b, c**). In mice that received two bolus CpG + OVA

injections, tumor growth was delayed and were visible in all mice three-weeks post tumor inoculation (**Fig. 4.6b**). In contrast, only 60% of the mice that received a single CpG-OVA-HAC2 as prime and boost had visible tumors. 40% of the mice that received two CpG-OVA-HAC2 as prime and boost each had visible tumors four-weeks post tumor inoculation (**Fig. 4.6b**). In all vaccinated mice, tumor growth rate was significantly reduced and increased the mean survival time (**Fig. 4.6c**). Overall survival was dose responsive to CpG-OVA-HAC2. Mice that received two CpG-OVA-HAC2 as a prime and boost had the highest overall survival of 60% (**Fig. 4.6d**). Mice that received a single CpG-OVA-HAC2 had an overall survival of 40% whereas mice receiving bolus vaccination and unvaccinated mice all succumb to B16-OVA melanoma (**Fig. 4.6d**). Vaccinated mice were bled six-weeks post prime, three-weeks post tumor inoculation, and mice which received bolus CpG-OVA-HAC2 had lower anti-OVA IgG1 antibody titers than mice which received CpG-OVA-HAC2 (**Fig. 4.6e**). Mice which survived B16-OVA melanoma challenge were re-challenged with 100K B16-OVA cells three-months post initial inoculation. All mice survived rechallenge without visible tumors for at least 40 days post re-challenge. Next, we assessed whether CpG-OVA-HAC2 would provide therapeutic protection against murine melanoma. Mice were administered one hundred thousand B16-OVA cells administered subcutaneously 3-days prior to one or two CpG-OVA-HAC2 in a prime and boost setting (**Fig. 4.6f**). CpG-OVA-HAC2 administered therapeutically slowed tumor growth and prolonged survival as compared to unvaccinated mice (**Fig. 4.6g, h**). Mice that received a single CpG-OVA-HAC2 as a prime and boost survived 45.9 ± 13.8 days and mice that received two CpG-OVA-HAC2 as a prime and boost survived 45.5 ± 12.0

days post-tumor challenge. In contrast, unvaccinated mice only survived 28.5 ± 5.3 days post-tumor challenge. (**Fig. 4.6h**).

4.3 Discussion

Here, we demonstrate that a hyaluronic acid cryogel-based biodegradable vaccine mediates sustained release of vaccine components, enhances antigen-specific adaptive immunity in healthy and immunodeficient mice, and provides protection against B16-OVA melanoma in a vaccine dose-dependent manner. The source of material and selection of adjuvants had a significant impact on the infiltrating innate immune cell subsets that constitute the FBR. We demonstrate that CpG-OVA-HAC2 formulation enhances anti-OVA adaptive immune response without significantly altering the FBR and that the adaptive immune response was enhanced with escalating vaccine doses. The effect of high-dose Cpg-OVA-HAC2 was studied in immune deficient models. In gp91^{-phox} mice, the degradation of CpG-OVA-HAC2 was delayed which resulted in slowed activation of the adaptive immunity. In post-HSCT mice, adaptive immune activation with CpG-OVA-HAC2 was greatly enhanced as compared to bolus CpG+OVA vaccination, highlighting the enhancement in adaptive immune response even in immunodeficient contexts. Lastly, enhancement in immune response was assessed in both prophylactic and therapeutic vaccine studies involving B16-OVA melanoma, in which the CpG-OVA-HAC2 slowed tumor growth and enhanced survival relative to unvaccinated mice and mice receiving bolus vaccination.

HA was selected as the polymer as it is ubiquitous in the ECM and has a long history of use as a biodegradable material to effectively facilitate sustained drug delivery. As an

ECM component, HA provides cues to regulate inflammation and tissue repair[27]. In the context of tissue damage or injury, HA undergoes degradation resulting in the production of low molecular weight fragments[28,29]. These fragments are known to activate innate immune cells, particularly monocytes, macrophages, and DCs, through the activation of TLR2 and TLR4[4,29–32]. The downstream signaling of TLR activation results in secretion of TNF-α, IL-12 and IL-1β which promote inflammation[33,34]. Additionally, HA fragments have been shown to induce expression of matrix metalloproteinases, which degrade ECM components and facilitate tissue remodeling[35,36]. Thus, the use of HA in biomaterials-based vaccine not only provides sustained release of vaccine components but also potentially offers additional cues to regulate inflammation. The use of HA is further supported by other pre-clinical vaccine studies which have utilized HA as an adjuvant in their vaccine formulations[4–6]. Consistent with prior work, our results showing that HA cryogel encapsulating OVA alone elicits anti-OVA IgG1 antibody titers without an additional adjuvant[4].

Seeking to assess the effect of HA from different sources, we tested the effect of formulating HA cryogels from two commercial vendors. HA cryogels from both vendors had comparable pore size and morphology, in vitro degradation kinetics, and in vitro OVA release kinetics. There were differences in endotoxin levels, as determined by measuring LPS content, with HAC1 having 10.8-fold higher endotoxin levels than HAC2. However, the endotoxin levels of HAC1 and HAC2 were well below FDA guidelines for implantable devices[37,38]. When cryogels were administered, OVA-HAC1 induced higher anti-OVA IgG1titers than OVA-HAC2 but was associated with a neutrophil dominated FBR with enhanced capsule thickness. However, when we added external LPS into HAC2 such

that the resulting endotoxin levels were ~80% and 800% of those in HAC1, there were no significant differences in anti-OVA IgG1 antibody titers and FBR when compared to OVA-HAC2 without added LPS. These results suggest that increased LPS content alone in OVA-HAC1 cannot explain the differences in anti-OVA IgG1 antibody titers and FBR. These results suggest the potential of other components that constitute endotoxin which can also act as TLR agonists[39–41].

Inspired by previously reported biomaterial-based vaccine formulations, we tested the effect of encapsulating the adjuvants CpG and GM-CSF[1,2,9,42]. CpG is a clinically approved TLR9 agonist and has also been extensively studied for use in other vaccine formulations[43,44]. GM-CSF is a clinically approved agent for bone marrow recovery and has also been studied as a potential adjuvant in vaccine formulations [45]. In contrast to other common TLR agonists such as Monophosphoryl-Lipid A (MPLA) or squalene, CpG and GM-CSF are water soluble and amenable for encapsulation in HA cryogels. Avoiding the need for organic solvents, solubilizers and stabilizers reduces interference with the crosslinking process. If needed, encapsulating multiple TLR agonists, for example CpG and poly(I:C), may represent a strategy for improving immunogenicity of the HAC2-based vaccine formulation[46,47].

In our studies, inclusion of either GM-CSF or CpG into OVA-HAC2 enhanced anti-OVA IgG1 antibody titers comparably and inclusion of both did not further enhance anti-OVA IgG1 antibody titers. When we assessed innate immune cell infiltration in the various vaccine formulations, inclusion of GM-CSF lead to enhanced neutrophil infiltration, consistent with other reports. Supporting these results, analysis of H&E stained HAC2 vaccine formulations showed an increase in cellularity with formulations including GM-

CSF. As the inclusion of GM-CSF in the vaccine increased inflammation at the injection site and did not further improve the immune response, CpG-OVA-HAC2 was chosen for further evaluation.

Our previous finding of the importance of degradation in mediating release of encapsulated components[12] was further validated in the present work. In vitro release in PBS and HYAL2 solutions showed an initial burst release followed by a period of sustained release. Burst release in PBS is expected and is observed in nearly all cryogel-based drug delivery systems. The burst release in HYAL2 solution can be attributed to rapid initial degradation of the HA cryogels, during which approximately 50% of gel degraded after first 9-hours for HAC1:Cy5 and HAC2:Cy5, respectively. In vivo, the slower rate of degradation of HA cryogels corresponded to more sustained release of encapsulated vaccine components.

CpG-OVA-HAC2 was administered in immunodeficient mice to assess the mechanism and potential enhancement of vaccine efficacy. Consistent with our previous work, the degradation of HA cryogels in gp91^{phox-} mice was impaired[12]. Moreover, the induction of anti-OVA IgG1 antibody titers in the gp91^{phox-} were significantly delayed, supporting the need for release of vaccine components. Post-HSCT Mice which received CpG-OVA-HAC2 injections developed robust anti-OVA IgG1 antibody titers starting two-weeks post-prime whereas mice which received bolus vaccination only developed failed to develop a detectable adaptive immune response until 6-weeks post-prime. These results support the utility of CpG-OVA-HAC2 in generating a robust adaptive immune response in immunodeficient mice.

Although two dose prime and boost was more effective at inducing a greater cellular

and humoral immune response than a single dose prime and boost, the enhancement did not significantly change the efficacy of prophylactic prevention and therapeutic treatment of tumors between the two groups, as measured by overall survival. This observation might reflect a limitation in the effectiveness of CpG-OVA-HAC2 alone as a monotherapy and is consistent with past reports of other cancer vaccines [7,48–50]. To potentially improve cancer vaccine efficacy, particularly in established tumors, combining standard-of-care therapy, for example chemotherapy or checkpoint inhibitors, with cancer vaccines has proven to be an effective strategy to prolong survival compared to either therapy alone[2,51,52]. The distinct mechanisms by which these agents operate might leverage both pre-existing tumor-specific immune cells and generate new anti-tumor immunity for a potentially stronger and more durable response.

The results from this study show that by sustaining release of vaccine components, CpG-OVA-HAC2 induce a more potent adaptive immune response compared to conventional bolus vaccination. These results are consistent with those from other biodegradable injectable scaffold systems. This includes an in situ crosslinked polymer-nanoparticle hydrogel-based vaccine platform which shows sustained OVA release and enhanced anti-OVA adaptive immune response relative to bolus control[1]. A potential advantage of HA cryogel-based vaccines is that the gels are pre-formed and injected individually, allowing for more control of dosing and less inter-operator variability. Our results are also consistent with another approach using nanocellulose hydrogels, which shows sustained release of OVA provides stronger protection against murine lymphoma, than bolus vaccination[53]. However, nanocellulose hydrogels are surgically implanted, whereas HA cryogel-based vaccination is administered with a syringe. Similar to other biomaterial-

based vaccines, the HA cryogel-based vaccine allows for incorporating a range of adjuvants and antigens with the advantage of leveraging an established bioorthogonal crosslinking chemistry that reduces the potential for inactivating vaccine components[54,55]. The results support the development of a HAC2-based vaccine for protection against infections or cancers, including in settings of immunodeficiency. However, owing to its xenogeneic origin, OVA can be inherently more immunostimulatory than antigens that might be associated with cancer cells. HAC2-based vaccine formulations could be designed to utilize tumor cell lysate as a source of tumor antigen, precluding the need to identify a specific tumor antigen and potentially allowing for testing the formulation in multiple tumors types[56,57]. Alternatively, HAC2-based subunit vaccines could be developed that contain known tumor antigens such as Trp2 and gp100[58,59]. HAC2-based cancer neoantigen vaccines would likely require optimization with multiple TLR agonists and multiple antigen targets to improve vaccine efficacy and breadth of the adaptive immune response. Further, efficacy of HAC2-based neoantigen vaccines could be assessed in combination with checkpoint inhibitor or chemotherapy[52,60,61]. Taken together, our results demonstrate the development of a degradable, biocompatible vaccination platform which may be leveraged to provide greater protection against infections or cancers, including in settings of immunodeficiency.

4.4 Figures

Figure 4.1| Synthesis and characterization of HA cryogels
(**a**) Schematic depicting HA cryogel vaccine formulation. (**b**) Confocal microscopy images, overhead and side views, depicting hydrated Cy5-conjugated HAC1 (HAC1:Cy5) and HAC2:Cy5 incubated with 10 μm FITC-labeled microparticles. Scale bar = 100 μm. (**c**) Scanning electron microscope (SEM) images of HA cryogels, HAC1 and HAC2. Left scale bar = 2 mm, right scale bar = 300 μm. (**d**) In vitro degradation kinetics of OVA-encapsulated Cy5-labeled HAC1 (OVA-HAC1:Cy5) and HAC2 (OVA-HAC1:Cy5) in hyaluronidase 2 (HYAL2) solution. (**e**) Representative in vivo imaging system (IVIS) fluorescence images of OVA-HAC1:Cy5 and OVA-HAC2:Cy5 degradation. (**f**) Measuring OVA-HAC1:Cy5 and OVA-HAC2:Cy5 degradation in vivo by quantification of total radiant efficiency normalized to initial day 3 timepoint. (**g**) Quantification of in vitro OVA release from OVA-encapsulated HAC1 (OVA-HAC1) and OVA-HAC2 in either phosphate buffered saline or HYAL2 solution. (**h**) Representative IVIS fluorescence images of Cy5-conjugated OVA (OVA:Cy5) encapsulated HAC1 (OVA:Cy5-HAC1) and OVA:Cy5-HAC2. (**i**) Measuring OVA:Cy5 release from HAC1 and HAC2 by quantification of total radiant efficiency normalized to initial 6-hour timepoint. Data in **d, g** represents mean ± s.d. of n=4 cryogels. Data in **f** represents mean ± s.e.m. of n=5 mice. Data in **i** represents mean ± s.e.m. of n=4 mice. Data in **d, f, g, i** compared using two-way ANOVA with Bonferroni's multiple comparison test. In **g** comparison of PBS and HYAL2 release was conducted by pooling measurements for OVA-HAC1 and OVA-HAC2. Figure 1a created using Biorender.

Figure 1

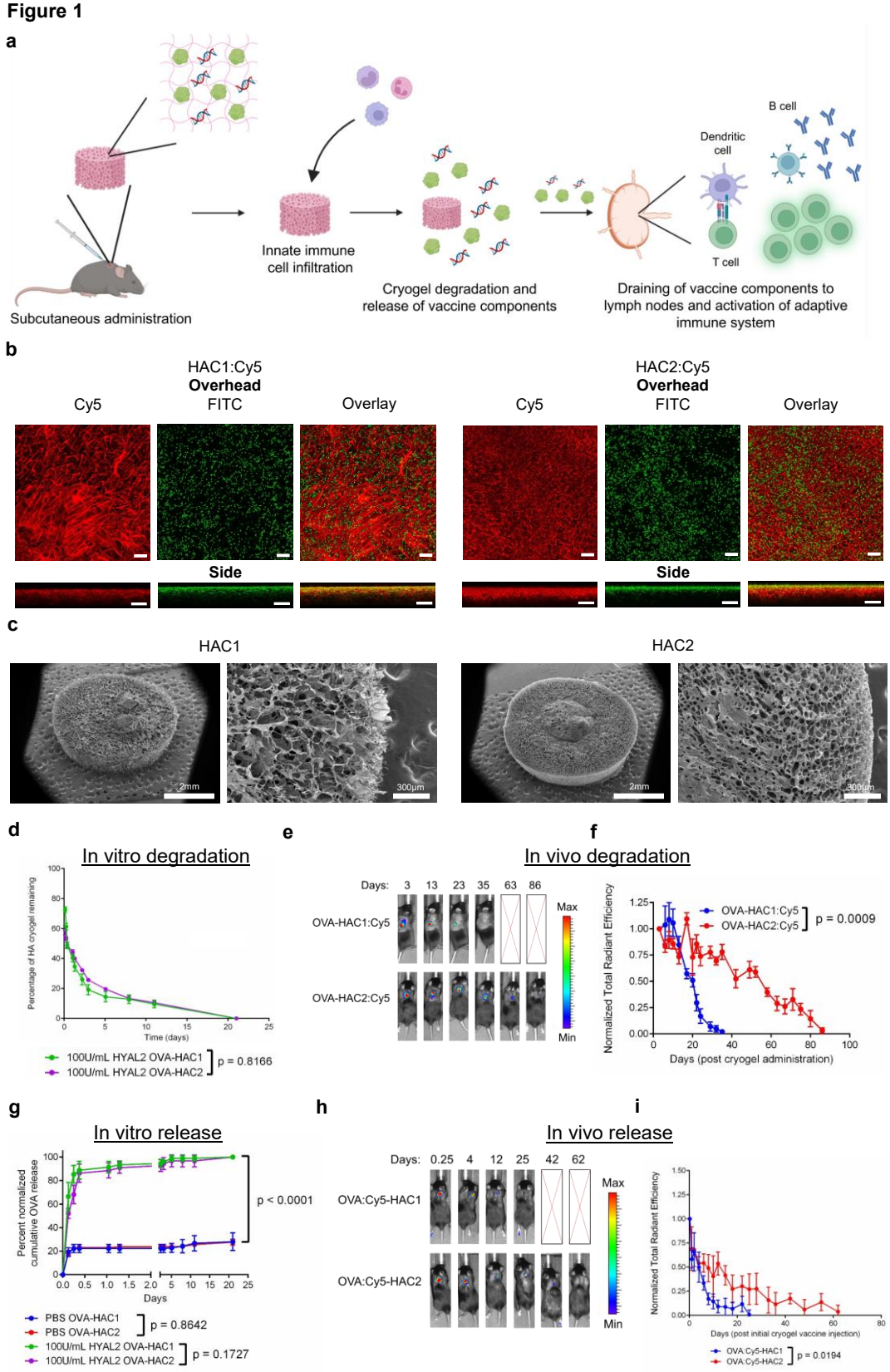
a
Subcutaneous administration
Innate immune cell infiltration
Cryogel degradation and release of vaccine components
Dendritic cell
B cell
T cell
Draining of vaccine components to lymph nodes and activation of adaptive immune system
b
HAC1:Cy5
Overhead
Cy5
FITC
Overlay
Side
HAC2:Cy5
Overhead
Cy5
FITC
Overlay
Side
c
HAC1
HAC2
2mm
300µm
d
In vitro degradation
Percentage of HA cryogel remaining
Time (days)
100U/mL HYAL2 OVA-HAC1
100U/mL HYAL2 OVA-HAC2
p = 0.8166
e
f
In vivo degradation
Days: 3 13 23 35 63 86
OVA-HAC1:Cy5
OVA-HAC2:Cy5
Max
Min
Normalized Total Radiant Efficiency
OVA-HAC1:Cy5
OVA-HAC2:Cy5
p = 0.0009
Days (post cryogel administration)
g
In vitro release
Percent normalized cumulative OVA release
Days
p < 0.0001
PBS OVA-HAC1
PBS OVA-HAC2
p = 0.8642
100U/mL HYAL2 OVA-HAC1
100U/mL HYAL2 OVA-HAC2
p = 0.1727
h
i
In vivo release
Days: 0.25 4 12 25 42 62
OVA:Cy5-HAC1
OVA:Cy5-HAC2
Max
Min
Normalized Total Radiant Efficiency
Days (post initial cryogel vaccine injection)
OVA:Cy5-HAC1
OVA:Cy5-HAC2
p = 0.0194

Figure 4.2| Assessment of innate immune cell response to HAC1 and HAC2
(**a**) Workflow schematic for assessing innate immune cell infiltration in OVA-HAC. (**b**) Representative flow cytometry plots depicting gating strategy to determine cellular identity of $CD45^+CD11b^+Ly6G^+$ (neutrophil), $CD45^+CD11b^+Ly6G^-CD115^+$ (monocyte), $CD45^+CD11b^+Ly6G^-CD115^-F4/80^+$ (macrophage), and $CD45^+CD11b^+Ly6G^-CD115^-F4/80^-CD11c^+$ dendritic cells (DCs). (**c**) Quantification of total $CD45^+CD11b^+$ (myeloid) cells. (**d**) Infiltrating immune cells plotted as a percentage of myeloid cells. **e-h** Quantification of total numbers of (**e**) neutrophils, (**f**) monocytes, (**g**) macrophages, and (**h**) DCs. (**i**) Hematoxylin and eosin (H&E) stained histological sections of explanted OVA-HAC1 and OVA-HAC2 7-days post-injection. Full view scale bar = 800 μm, magnified scale bar = 100 μm. (**j**) Quantification of cellular density in the sections from H&E slides. (**k**) Quantification of fibrotic capsule thickness in the sections from H&E slides. (**l**) Assessment of anti-OVA IgG1 antibody titers in serum of mice which received a single injection of OVA-HAC1 or OVA-HAC2, administered in a prime and boost setting 11 days apart. Data in **c-h** represents mean ± s.d. of n = 9 cryogels. Data in **j** represents mean ± s.d. of n = 4 cryogels. Data in **k** represents mean ± s.d. of n = 12 measurements (4 measurements per cryogel). Data in **l** represents mean ± s.d. of n=5 mice. Data in **c, e-h, j, k** compared using student's t-test. Data in **l** compared using two-way ANOVA with Bonferroni's multiple comparison test. Figure 2a created using Biorender.

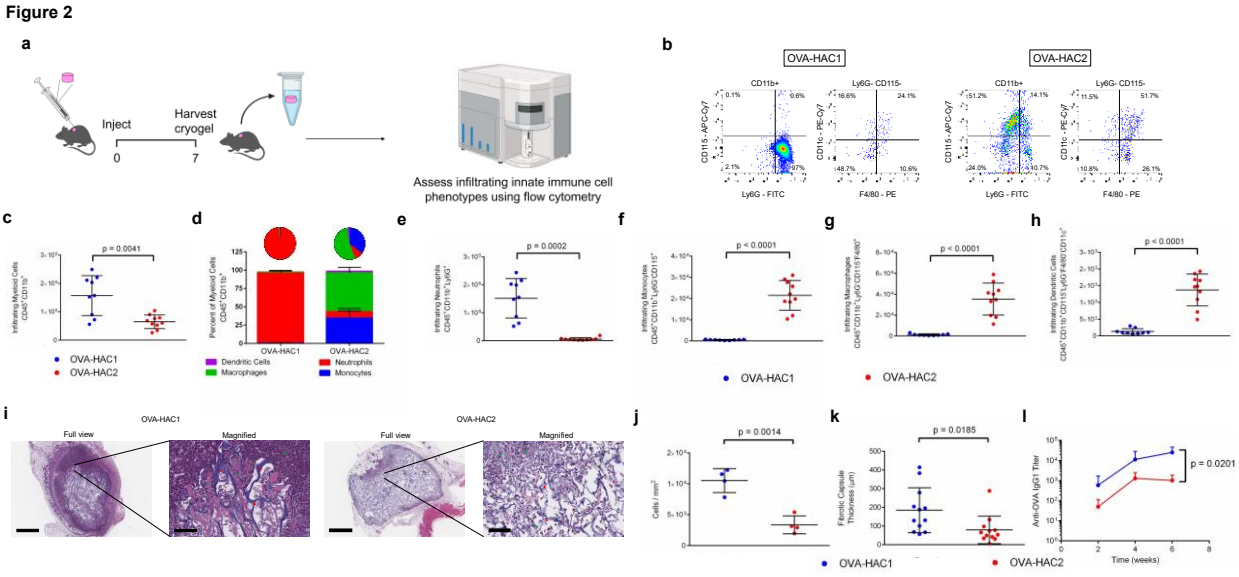

Figure 4.3| HA cryogel degradation is independent of encapsulated adjuvants
(**a**) Overview schematic depicting for in vivo degradation study. **b-e** Representative IVIS fluorescence images of cryogel degradation and quantification by measuring total radiant efficiency normalized to initial day 3 timepoint of (**b**) OVA-HAC2, (**c**) GMCSF-OVA-HAC2, (**d**) CpG-OVA-HAC2, and (**e**) GM-CSF and CpG encapsulated OVA-HAC2 (GMCSF-CpG-OVA-HAC2). Data in **e-h** represents mean ± s.e.m. of n = 5 mice. Data in **e-h** compared two-way ANOVA with Bonferroni's multiple comparison test on prime vaccine degradation curves. Figure 3a created using Biorender.

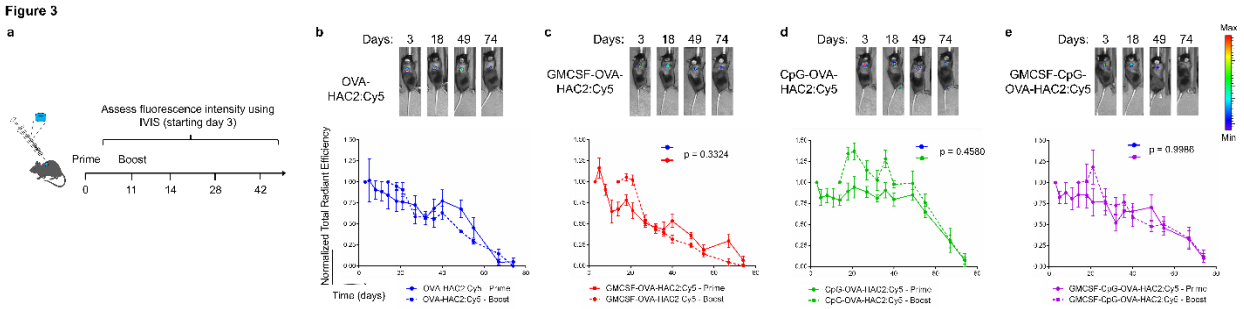

Figure 4.4| Encapsulation of adjuvants alters foreign body response
(**a**) Workflow schematic for assessing innate immune cell infiltration in HAC2, OVA-HAC2, GM-CSF and OVA encapsulated HAC2 (GMCSF-OVA-HAC2), CpG and OVA encapsulated HAC2 (CpG-OVA-HAC2), and GM-CSF, CpG, and OVA encapsulated HAC2 (GMCSF-CpG-OVA-HAC2). (**b**) Quantification of total $CD45^+CD11b^+$ (myeloid) cells in cryogels removed 10-days post-injection. (**c**) Infiltrating immune cell lineages plotted as a percentage of myeloid cells in cryogels removed 10-days post-injection. **d-g** Quantification of total numbers of (**d**) $CD45^+CD11b^+Ly6G^+$ (neutrophils), (**e**) $CD45^+CD11b^+Ly6G^-CD115^+$ (monocytes), (**f**) $CD45^+CD11b^+Ly6G^-CD115^-F4/80^+$ (macrophages), and (**g**) $CD45^+CD11b^+Ly6G^-CD115^-F4/80^-CD11c^+$ (dendritic) cells (DCs) in cryogels removed 10-days post-injection. (**h**) Hematoxylin and eosin (H&E) stained histological sections of explanted OVA-HAC2, GMCSF-OVA-HAC2, CpG-OVA-HAC2, and GMCSF-CpG-OVA-HAC2 10-days post-injection. Full view scale bar = 800 μm, magnified scale bar = 100 μm. (**i**) Quantification of cellular density in the sections from H&E slides. (**j**) Quantification of fibrotic capsule thickness in the sections from H&E slides. (**k**) Assessment of anti-OVA IgG1 antibody titers in serum of mice which received OVA-HAC2, GMCSF-OVA-HAC2, CpG-OVA-HAC2, or GMCSF-CpG-OVA-HAC2 administered in a prime and boost setting 11-days apart. Data in **b-g** represents mean ± s.d. of n = 5 cryogels. Data in **i** represents mean ± s.d. of n = 8-10 cryogels. Data in **j** represents mean ± s.d. of n = 20 measurements (4 measurements per cryogel). Data in **k** represents mean ± s.d. of n = 5 mice. Data in **b, e-g, i, j** compared using one-way ANOVA with Dunnet's multiple comparison. Data in **d** was compared using Kruskal-Wallis test with Dunnet's multiple comparison. Data in **k** was compared using two-way ANOVA with Bonferroni's multiple comparison test. Figure 4a created using Biorender.

Figure 4

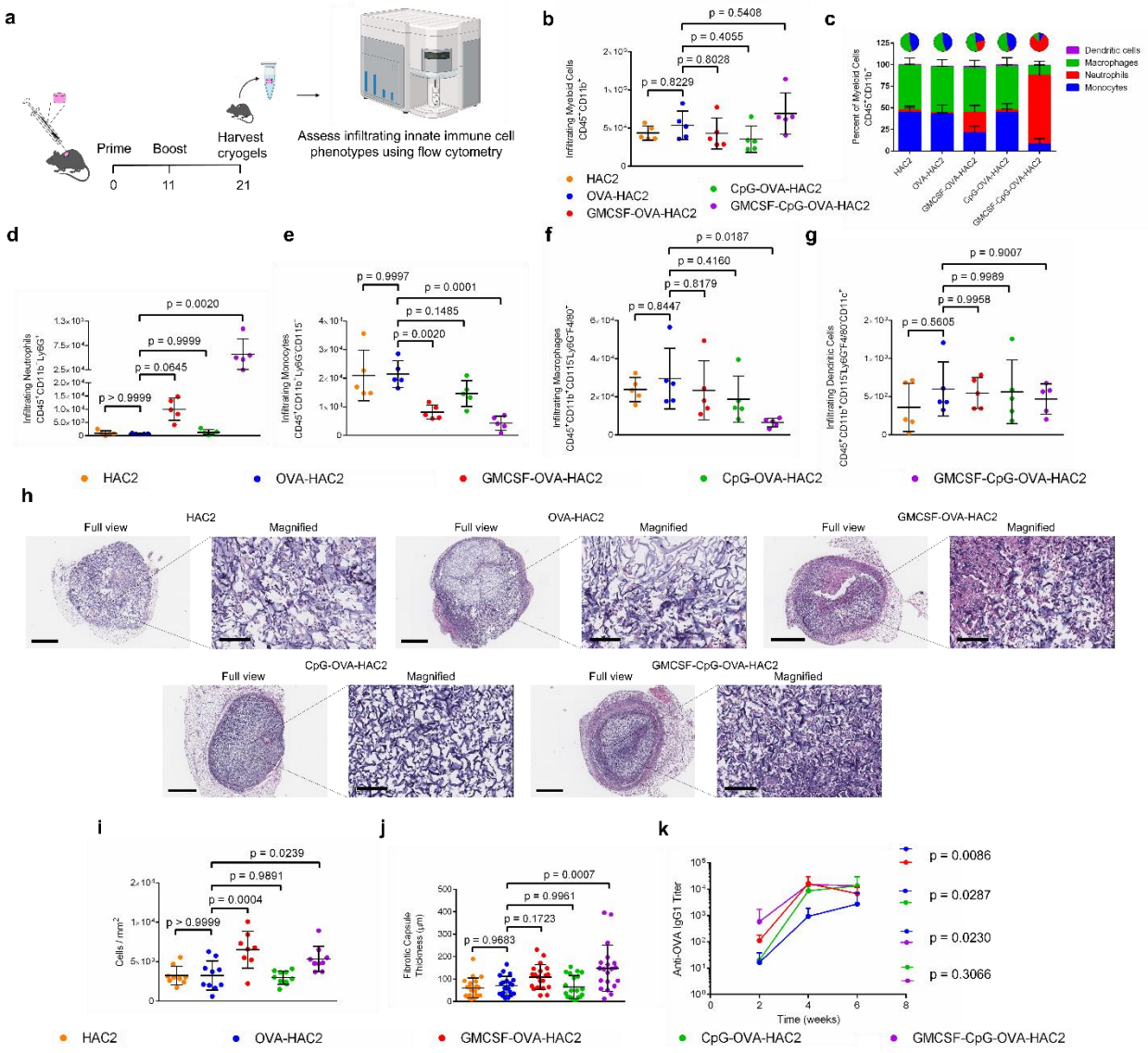
a
Prime
Boost
Harvest cryogels
0
11
21
Assess infiltrating innate immune cell phenotypes using flow cytometry
b
Infiltrating Myeloid Cells CD45+CD11b+
p = 0.5408
p = 0.4055
p = 0.8028
p = 0.8229
c
Percent of Myeloid Cells CD45+CD11b+
Dendritic cells
Macrophages
Neutrophils
Monocytes
HAC2
OVA-HAC2
GMCSF-OVA-HAC2
CpG-OVA-HAC2
GMCSF-CpG-OVA-HAC2
d
Infiltrating Neutrophils CD45+CD11b+Ly6G+
p = 0.0020
p = 0.9999
p = 0.0645
p > 0.9999
e
Infiltrating Monocytes CD45+CD11b+Ly6G-CD115+
p = 0.9997
p = 0.0001
p = 0.1485
p = 0.0020
f
Infiltrating Macrophages CD45+CD11b+CD115+Ly6G-F480+
p = 0.0187
p = 0.4160
p = 0.8179
p = 0.8447
g
Infiltrating Dendritic Cells CD45+CD11b+CD115+Ly6G-F480+CD11c+
p = 0.9007
p = 0.9989
p = 0.9958
p = 0.5605
HAC2
OVA-HAC2
GMCSF-OVA-HAC2
CpG-OVA-HAC2
GMCSF-CpG-OVA-HAC2
h
HAC2
OVA-HAC2
GMCSF-OVA-HAC2
CpG-OVA-HAC2
GMCSF-CpG-OVA-HAC2
Full view
Magnified
i
Cells / mm2
p = 0.0239
p = 0.9891
p = 0.0004
p > 0.9999
j
Fibrotic Capsule Thickness (μm)
p = 0.0007
p = 0.9961
p = 0.1723
p = 0.9683
k
Anti-OVA IgG1 Titer
Time (weeks)
p = 0.0086
p = 0.0287
p = 0.0230
p = 0.3066

Figure 4.5| Adaptive immune response to HA cryogel vaccine is dose-responsive
(**a**) Representative in vivo imaging system (IVIS) fluorescence images of Cy5-labeled CpG (CpG:Cy5) and OVA encapsulated within HA cryogels from supplier 2 (CpG:Cy5-OVA-HAC2) and measuring degradation by quantification of total radiant efficiency normalized to initial 6-hour timepoint. (**b**) Assessment of anti-OVA IgG1 antibody titers in serum of mice which received CpG-OVA-HAC2 administered as a single dose prime, two-dose prime, single dose prime and boost administered 11-days apart, or two-dose prime and boost administered 11-days apart. (**c**) Representative flow cytometry plots in axillary draining lymph nodes (LNs) to depicting gating strategy to assess $CD45^{+}B220^{-}CD8^{+}SIINFEKL^{+}$ cells (OVA-specific cytotoxic T cells). (**d**) Percentage of OVA-specific cytotoxic T cells of total $CD45^{+}B220^{-}CD8^{+}$ cells (cytotoxic T cells) in axillary draining LNs. (**e**) Representative IVIS fluorescence images of CpG and OVA encapsulated within Cy5-conjugated HAC2 (CpG-OVA-HAC2:Cy5) in B6 and $gp91^{phox-}$ mice. (**f**) Assessment of anti-OVA IgG1 antibody titers in serum of B6 and $gp91^{phox-}$ mice which received 2 CpG-OVA-HAC2:Cy5 as a prime and boost. (**g**) Overview schematic for assessing anti-OVA IgG1 antibody titers post autologous hematopoietic stem cell transplant (HSCT) mice (**h**) Anti-OVA IgG1 antibody titers in serum of mice following 2 prime and boost vaccination of either 2 bolus CpG + OVA vaccination or 2 CpG-OVA-HAC2 post-HSCT. Data in **a** represents mean ± s.e.m. of n=5 mice. Data in **b, d, f** represents mean ± s.d. of n=5 mice. Data in **h** represents mean ± s.d. of n=7 mice. Data in **b, f, h** were compared pairwise using two-way ANOVA with Bonferroni's multiple comparison test. Data in **d** was compared using one-way ANOVA with Dunnet's multiple comparison. Figure 5g created using Biorender.

Figure 5

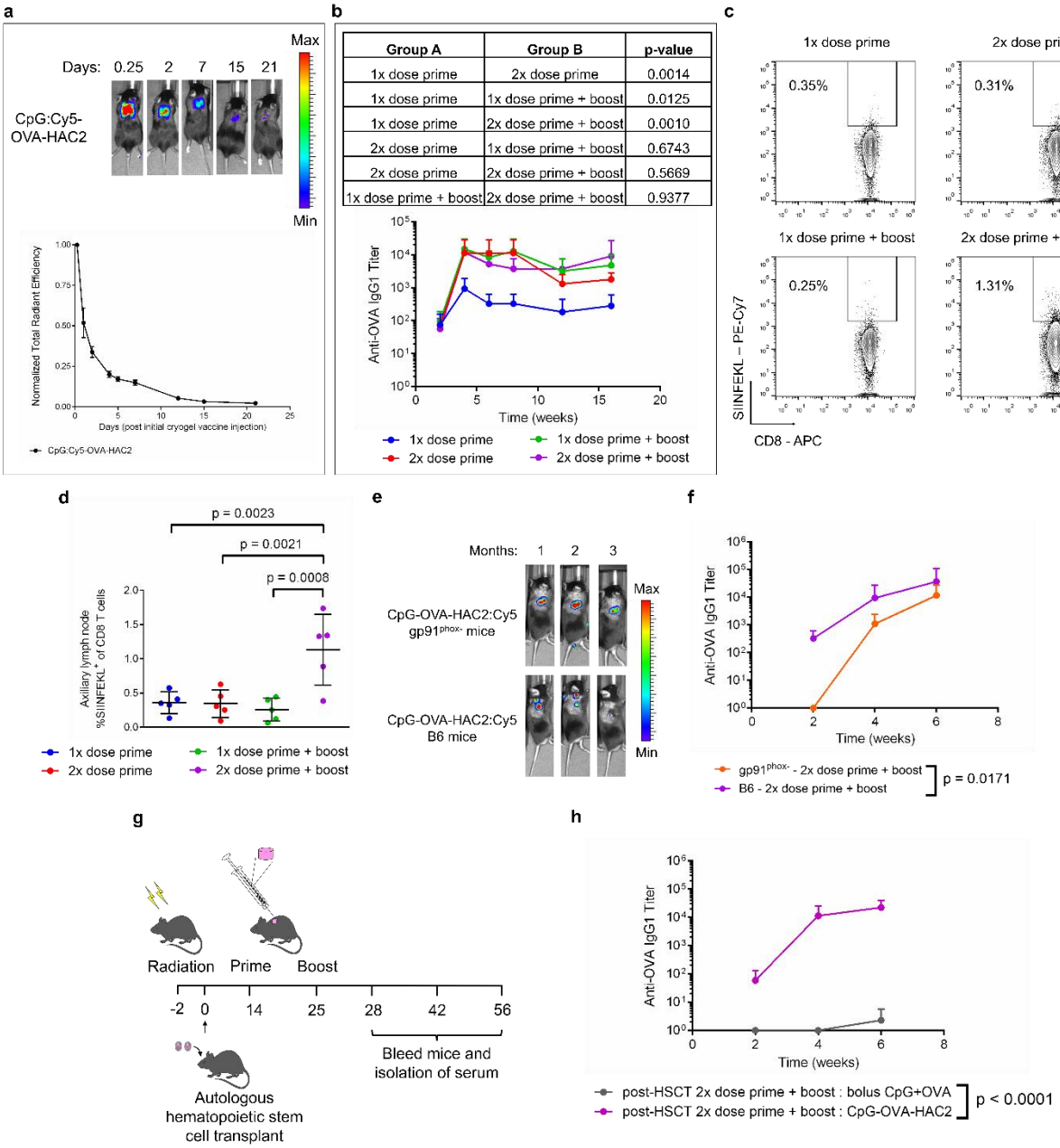
a
Days: 0.25 2 7 15 21
CpG:Cy5-OVA-HAC2
Max
Min
Normalized Total Radiant Efficiency
Days (post initial cryogel vaccine injection)
CpG:Cy5-OVA-HAC2
b
Group A | Group B | p-value
1x dose prime | 2x dose prime | 0.0014
1x dose prime | 1x dose prime + boost | 0.0125
1x dose prime | 2x dose prime + boost | 0.0010
2x dose prime | 1x dose prime + boost | 0.6743
2x dose prime | 2x dose prime + boost | 0.5669
1x dose prime + boost | 2x dose prime + boost | 0.9377
Anti-OVA IgG1 Titer
Time (weeks)
1x dose prime
2x dose prime
1x dose prime + boost
2x dose prime + boost
c
1x dose prime
2x dose prime
0.35%
0.31%
1x dose prime + boost
2x dose prime + boost
0.25%
1.31%
SIINFEKL – PE-Cy7
CD8 - APC
d
p = 0.0023
p = 0.0021
p = 0.0008
Axillary lymph node %SIINFEKL+ of CD8 T cells
1x dose prime
2x dose prime
1x dose prime + boost
2x dose prime + boost
e
Months: 1 2 3
CpG-OVA-HAC2:Cy5 gp91phox- mice
CpG-OVA-HAC2:Cy5 B6 mice
Max
Min
f
Anti-OVA IgG1 Titer
Time (weeks)
gp91phox- - 2x dose prime + boost
B6 - 2x dose prime + boost
p = 0.0171
g
Radiation
Prime
Boost
-2 0 14 25 28 42 56
Bleed mice and isolation of serum
Autologous hematopoietic stem cell transplant
h
Anti-OVA IgG1 Titer
Time (weeks)
post-HSCT 2x dose prime + boost : bolus CpG+OVA
post-HSCT 2x dose prime + boost : CpG-OVA-HAC2
p < 0.0001

Figure 4.6| CpG-OVA-HAC2 provides protection against B16-OVA melanoma
(**a**) Overview schematic for assessing prophylactic immunization in mediating protection against B16-OVA melanoma. **b-d** (**b**) Progression-free survival, (**c**) tumor volume measured in individual mice, and (**d**) overall survival. Mice were inoculated with 100K B16-OVA melanoma cells administered subcutaneously either in unvaccinated mice, or after two-dose bolus, single dose CpG-OVA-HAC2, and two-dose CpG-OVA-HAC2 administered as a prime and boost. (**e**) Quantification of anti-OVA IgG1 antibody titers in serum of vaccinated mice 6-weeks post prime and 3-weeks post tumor inoculation. (**f**) Overview schematic for assessing therapeutic immunization in mediating protection against B16-OVA melanoma. **g, h** (**g**) Tumor volume measured in individual mice and (**h**) overall survival. Data in **b, c, d** represents n=10 mice. Data in **e** represents mean ± s.d. of n=10 mice. Data in **g, h** represents n=8-10 mice. Data in **b, d, h** were compared pairwise using log-rank test. Data in **c, g** was compared using Kruskal-Wallis test with Dunnet's multiple comparison of area under the curve. Data in **e** was compared using one-way ANOVA with Dunnet's multiple comparison. Figure 6a, f created using Biorender.

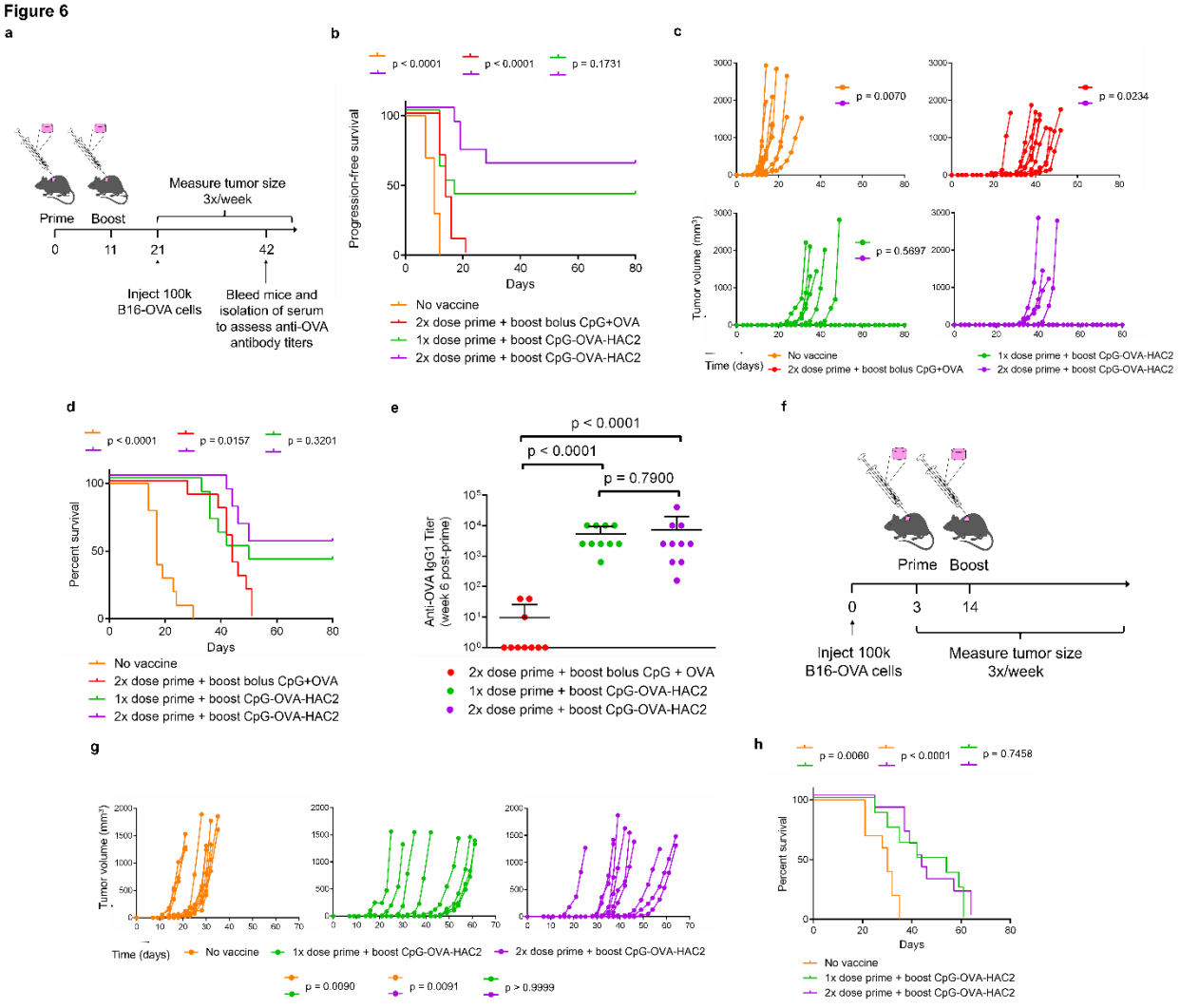

4.5 Table

Table 4.1 | Endotoxin Content of HAC1 and HAC2

HA supplier 1

Material	Sample 1 (EU/mL)	Sample 2 (EU/mL)	Sample 3 (EU/mL)
HA-Tz	0.287	0.325	0.318
Cy5-HA-Nb	0.172	0.175	0.174
HA Cryogel Average Endotoxin Content	7.3×10^{-3} EU		

HA supplier 2

Material	Sample 1 (EU/mL)	Sample 2 (EU/mL)	Sample 3 (EU/mL)
HA-Tz	0.013	0.015	0.020
Cy5-HA-Nb	0.034	0.0270	0.026
HA Cryogel Average Endotoxin Content	6.7×10^{-4} EU		

4.6 Appendix

Supplementary Figure 4.1| Extended HA cryogel characterization
(**a**) Schematic for tetrazine (Tz) and norbornene (Nb) functionalization of HA polymer, Cy5 functionalization of Nb functionalized HA polymer (Cy5-HA-Nb) and crosslinking of Tz functionalized HA polymer (HA-Tz) with Cy5-HA-Nb to make crosslinked Cy5-labled HA cryogels. (**b**) Quantification of pore diameter in HA cryogels from supplier 1 (HAC1) and supplier 2 (HAC2). (**c**) Time to 50% fluorescence intensity for OVA-HAC1:Cy5 and OVA-HAC2:Cy5. Data in **b** represents mean ± s.d. of n=3 cryogels. Data in **c** represents mean s.d. of n=5 cryogels. Data in **b**, **c** compared using student's t-test on pooled measurements.

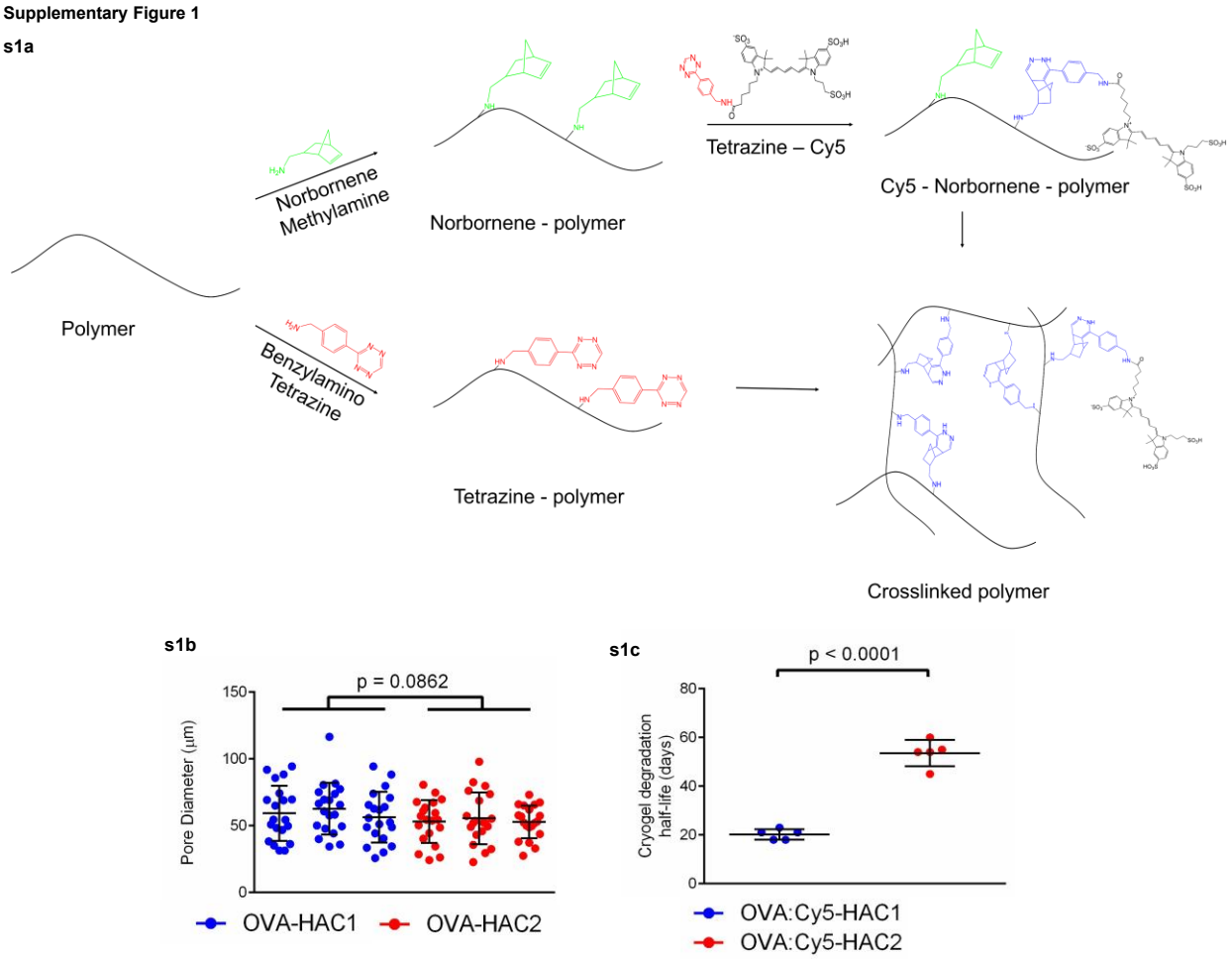

Supplementary Figure 4.2| Extended innate immune cell infiltration characterization in OVA-HAC1 and OVA-HAC2

(**a**) Representative gating strategy to determine identity of innate immune cells. (**b**) Percentage of Aqua Zombie$^-$ (live) cells within OVA-HAC1 and OVA-HAC2. **c-g** Quantification of (**c**) total CD45$^+$CD11b$^+$ (myeloid), (**d**) CD45$^+$CD11b$^+$Ly6G$^+$ (neutrophil), (**e**) CD45$^+$CD11b$^+$Ly6G$^-$CD115$^+$ (monocyte), (**f**) CD45$^+$CD11b$^+$Ly6G$^-$CD115$^-$F4/80$^+$ (macrophage), and (**g**) CD45$^+$CD11b$^+$Ly6G$^-$CD115$^-$F4/80$^-$CD11c$^+$ (dendritic) cells (DCs) in LPS-doped OVA-HAC2. (**h**) Infiltrating immune cell lineages plotted as a percentage of myeloid cells in LPS-doped OVA-HAC2. (**i**) Assessment of anti-OVA IgG1 antibody titers in serum of mice which received a single OVA-HAC2, 0.0052EU (low) LPS-doped OVA-HAC2, or 0.0533EU (high) LPS-doped OVA-HAC2 administered in a prime and boost setting 11-days apart. Data in **b** represents mean ± s.d. of n = 9 cryogels. Data in **c-h** represents mean ± s.d. of n = 5 cryogels. Data in **i** represents mean ± s.d. of n = 5 mice. Data in b compared using student's t-test. Data in **c-g** compared with one-way ANOVA with Dunnet's multiple comparison. Data in **i** compared using two-way ANOVA with Bonferroni's multiple comparison test.

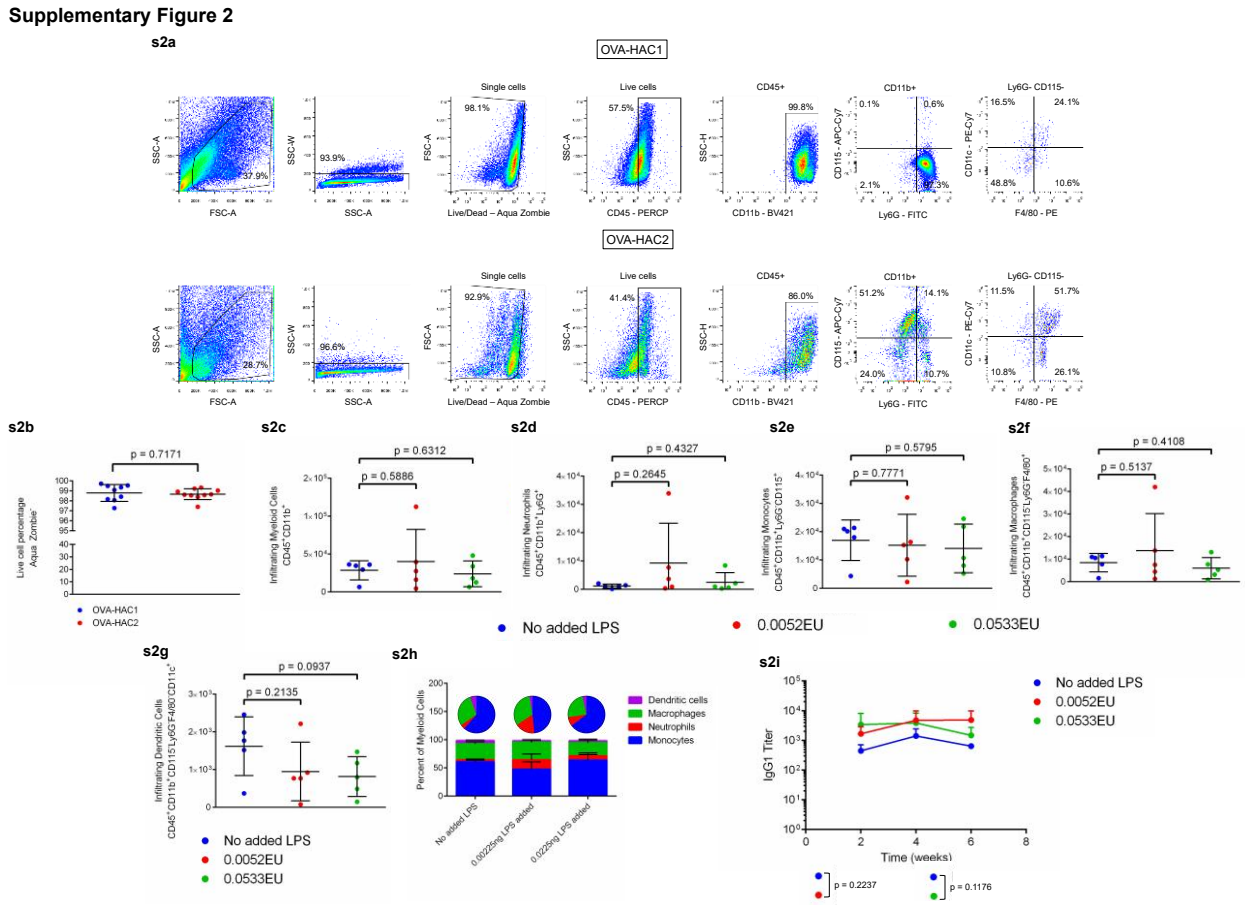

Supplementary Figure 4.3| In vitro release profile of CpG and GM-CSF
(**a**) Quantification of in vitro CpG release from CpG and OVA encapsulated HA cryogel from supplier 2 (CpG-OVA-HAC2) in both 1x PBS and hyaluronidase 2 (HYAL2) solution. (**b**) Quantification of in vitro GM-CSF release from GM-CSF and OVA encapsulated HAC2 (GMCSF-OVA-HAC2) in both 1x PBS and HYAL2 solution. Data in **a, b** represents mean ± s.d. of n = 4 cryogels. Data in **a, b** compared using two-way ANOVA with Bonferroni's multiple comparison test.

Supplementary Figure 3

s3a **s3b**

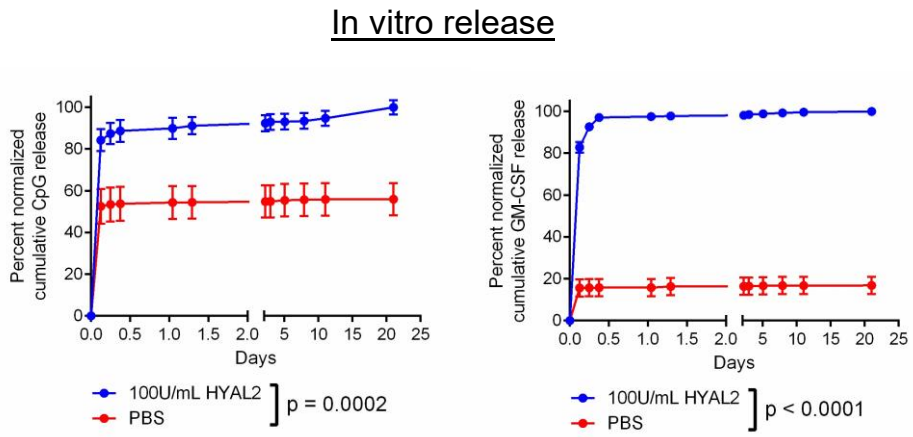

Supplementary Figure 4.4| Extended characterization of innate immune cell infiltration in adjuvanted OVA-HAC2

a,b Percentage of Aqua Zombie$^-$ (live) cells within OVA-encapsulated HA cryogel from supplier 2 (OVA-HAC2), GM-CSF and OVA encapsulated HAC2 (GMCSF-OVA-HAC2), CpG and OVA encapsulated HAC2 (CpG-OVA-HAC2), and GM-CSF, CpG, and OVA encapsulated HAC2 (GMCSF-CpG-OVA-HAC2) (**a**) 10-days and (**b**) 21-days after injection. **c-g** Quantification of (**c**) total CD45$^+$CD11b$^+$ (myeloid) cells, (**d**) CD45$^+$CD11b$^+$Ly6G$^+$ (neutrophils), (**e**) CD45$^+$CD11b$^+$Ly6G$^-$CD115$^+$ (monocytes), (**f**) CD45$^+$CD11b$^+$Ly6G$^-$CD115$^-$F4/80$^+$ (macrophages), and (**g**) CD45$^+$CD11b$^+$Ly6G$^-$CD115$^-$F4/80$^-$CD11c$^+$ (dendritic) cells in cryogels removed 21-days after injection. (**h**) Infiltrating immune cell lineages plotted as a percentage of myeloid cells in cryogels removed 21-days after injection. Data in **a-g** represents mean ± s.d. of n = 5 mice. Data in **a-g** was compared using one-way ANOVA with Dunnet's multiple comparison.

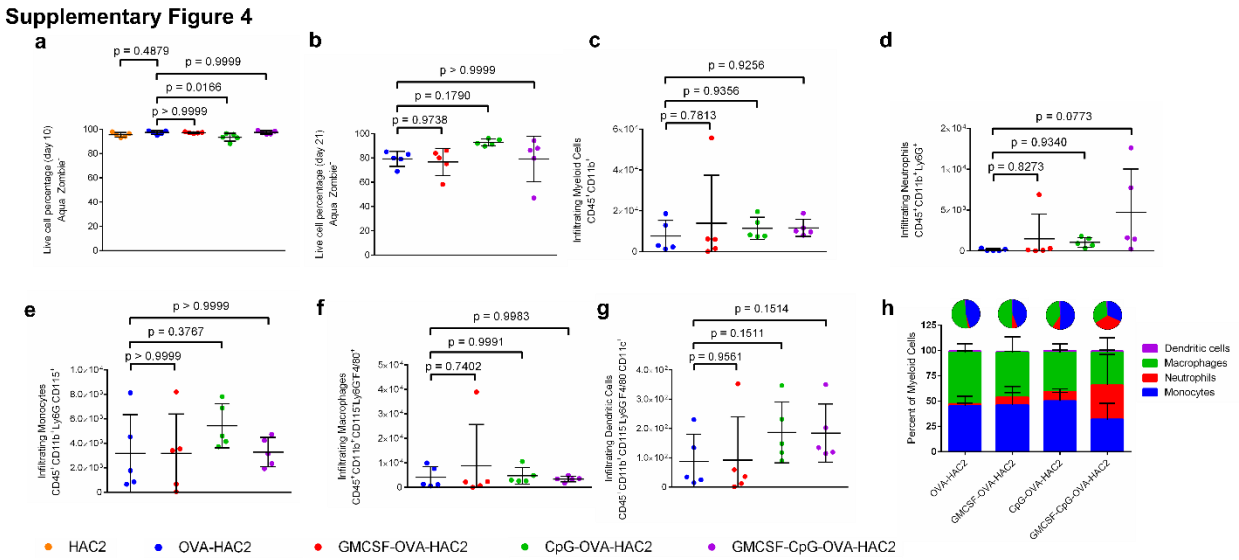

Supplementary Figure 4.5| Extended characterization assessing vaccine efficacy of bolus vaccine formulations

(**a**) Overview schematic for assessing bolus vaccine formulations. (**b**) Assessment of anti-OVA IgG1 antibody titers in serum of mice which received a single bolus OVA, bolus GM-CSF + OVA, bolus CpG + OVA, or bolus GM-CSF + CpG + OVA injection administered in a prime and boost setting 11-days apart. **c,d** Representative gating strategy to determine identity of adaptive immune cells in (**c**) draining axillary lymph nodes (LNs) and (**d**) spleen. **e, f** Percentage of $CD45^+B220^-CD8^+SIINFEKL^+$ (OVA-specific cytotoxic T cells) of total $CD45^+B220^-CD8^+$ cells (cytotoxic T cells) in (**e**) axillary lymph nodes and (**f**) spleen. Data in **b, e, f** represents mean ± s.d. of n = 5 mice. Data in **b** was compared using two-way ANOVA with Bonferroni's multiple comparison test. Data in **e, f** were compared using one-way ANOVA with Dunnet's multiple comparison. Figure 5a created using Biorender.

Supplementary Figure 5

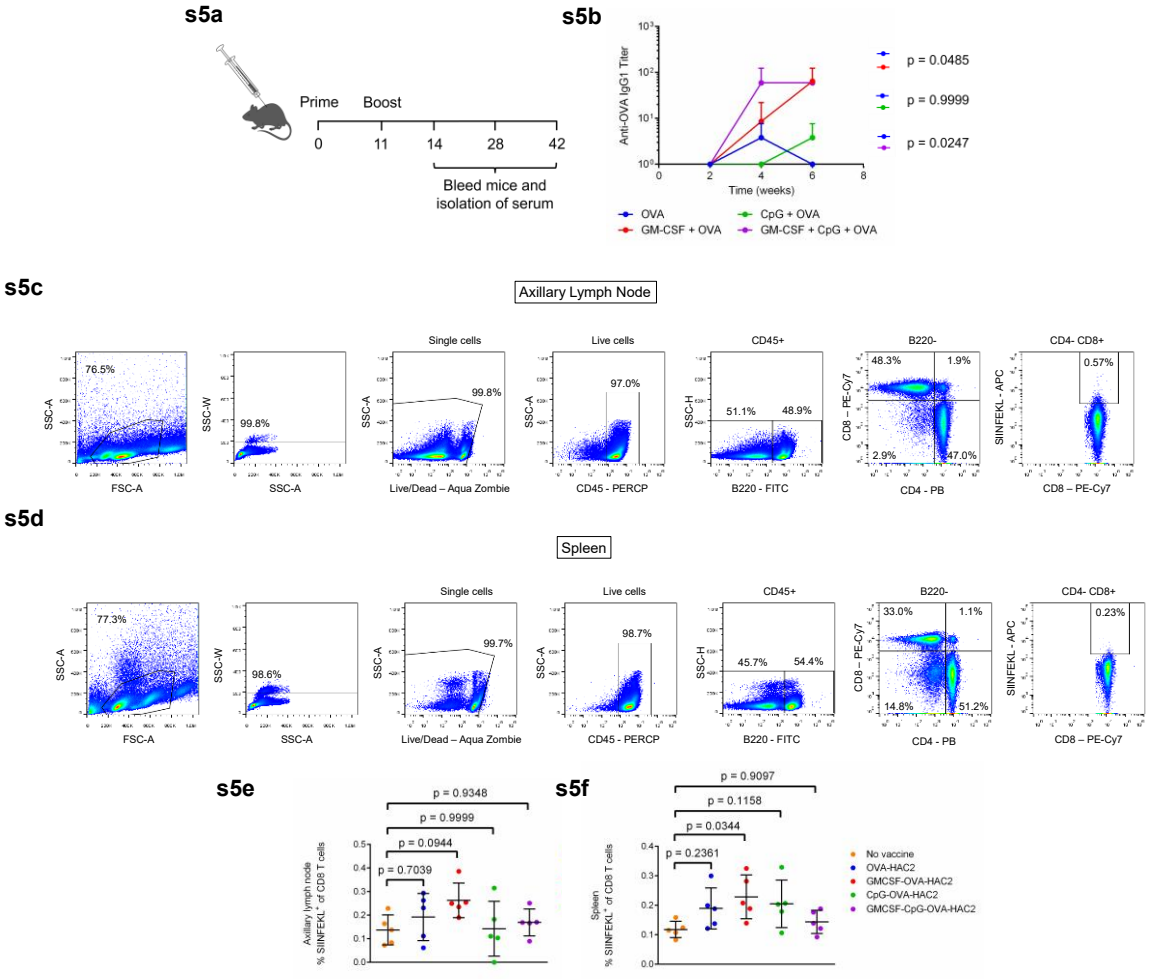

Supplementary Figure 4.6| Supplementary data for dose escalation studies
Percentage of $CD45^+B220^-CD8^+SIINFEKL^+$ cells (OVA-specific cytotoxic T cells) of total $CD45^+B220^-CD8^+$ cells (cytotoxic T cells) in spleen. Data in represents mean ± s.d. of n=5 mice and was compared using one-way ANOVA with Dunnet's multiple comparison.

Supplementary Figure 6

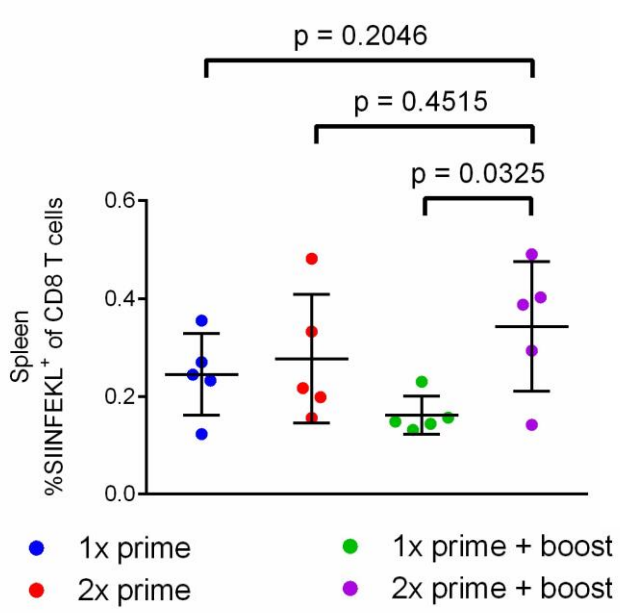

Supplementary Table 4.1

Material	Solution weight %	LPS added (ng) / HA (mg)	Sample 1 (EU/mL)	Sample 2 (EU/mL)	Sample 3 (EU/mL)	Average (EU/mL)	EU/cryogel
HA-Tz	0.3	None	0.0126	0.0146	0.0198	0.0157	
HA-Nb-Cy5	0.3	None	0.0344	0.0265	0.0263	0.0291	0.000672
HA-Tz	0.3	0.0125	0.178	0.176	0.176	0.177	
HA-Nb-Cy5	0.3	0.0125	0.174	0.170	0.166	0.170	0.00520
HA-Tz	0.03	0.125	0.188	0.183	0.184	0.185	
HA-Nb-Cy5	0.03	0.125	0.171	0.169	0.171	0.170	0.0533

Supplementary Table 4.2

Material	Sample 1 (EU/mL)	Sample 2 (EU/mL)	Sample 3 (EU/mL)	Average
RO Water	<0.01	<0.01	<0.01	<0.01
CpG-ODN (100µg/mL)	<0.01	<0.01	<0.01	<0.01
GM-CSF (1µg/mL)	<0.01	<0.01	<0.01	<0.01
OVA (vaccine grade, 100µg/mL)	0.0299	0.0280	0.0305	0.0294
HA-Tz (0.3wt%, HA supplier 2)	0.0126	0.0146	0.0198	0.0157
HA-Nb-Cy5 (0.3wt%, HA supplier 2)	0.0344	0.0265	0.0263	0.0291

4.7 Methods

4.7.1 General methods and statistics

Sample sizes for animal studies were based on prior work without use of additional statistical estimations[12]. Results were analyzed where indicated using student's t-test, one-way ANOVA with Dunnett's multiple comparison, Kruskal-Wallis test with Dunnet's multiple comparison, two-way ANOVA with Bonferroni's test, and log-rank test using Graphpad Prism software. Alphanumeric coding was used in blinding for pathology samples and cell counting.

4.7.2 Reagents

Sodium hyaluronate was purchased from Acros Organics (MW 1.5-2.2MDa, lot: A0405554, Supplier 1) and NovaMatrix (MW 1.2-1.9 MDa, Pharma Grade 150, lot: 18011K, Supplier 2). (2-morpholinoethanesulfonic acid (MES), sodium chloride (NaCl), sodium hydroxide (NaOH), *N*-hydroxysuccinimide (NHS), 1-ethyl-3-(3-dimethylaminopropyl)-carbodiimide hydrochloride (EDC), sodium periodate (311448) and ammonia borane (AB) complex (682098) were purchased from Sigma-Aldrich. (4-(1,2,4,5-tetrzain-3-yl)phenyl)methanamine (tetrazine amine) was purchased from Kerafast (FCC659, lot: 2014). 1-bicyclo[2.2.1]hept-5-en-2-ylmethanamine (norbornene amine) was purchased from Matrix Scientific (# 038023, lot: M15S). Cy5-tetrazine amine was purchased from Lumiprobe (lot: 9D2FH). 1kDa molecular weight cutoff (MWCO) mPES membrane was purchased from Spectrum (S02-E001-05-N). GM-CSF was purchased from PeproTech (AF-315-03, lot: 081955). CpG (CpG ODN 1826, 5′-TCC ATG ACG TTC CTG ACG TT-3′) was purchased from Integrated DNA Technologies (lots: 480037977, 513470982). CpG:Cy5 (CpG ODN 1826, 5′-Cy5 TCC ATG ACG TTC CTG

ACG TT-3′) was purchased from Integrated DNA Technologies (lot: 526167013). Vaccine grade OVA was purchased from Invivogen (vac-pova-100, lot: 5822-04-01). Lipopolysaccharide (LPS) was purchased from Sigma-Aldrich (L3012-5MG, lot: 0000091258).

4.7.3 Derivatization of HA

Tetrazine functionalized HA (HA-Tz) or norbornene functionalized HA (HA-Nb) were prepared by reacting tetrazine amine or norbornene amine to HA using EDC/NHS carbodiimide chemistry. Sodium hyaluronate was dissolved in a buffer solution (0.75% wt/vol, pH ~ 6.5) of 100mM MES buffer. NHS and EDC were added to the mixture to activate the carboxylic acid groups on the HA backbone followed by either tetrazine amine or norbornene amine. HA from both suppliers was assumed to be 1.8 MDa for purposes of conjugation reactions. To synthesize HA-Tz, the molar ratios of HA:EDC:NHS:tetrazine are 1:25000:25000:2500. To synthesize HA-Nb, the molar ratios of HA:EDC:NHS:norbornene are 1:25000:25000:2500. Each reaction was stirred at room temperature for 24 hours and transferred to a 12,000Da MW cutoff dialysis sack (Sigma Aldrich) and dialyzed in 4L of NaCl solutions of decreasing molarity (0.125M, 0.100M, 0.075M, 0.050M, 0.025M, 0M, 0M, 0M, 0M) for 8 hours per solution. After dialysis, solutions containing HA-Tz or HA-Nb were frozen overnight and lyophilized (Labconco Freezone 4.5) for 48 hours. Cy5 conjugated HA-Nb (Cy5-HA-Nb) was synthesized following a previously described technique[12]. 0.8mg of Cy5-Tz was reacted with 100mg of HA-Nb at 0.2 wt/vol in DI water for 24 hours at 37 ^{o}C and purified by dialysis in DI water using a 12,000Da MW cutoff dialysis sack for 48 hours. Dialysis water bath was changed

every ~8 hours. The Cy5-HA-Nb solution was then frozen overnight and lyophilized for 48 hours.

4.7.4 Cryogel formation

We followed a previously described cryogelation method[12]. To form cryogels, aqueous solutions of 0.6% wt/vol HA-Tz and Cy5-HA-Nb were prepared by dissolving lyophilized polymers into deionized water and left on a rocker at room temperature for a minimum of 8 hours to allow for dissolution. The aqueous solutions were then pre-cooled to 4^{o}C before crosslinking to slow reaction kinetics. HA-Tz and HA-Nb solutions were mixed at a 1:1 volume ratio, pipetted into 30µL Teflon molds which were pre-cooled to -20 ^{o}C, and quickly transferred to a -20 ^{o}C freezer to allow for overnight cryogelation. To form OVA-HA cryogels, HA-Tz and Cy5-HA-Nb were solubilized in 3.33mg/mL OVA solution in DI water prior to crosslinking. To form HA cryogel vaccines, 1µL/cryogel of CpG (100mg/mL concentration) and/or GM-CSF (1mg/mL concentration) was added to HA-Tz or Cy5-HA-Nb solubilized in OVA solution prior to crosslinking.

4.7.5 Endotoxin Testing

Endotoxin testing was conducted using a commercially available endotoxin testing kit (88282, Thermo Fisher Scientific, lot: VH310729) and following manufacturer's instructions. HA-Tz and Cy5-HA-Nb from both suppliers were solubilized at 0.3 wt% in endotoxin free water and samples were tested in technical triplicates. To calculate endotoxin content of a single HA cryogel, the EU/mL concentration for HA-Tz and Cy5-HA-Nb were multiplied by 0.03 (30uL of volume per HA cryogel). Other components of the HA cryogel vaccine formulations tested for endotoxin included CpG (100µg/mL

concentration), OVA (100µg/mL concentration), GM-CSF (1µg/mL concentration), and RO water which was used to solubilize all vaccine components.

4.7.6 Pore size analysis of HA cryogels

For scanning electron microscopy (SEM), frozen HA cryogels were lyophilized for 24 hours in their molds. Lyophilized HA cryogels were adhered onto sample stubs using carbon tape and coated with iridium in a sputter coater. Samples were imaged using secondary electron detection on a FEI Quanta 250 field emission SEM in the Nano3 user facility at UC San Diego. Fluorescence images of Cy5-labled HA cryogels were acquired using a Leica SP8 All experiments were performed at the UC San Diego School of Medicine Microscopy Core. Pore size quantification of SEM images was quantified using FIJI image processing package[54].

4.7.7 LPS doping of HAC2

LPS was added to HA-Tz and HA-Nb solutions from supplier 2 at either 12.5ng/100mg or 1.25ng/100mg. The mixtures were stirred for 24 hours and then frozen overnight and lyophilized for 48 hours. Lyophilized polymers were rehydrated to assess endotoxin concentration prior to conducting in vivo studies.

4.7.8 HA cryogel pore-interconnectedness analysis

Cy5-labeled HA cryogels were incubated in 1mL of FITC-labeled 10µM diameter melamine resin micro particles (Sigma Aldrich) at 0.29mg/mL concentration on a rocker at room temperature overnight. Fluorescence images of HA cryogels with FITC-labeled microparticles were acquired using a Leica SP8 confocal. Interconnectedness of the HA cryogels was determined by generating 3D renderings of confocal z-stacks using FIJI imaging processing package and assessing fluorescence intensity of both the Cy5 and

FITC channels with depth starting from the top of the HA cryogel. All experiments were performed at the UC San Diego School of Medicine Microscopy Core.

4.7.9 In vitro degradation of HA cryogels

Cy5-labled HA cryogels were placed into individual 1.5mL microcentrifuge tubes (3448, Thermo Scientific, lot: 20430852) with 1mL of 100U/mL Hyaluronidase from sheep testes Type II (HYAL2, H2126, Sigma Aldrich, lot: SLBZ9984) in 1x phosphate buffered saline (PBS). Degradation studies were conducted in tissue culture incubators at 37 ^{o}C. Supernatant from samples were collected by centrifuging the samples at room temperature at 2,000G for 5 minutes and removing 0.9mL of supernatant. HA cryogels were resuspended by adding 0.9mL of freshly made 100U/mL HYAL2 in 1x PBS. Fluorescence measurements were conducted using a Nanodrop 2000 Spectrophotometer (Thermo Fisher Scientific) and these values were normalized to sum of the fluorescence values over the course of the experiment.

4.7.10 In vitro release assays

OVA-HAC1, OVA-HAC2, CpG-OVA-HAC2, or GMCSF-OVA-HAC2 were placed into individual 1.5mL microcentrifuge tubes in either 1mL of 1x PBS or 100U/mL HYAL2 solubilized in 1x PBS. Quantification of in vitro OVA release was conducted using a Micro BCA kit (Thermo Fisher Scientific, lot: UD277184) on supernatant samples. Absorbance values of 100U/mL HYAL2 solution was assessed and subtracted from absorbance values in supernatant containing HYAL2 solution. Quantification of in vitro CpG release was conducted using OliGreen Assay kit (Thermo Fisher Scientific, lot: 2471822). Quantification of in vitro GM-CSF release was conducted using Murine GM-CSF ELISA kit (Peprotech, lot: 1010055).

4.7.11 Cell lines and cell culture

The B16-OVA cell line was obtained from Professor Liangfang Zhang's laboratory (University of California, San Diego). The cells were cultured in Dulbecco's modified eagle medium (DMEM, Gibco, lot: 2060444) supplemented with 10% fetal bovine serum (Gibco), 1% penicillin-streptomycin (Corning, lot: 30002357), and 300μg/mL hygromycin B (Corning, lot: 30240136, selective antibiotic for OVA-expressing cells).

4.7.12 In vivo mouse experiments

All animal work was conducted at the Moores Cancer Center vivarium at UC San Diego and approved by the Institutional Animal Care and Use Committee (IACUC) under protocol number S17160. All animal experiments followed the National Institutes of Health guidelines and relevant AALAC-approved procedures. Female C57BL/6J mice (B6, Jax # 000664) and BALB/cJ mice (Jax # 000651) were 6-8 weeks at the start of the experiments. Male B6 and B6.129S-Cybbtm1Din ($gp91^{phox-}$, Jax # 002365) mice were 6-8 weeks old at the start of experiments. All mice in each experiment were age and sex matched and no randomization was performed. This work did not assess if there are sex-differences associated with the observed effects. Female mice are commonly used in mouse model of melanoma. Previous studies have shown sex-based differences in adaptive immune response to both vaccination and tumor growth rate[63,64]. Females typically develop higher antibody titers than males and tumor growth rate in murine melanoma is slowed in female mice due to a more robust adaptive immune response. It is unknown if there are sex-differences in the mouse HSCT model described in this work. Male mice were used in the $gp91^{phox-}$ studies as the mutation is X-linked and males but not females lack superoxide production[65,66].

4.7.13 Subcutaneous cryogel administration

HA cryogels suspended in 200μL of sterile 1x PBS were administered into the dorsal flank of mice by means of a 16G needle positioned approximately midway between the hind- and forelimbs. The site of injection was shaved and wiped with a sterile alcohol pad prior to gel injection.

4.7.14 In vivo cryogel degradation

In vivo OVA-HAC1:Cy5 and OVA-HAC2:Cy5 degradation studies were performed in B6 mice and gp91^{phox-} mice. In all cases, Cy5-labeled cryogels were administered into the dorsal flank of an anesthetized mouse and the fluorescent intensity of the HA cryogel was quantified using an IVIS spectrometer (PerkinElmer) at predetermined timepoints and analyzed using LivingImage software (PerkinElmer). At each timepoint, mice were anesthetized and the area around the subcutaneous cryogel was shaved to reduce fluorescence signal attenuation. Fluorescence radiant efficiency, the ratio of fluorescence emission to excitation, was measured longitudinally as a metric to quantify fluorescence from subcutaneous cryogels. These values were normalized to the measured signal on day 3. All experiments were performed at the Moores Cancer Microscopy Core Facility at UC San Diego Health using an IVIS spectrometer.

4.7.14 In vivo release

For in vivo release assays, OVA:Cy5 was prepared by reacting OVA with sulfo-Cy5 NHS ester (Lumiprobe, lot: lot: 7FM7C) at a 1:50:5 molar ratio of OVA:EDC:Sulfo-Cy5 NHS ester in MES buffer to form OVA:Cy5. Unreacted EDC and sulfo-Cy5 NHS ester were removed by overnight dialysis using a 12kDa MWCO dialysis membrane (D6191, Sigma Aldrich, lot: SLCL5005). 100μg of OVA:Cy5 was added to either HAC1 or HAC2 polymer

mixture prior to crosslinking. To make CpG:Cy5-OVA-HAC2, 100μg of CpG:Cy5 was added to OVA-HAC2 polymer mixture prior to crosslinking. For all in vivo release assays, release was assessed normalized to a 6-hour initial timepoint in an analogous manner to in the in vivo cryogel degradation studies in the previous section.

4.7.15 Detection of serum anti-OVA IgG1 antibody titers

Blood was first collected from the tail vein of mice into EDTA coated tubes (365974, BD, lot: 2181885). Blood was centrifuged at 2,000G for 10 minutes at room temperature for serum collection. Anti-OVA IgG1 antibody titers were quantified using ELISA following established protocol[42]. High-binding (3590, Corning) ELISA plates were coated with 1μg/mL OVA in PBS at 4 °C overnight. Serum samples were diluted ranging from 1:8 to 1:1:163840 and incubated with the plates at room temperature for 1.5 hours before staining for mouse IgG1 (406604, Biolegend, lot: B270354). The anti-OVA titer was defied as the lowest serum dilution with an optical density value above 0.2.

4.7.16 Flow cytometry analysis

Anti-mouse antibodies to CD45 (30-F11, lot: B280746), CD11b (M1/70, lot: B322056), Ly6-G/Gr-1 (1A8, lot: B259670), CD115 (CSF-1R, lot: B291837), CD11c (N418, lot: B346713), CD4 (RM4-5, lot: B240051), CD8α (53-6.7, lot: B266721), and B220 (RA3-6B2, lot: B298555) were purchased from Biolegend. Anti-mouse F4/80 (BM8, lot: 2229150) and was purchased from eBioscience. SIINFEKL tetramer (lot: 57396) was sourced from the NIH tetramer core. All cells were gated based on forward and side scatter characteristics to limit debris, including dead cells. Aqua Zombie fixable viability kit (423102, Biolegend, lot: B348291) was used to separate live and dead cells. Antibodies were diluted 1:400 v/v in staining buffer in and added to cells in 1:1 v/v ratio.

Cells were gated based on fluorescence-minus-one controls, and the frequencies of cells staining positive for each marker were recorded. To quantify infiltrating immune cells within HA cryogels, spleen, and axillary LNs, mice were sacrificed, organ or HA cryogel was removed, and crushed against a 70-micron filter screen before antibody staining. All flow cytometry experiments were performed using a Attune® NxT Acoustic Focusing cytometer analyzer (A24858) at UC San Diego. Flow cytometry was analyzed using FlowJo (BD) software.

4.7.17 Histology

After euthanasia, HA cryogels were explanted and fixed in 4% paraformaldehyde (PFA) for 24 hours. 4% PFA was prepared by diluting 16% PFA stock (28908, Thermo Fisher Scientific, lot: XB340632) in 1x PBS. The fixed HA cryogels were then transferred to 70% ethanol solution. Samples were routinely processed, and sections (5μm) were stained and digitized using an Aperio AT2 Automated Digital Whole Slide Scanner by the Tissue Technology Shared Resource at the Moores Cancer Center at UC San Diego Health. Digital slides were rendered in QuPath and positive cell detection was used to quantify the total number of mononuclear cells within each image. Quantification of mononuclear cell density was determined for each histological section. To quantify fibrotic capsule thickness, Qupath was used to measure the epithelial cell layer starting at the edge of the cryogel. Four measurements per cryogel were taken and all measurements were pooled for analysis.

4.7.18 Hematopoietic stem cell transplant

Irradiations were performed with a Cesium-137 gamma-radiation source irradiator (J.L. Shepherd & Co.). Syngeneic HSCT (B6 donor and recipient) and allogenic HSCT (BalbC

donors, B6 recipients) consisted of 2 doses of 5000 cGy 6-hours apart + 15M whole bone marrow cells and 10M splenocytes. Bone marrow cells for transplantation (from donors) were harvested by crushing all limbs with a mortar and pestle, diluted in 1× PBS, filtering the tissue homogenate through a 70 μm mesh and preparing a single-cell suspension by passing the cells in the flowthrough once through a 20-gauge needle. Splenocytes were collected by crushing spleens against a 70 μm mesh and preparing a single-cell suspension by passing the cells in the flowthrough once through a 20-gauge needle. Total cellularity was determined by counting cells using a hemacytometer. Subsequently, cells were suspended in 100 μl of sterile 1× PBS and administered to anesthetized mice via a single retroorbital injection. All experiments were performed at the Moores Cancer Animal Facility at UC San Diego Health.

4.7.19 Prophylactic immunization

CpG-OVA-HAC2 were administered to mice in a prime and boost schedule 11-days apart. Unvaccinated mice were used as a control. Mice were challenged 21 days post-prime with 100 thousand B16-OVA cells in 100μL cold PBS injected subcutaneously below the neck using an insulin syringe. Tumor growth was monitored using calipers. Tumor volume was calculated assuming an ellipsoid (Volume = 4/3 * π * long axis/2 * short axis/2 * height/2). Mice were euthanized when the tumor volume exceeded 1200mm^3.

4.7.20 Therapeutic immunization

100K B16-OVA cells in 100 μL cold PBS injected subcutaneously below the neck using an insulin syringe. CpG-OVA-HAC2 were administered to mice 3-days post tumor inoculation in a prime and boost schedule 11-days apart. Tumor growth was monitored using calipers. Tumor volume was calculated assuming an ellipsoid (Volume = 4/3 * π *

long axis/2 * short axis/2 * height/2). Mice were euthanized when the tumor volume exceeded 1200 mm^3.

4.8 Acknowledgements

Matthew D. Kerr: Conceptualization, methodology, validation, formal analysis, investigation, resources, data curation, writing – original draft, writing – review & editing and visualization. **Wade T. Johnson:** Investigation, writing – review and editing. **David A. McBride:** Investigation and writing – review and editing. **Arun K. Chumber:** Investigation and writing – review and editing. **Nisarg J. Shah:** Conceptualization, writing - original draft, writing – review and editing, supervision, project administration, funding acquisition. All authors reviewed the manuscript and data, provided input and approved the submission.

The work was supported in part by the American Cancer Society (IRG-15-172-45-IRG), National Multiple Sclerosis Society (PP-1905-34013). M.D.K received NIH training grant support through the NCI (T32CA153915) and NHLBI (F31HL164055). W.T.J and D.A.M received NIH training support through NIAMS (T32AR064194 and F31AR079921, respectively). The authors acknowledge assistance by the Moores Cancer Center Tissue Technology Shared Resource at UC San Diego Health, the Microscopy Core at UC San Diego School of Medicine, and the Biostatistics Unit of the Clinical and Translational Research Institute at UC San Diego supported by the National Institutes of Health (P30NS047101 and UL1TR001442 respectively). This work was performed in part at the San Diego Nanotechnology Infrastructure (SDNI) of UCSD, a member of the National Nanotechnology Coordinated Infrastructure (NNCI), which is supported by the National Science Foundation under Grant No. ECCS-2025752. The content is solely the

responsibility of the authors and does not necessarily represent the official views of the funding agencies, which includes the National Institutes of Health and the National Science Foundation.

The datasets generated during and/or analyzed during the current study are available from the corresponding authors on reasonable request.

Chapter 4, in full, is a copy of a manuscript accepted for publication in Bioengineering & Translational medicine with the following authors Matthew D. Kerr, Wade T. Johnson, David A. McBride, Arun K. Chumber, Nisarg J. Shah. The dissertation author was the primary investigator and author of this paper.

4.9 References

1. Roth, G. A. et al. Injectable Hydrogels for Sustained Codelivery of Subunit Vaccines Enhance Humoral Immunity. ACS Cent Sci 6, 1800–1812 (2020).

2. Shah, N. J. et al. A biomaterial-based vaccine eliciting durable tumour-specific responses against acute myeloid leukaemia. Nat Biomed Eng 4, 40–51 (2020).

3. Cirelli, K. M. et al. Slow Delivery Immunization Enhances HIV Neutralizing Antibody and Germinal Center Responses via Modulation of Immunodominance. Cell 177, 1153-1171.e28 (2019).

4. Dalla Pietà, A. et al. Hyaluronan is a natural and effective immunological adjuvant for protein-based vaccines. Cell Mol Immunol 18, 1197–1210 (2021).

5. Chen, J. et al. Sustained Delivery of SARS-CoV-2 RBD Subunit Vaccine Using a High Affinity Injectable Hydrogel Scaffold. Adv Healthc Mater 11, 2101714 (2022).

6. Moon, S., Shin, E.-C., Noh, Y.-W. & Lim, Y. T. Evaluation of hyaluronic acid-based combination adjuvant containing monophosphoryl lipid A and aluminum salt for hepatitis B vaccine. Vaccine 33, 4762–4769 (2015).

7. Kuai, R. et al. Dual TLR agonist nanodiscs as a strong adjuvant system for vaccines and immunotherapy. Journal of Controlled Release 282, 131–139 (2018).

8. Hao, H. et al. Immunization against Zika by entrapping live virus in a subcutaneous self-adjuvanting hydrogel. Nat Biomed Eng (2023) doi:10.1038/s41551-023-01014-4.

9. Shih, T.-Y. et al. Injectable, Tough Alginate Cryogels as Cancer Vaccines. Adv Healthc Mater 7, 1701469 (2018).

10. Weiden, J. et al. Robust Antigen-Specific T Cell Activation within Injectable 3D Synthetic Nanovaccine Depots. ACS Biomater Sci Eng 7, 5622–5632 (2021).

11. Selders, G. S., Fetz, A. E., Radic, M. Z. & Bowlin, G. L. An overview of the role of neutrophils in innate immunity, inflammation and host-biomaterial integration. Regen Biomater 4, 55–68 (2017).

12. Kerr, M. D. et al. Immune-responsive biodegradable scaffolds for enhancing neutrophil regeneration. Bioeng Transl Med 8, (2023).

13. Burdick, J. A., Chung, C., Jia, X., Randolph, M. A. & Langer, R. Controlled Degradation and Mechanical Behavior of Photopolymerized Hyaluronic Acid Networks. Biomacromolecules 6, 386–391 (2005).

14. Hopkins, K. et al. Sustained degradation of hyaluronic acid using an in situ forming implant. PNAS Nexus 1, pgac193 (2022).

15. Weeratna, R. D., Makinen, S. R., McCluskie, M. J. & Davis, H. L. TLR agonists as vaccine adjuvants: comparison of CpG ODN and Resiquimod (R-848). Vaccine 23, 5263–5270 (2005).

16. Zhang, X. et al. The Toll-Like Receptor 9 Agonist, CpG-Oligodeoxynucleotide 1826, Ameliorates Cardiac Dysfunction After Trauma-Hemorrhage. Shock 38, (2012).

17. Krogmann, A. O. et al. Proinflammatory Stimulation of Toll-Like Receptor 9 with High Dose CpG ODN 1826 Impairs Endothelial Regeneration and Promotes Atherosclerosis in Mice. PLoS One 11, e0146326- (2016).

18. Inaba, K. et al. Identification of proliferating dendritic cell precursors in mouse blood. Journal of Experimental Medicine 175, 1157–1167 (1992).

19. Sallusto, F. & Lanzavecchia, A. Efficient presentation of soluble antigen by cultured human dendritic cells is maintained by granulocyte/macrophage colony-stimulating factor plus interleukin 4 and downregulated by tumor necrosis factor alpha. Journal of Experimental Medicine 179, 1109–1118 (1994).

20. Lutz, M. B. et al. Immature dendritic cells generated with low doses of GM-CSF in the absence of IL-4 are maturation resistant and prolong allograft survival in vivo. Eur J Immunol 30, 1813–1822 (2000).

21. Zhan, Y., Lew, A. M. & Chopin, M. The Pleiotropic Effects of the GM-CSF Rheostat on Myeloid Cell Differentiation and Function: More Than a Numbers Game. Front Immunol 10, (2019).

22. Zhang, C., Wang, B. & Wang, M. GM-CSF and IL-2 as adjuvant enhance the immune effect of protein vaccine against foot-and-mouth disease. Virol J 8, 7 (2011).

23. Hasan, M. S. et al. Granulocyte Macrophage Colony-Stimulating Factor as an Adjuvant for Hepatitis B Vaccination of Healthy Adults. J Infect Dis 180, 2023–2026 (1999).

24. Zhao, W., Zhao, G. & Wang, B. Revisiting GM-CSF as an adjuvant for therapeutic vaccines. Cell Mol Immunol 15, 187–189 (2018).

25. Banerjee, E. R. & Henderson, W. R. Role of T cells in a gp91phox knockout murine model of acute allergic asthma. Allergy, Asthma & Clinical Immunology 9, 6 (2013).

26. Pollock, J. D. et al. Mouse model of X–linked chronic granulomatous disease, an inherited defect in phagocyte superoxide production. Nat Genet 9, 202–209 (1995).

27. Petrey, A. & de la Motte, C. Hyaluronan, a Crucial Regulator of Inflammation. Front Immunol 5, (2014).

28. Ruppert, S. M., Hawn, T. R., Arrigoni, A., Wight, T. N. & Bollyky, P. L. Tissue integrity signals communicated by high-molecular weight hyaluronan and the resolution of inflammation. Immunol Res 58, 186–192 (2014).

29. Gariboldi, S. et al. Low Molecular Weight Hyaluronic Acid Increases the Self-Defense of Skin Epithelium by Induction of β-Defensin 2 via TLR2 and TLR4. The Journal of Immunology 181, 2103–2110 (2008).

30. Rayahin, J. E., Buhrman, J. S., Zhang, Y., Koh, T. J. & Gemeinhart, R. A. High and Low Molecular Weight Hyaluronic Acid Differentially Influence Macrophage Activation. ACS Biomater Sci Eng 1, 481–493 (2015).

31. Bourguignon, L. Y. W., Wong, G., Earle, C. A. & Xia, W. Interaction of low molecular weight hyaluronan with CD44 and toll-like receptors promotes the actin filament-associated protein 110-actin binding and MyD88-NFκB signaling leading to proinflammatory cytokine/chemokine production and breast tumor invasion. Cytoskeleton 68, 671–693 (2011).

32. Romo, M. et al. Small fragments of hyaluronan are increased in individuals with obesity and contribute to low-grade inflammation through TLR-mediated activation of innate immune cells. Int J Obes 46, 1960–1969 (2022).

33. Kim, H. S. & Chung, D. H. TLR4-mediated IL-12 production enhances IFN-γ and IL-1β production, which inhibits TGF-β production and promotes antibody-induced joint inflammation. Arthritis Res Ther 14, R210 (2012).

34. Park, S. H., Choi, H.-J., Lee, S. Y. & Han, J.-S. TLR4-mediated IRAK1 activation induces TNF-α expression via JNK-dependent NF-κB activation in human bronchial epithelial cells. Eur J Inflamm 13, 183–195 (2015).

35. Isnard, N., Legeais, J.-M., Renard, G. & Robert, L. EFFECT OF HYALURONAN ON MMP EXPRESSION AND ACTIVATION. Cell Biol Int 25, 735–739 (2001).

36. Shirvaikar, N., Montano, J., Turner, A. R., Ratajczak, M. Z. & Janowska-Wieczorek, A. Upregulation of MT1-MMP Expression by Hyaluronic Acid Enhances Homing-Related Responses of Hematopoietic CD34+ Cells to an SDF-1 Gradient. Blood 104, 2889 (2004).

37. Guidance for Industry Pyrogen and Endotoxins Testing: Questions and Answers . Food and Drug Administration 1–13 Preprint at https://www.fda.gov/regulatory-information/search-fda-guidance-documents/guidance-industry-pyrogen-and-endotoxins-testing-questions-and-answers (2012).

38. Gorbet, M. B. & Sefton, M. V. Endotoxin: The uninvited guest. Biomaterials 26, 6811–6817 (2005).

39. Sato, M. et al. Direct Binding of Toll-Like Receptor 2 to Zymosan, and Zymosan-Induced NF-κB Activation and TNF-α Secretion Are Down-Regulated by Lung Collectin Surfactant Protein A1. The Journal of Immunology 171, 417–425 (2003).

40. Ma, P., Wang, Z., Pflugfelder, S. C. & Li, D.-Q. Toll-like receptors mediate induction of peptidoglycan recognition proteins in human corneal epithelial cells. Exp Eye Res 90, 130–136 (2010).

41. Amemiya, K. et al. Activation of Toll-Like Receptors by Live Gram-Negative Bacterial Pathogens Reveals Mitigation of TLR4 Responses and Activation of TLR5 by Flagella. Front Cell Infect Microbiol 11, (2021).

42. Najibi, A. J., Shih, T.-Y. & Mooney, D. J. Cryogel vaccines effectively induce immune responses independent of proximity to the draining lymph nodes. Biomaterials 281, 121329 (2022).

43. Kwon, J. Y., Daoud, N. D., Hashash, J. G., Picco, M. F. & Farraye, F. A. Efficacy of Hepatitis B Vaccination with a Novel Immunostimulatory Sequence Adjuvant (Heplisav-B) in Patients With Inflammatory Bowel Disease. Inflamm Bowel Dis 29, 254–259 (2023).

44. Scheiermann, J. & Klinman, D. M. Clinical evaluation of CpG oligonucleotides as adjuvants for vaccines targeting infectious diseases and cancer. Vaccine 32, 6377–6389 (2014).

45. Advani, R. et al. Granulocyte-Macrophage Colony-Stimulating Factor (GM-CSF) as an Adjunct to Autologous Hemopoietic Stem Cell Transplantation for Lymphoma. Ann Intern Med 116, 183–189 (1992).

46. Arsenault, R. J., Kogut, M. H. & He, H. Combined CpG and poly I:C stimulation of monocytes results in unique signaling activation not observed with the individual ligands. Cell Signal 25, 2246–2254 (2013).

47. Liu, C. et al. Synergy effects of Polyinosinic-polycytidylic acid, CpG oligodeoxynucleotide, and cationic peptides to adjuvant HPV E7 epitope vaccine through preventive and therapeutic immunization in a TC-1 grafted mouse model. Hum Vaccin Immunother 14, 931–940 (2018).

48. Vogel, A. B. et al. BNT162b vaccines protect rhesus macaques from SARS-CoV-2. Nature 592, 283–289 (2021).

49. Levi, R. et al. One dose of SARS-CoV-2 vaccine exponentially increases antibodies in individuals who have recovered from symptomatic COVID-19. J Clin Invest 131, (2021).

50. Rhodes, S. J., Knight, G. M., Kirschner, D. E., White, R. G. & Evans, T. G. Dose finding for new vaccines: The role for immunostimulation/immunodynamic modelling. J Theor Biol 465, 51–55 (2019).

51. Wang, Y., Zhang, L., Xu, Z., Miao, L. & Huang, L. mRNA Vaccine with Antigen-Specific Checkpoint Blockade Induces an Enhanced Immune Response against Established Melanoma. Molecular Therapy 26, 420–434 (2018).

52. Kerr, M. D., McBride, D. A., Chumber, A. K. & Shah, N. J. Combining therapeutic vaccines with chemo- and immunotherapies in the treatment of cancer. Expert Opin Drug Discov 16, (2021).

53. Nishiguchi, A. & Taguchi, T. Sustained-immunostimulatory nanocellulose scaffold to enhance vaccine efficacy. J Biomed Mater Res A 108, 1159–1170 (2020).

54. Han, H.-S. et al. Development of a Bioorthogonal and Highly Efficient Conjugation Method for Quantum Dots Using Tetrazine−Norbornene Cycloaddition. J Am Chem Soc 132, 7838–7839 (2010).

55. Truong, V. X., Tsang, K. M., Ercole, F. & Forsythe, J. S. Red Light Activation of Tetrazine–Norbornene Conjugation for Bioorthogonal Polymer Cross-Linking across Tissue. Chemistry of Materials 29, 3678–3685 (2017).

56. Bencherif, S. A. et al. Injectable cryogel-based whole-cell cancer vaccines. Nat Commun 6, 7556 (2015).

57. Liu, J. et al. Cancer vaccines as promising immuno-therapeutics: platforms and current progress. J Hematol Oncol 15, 28 (2022).

58. Bakker, A. B. et al. Melanocyte lineage-specific antigen gp100 is recognized by melanoma-derived tumor-infiltrating lymphocytes. Journal of Experimental Medicine 179, 1005–1009 (1994).

59. Vasievich, E. A., Ramishetti, S., Zhang, Y. & Huang, L. Trp2 Peptide Vaccine Adjuvanted with (R)-DOTAP Inhibits Tumor Growth in an Advanced Melanoma Model. Mol Pharm 9, 261–268 (2012).

60. Duraiswamy, J., Kaluza, K. M., Freeman, G. J. & Coukos, G. Dual Blockade of PD-1 and CTLA-4 Combined with Tumor Vaccine Effectively Restores T-Cell Rejection Function in Tumors. Cancer Res 73, 3591–3603 (2013).

61. Moynihan, K. D. et al. Eradication of large established tumors in mice by combination immunotherapy that engages innate and adaptive immune responses. Nat Med 22, 1402–1410 (2016).

62. Schindelin, J. et al. Fiji: an open-source platform for biological-image analysis. Nat Methods 9, 676–682 (2012).

63. Klein, S. L., Marriott, I. & Fish, E. N. Sex-based differences in immune function and responses to vaccination. Trans R Soc Trop Med Hyg 109, 9–15 (2015).

64. Dakup, P. P., Porter, K. I., Little, A. A., Zhang, H. & Gaddameedhi, S. Sex differences in the association between tumor growth and T cell response in a melanoma mouse model. Cancer Immunology, Immunotherapy 69, 2157–2162 (2020).

65. Pollock, J. D. et al. Mouse model of X–linked chronic granulomatous disease, an inherited defect in phagocyte superoxide production. Nat Genet 9, 202–209 (1995).

66. Banerjee, E. R. & Henderson, W. R. Role of T cells in a gp91phox knockout murine model of acute allergic asthma. Allergy, Asthma & Clinical Immunology 9, 6 (2013).

CHAPTER 5

CONCLUSIONS AND FUTURE DIRECTIONS

5.1 Overview

This chapter is organized into two major parts. First, a summary of research and major conclusions is overviewed. Second, future research directions stemming from the conclusions of this work are discussed.

5.2 Summary

The thesis focused on the development of biodegradable hyaluronic acid scaffolds for the sustained release of immunomodulators to enhance immunity. In Chapter 2, click-crosslinked HA cryogels are introduced and their utility as a drug delivery platform is established. From studies comparing HA cryogel degradation kinetics in immune competent and immune deficient mouse models, particularly NSG and gp91^{-phox}, we determined that degradation of the HA cryogels was primarily driven by oxidative burst of neutrophils. In post-HSCT mice, HA cryogel degradation was delayed for 3-weeks and coincided with peripheral blood neutrophil reconstitution and HA cryogel infiltration. This data supported the finding that neutrophils are primarily responsible for HA cryogel degradation. Leveraging these findings, G-CSF was encapsulated within the HA cryogel and the delayed degradation in HSCT settings sustained the release of G-CSF from HA cryogels and accelerated neutrophil reconstitution.

In Chapter 3, cancer vaccine strategies involving both allogenic and autologous engineered whole cell-based vaccines were discussed. Peptide-based and DNA-based tumor antigen targeted subunit vaccines are reviewed. Clinical results for cancer vaccines

and newer strategies combining cancer vaccines with chemotherapy or immune checkpoint blockade are emphasized.

Chapter 4 combined the system developed in Chapter 2 with the concept of cancer vaccines reviewed in Chapter 3. HA sourced from different suppliers and formulated into cryogels termed HAC1 and HAC2. OVA was encapsulated in the cryogels and differences in degradation kinetics, innate immune response to the cryogels, and anti-OVA IgG1 titers were assessed. From these studies, we chose to proceed with HAC2 and incorporated additional adjuvants CpG and/or GM-CSF into OVA-HAC2. Both GM-CSF and CpG enhanced adaptive immune response to vaccination comparably. Inclusion of GM-CSF increased inflammation at the injection site. In contrast, CpG enhanced adaptive immune response while foreign body response at the biomaterial site was unaffected. As a result, CpG-OVA-HAC2 formulation was further assessed in both prophylactic and therapeutic studies using a melanoma model. CpG-OVA-HAC2 conferred protection in these models supporting its potential as an immunotherapeutic agent in cancer.

5.3 Future Directions

This work has established the HA cryogel platform as a biodegradable drug delivery device. There is potential to further expand the use cases and address limitations of this platform in vaccination settings. Several proposed follow-up studies are overviewed in the following sub-sections.

5.3.1 Subunit Vaccination Against Melanoma Antigens

The HA cryogel vaccine formulation, OVA-CpG-HAC2, induces an adaptive immune response against a model antigen OVA. A potential direction is to induce an adaptive immune response to melanoma specific antigens such as glycoprotein 100

(gp100)[9] or tyrosinase-related protein 2 (trp2)[10]. Adjuvant dose, antigen dose, and combination of melanoma antigens are all parameters which can be modified to maximize the adaptive immune response. This approach could potentially be combined with immune checkpoint blockade or chemotherapy to better mimic clinical strategies for deploying therapeutic cancer vaccines.

5.3.2 Subunit Vaccination Against Infectious Diseases

Vaccination with the HA cryogel platform can be expanded beyond cancer to prevent viral infections such as influenza or SARS-CoV-2. As compared to bolus vaccination, the HA cryogel system sustains the release of antigen and adjuvant over a prolonged period which enhances the adaptive immune response and may preclude necessity of booster vaccinations. Antigen and adjuvant identity and dosing may need to be modified to ensure robust adaptive immune response following long-term room temperature lyophilization and storage.

5.4 Concluding Remarks

The work presented in this thesis has resulted in the development of HA cryogels as a biodegradable drug delivery platform. The neutrophil responsive degradation of HA cryogels represents a new mechanism of drug release which can be leveraged to improve delivery. HA cryogels are amenable to the encapsulation of a range of immunomodulatory agents which could be explored in further research. The flexibility could also be leveraged for developing personalized immunotherapies.

5.5 References

1. McBride, D. A. et al. Immunomodulatory Microparticles Epigenetically Modulate T Cells and Systemically Ameliorate Autoimmune Arthritis. Advanced Science 10, 2202720 (2023).

2. Sun, C.-M. et al. Small intestine lamina propria dendritic cells promote de novo generation of Foxp3 T reg cells via retinoic acid. Journal of Experimental Medicine 204, 1775–1785 (2007).

3. Kang, S. G., Lim, H. W., Andrisani, O. M., Broxmeyer, H. E. & Kim, C. H. Vitamin A Metabolites Induce Gut-Homing FoxP3+ Regulatory T Cells1. The Journal of Immunology 179, 3724–3733 (2007).

4. Carlson, M. J. et al. In vitro–differentiated TH17 cells mediate lethal acute graft-versus-host disease with severe cutaneous and pulmonary pathologic manifestations. Blood 113, 1365–1374 (2009).

5. Li, W. et al. Proteomics analysis reveals a Th17-prone cell population in presymptomatic graft-versus-host disease. JCI Insight 1, (2016).

6. Malard, F., Gaugler, B., Lamarthee, B. & Mohty, M. Translational opportunities for targeting the Th17 axis in acute graft-vs.-host disease. Mucosal Immunol 9, 299–308 (2016).

7. Amsden, B. G. Hydrogel Mesh Size and Its Impact on Predictions of Mathematical Models of the Solute Diffusion Coefficient. Macromolecules 55, 8399–8408 (2022).

8. Moncure, P. J., Simon, Z. C., Millstone, J. E. & Laaser, J. E. Relationship between Gel Mesh and Particle Size in Determining Nanoparticle Diffusion in Hydrogel Nanocomposites. J Phys Chem B 126, 4132–4142 (2022).

9. Bakker, A. B. et al. Melanocyte lineage-specific antigen gp100 is recognized by melanoma-derived tumor-infiltrating lymphocytes. Journal of Experimental Medicine 179, 1005–1009 (1994).

10. Vasievich, E. A., Ramishetti, S., Zhang, Y. & Huang, L. Trp2 Peptide Vaccine Adjuvanted with (R)-DOTAP Inhibits Tumor Growth in an Advanced Melanoma Model. Mol Pharm 9, 261–268 (2012).